A Letter of Intent to
The J-PARC 50 GeV Proton Synchrotron Experiments

A Study of a Neutrino Factory in Japan (Nufact-J)

Nufact-J Working Group

January 1, 2003

The Nufact-J Working Group Members

The full member list will be added later. The contact persons are Yoshiharu Mori (KEK) and Yoshitaka Kuno (Osaka).

Abstract

We, the Nufact-J working group, would like to present our preliminary study on a neutrino factory in Japan, at the location of J-PARC. The Japanese scheme of a neutrino factory is based on a novel method of muon acceleration by fixed field alternating gradient synchrotrons (FFAG). We show the physics cases of a neutrino factory, a preliminary design of the acceleration complex, a possible layout, and our staging scenario.

Contents

Chapter 1

Executive Summary

What is a Neutrino Factory ? : A neutrino factory is a high-intensity neutrino source based on muon storage ring. Accelerated muons are injected into a storage ring, where muon decays in the straight section of the storage ring would provide a high intensity beam of neutrinos. The neutrino beam energy can be from a few GeV to several 10 GeV, and have a relatively narrow energy spread. The beam intensity anticipated at a neutrino factory is about 100 times the present intensity of conventional beams based on pion decays in the same energy range.

Physics Motivation : A high-intensity accelerator-based neutrino source is definitely a next-generation facility of particle physics. It is required in order to push neutrino physics forward into an unexplored territory. One of the physics motivations at neutrino factories is to study the 3×3 neutrino mixing matrix, which is called Maki-Nakagawa-Sakata (MNS) mixing matrix [1]. This is a completely new field in the lepton sector that must be pursued from now on, after many years of studies on the Kobayashi-Maskawa mixing matrix in the quark sector. The potential topics are

1. determination of θ_{13},

2. determination of the sign of Δm^2_{32}, and

3. the discovery of CP violation in the lepton sector (δ_{CP}).

Physics Sensitivity : Just after the completion of the 50-GeV PS of about 1 mega-watt beam power, it would be natural to start an experiment with a conventional pion-based neutrino beam to Super-Kamiokande. Then, a neutrino factory with higher intensity would follow to complete the studies.

It is however necessary to identify the physics reaches with the superbeam and with a neutrino factory. In general, if one of the mixing angle, $\sin 2\theta_{13} < 0.01$, the conventional beam with a water Cerenkov detector has difficulty to discover $\nu_\mu \to \nu_e$ oscillation. It would not be improved even if the detector size becomes larger mostly because of backgrounds from π^0. Therefore, in

the case of small $\sin 2\theta_{13}$, a neutrino factory is the only possibility to explore the physics potentials [4]. The sensitivity to $\sin^2 \theta_{13}$ is shown in Fig.1.1.
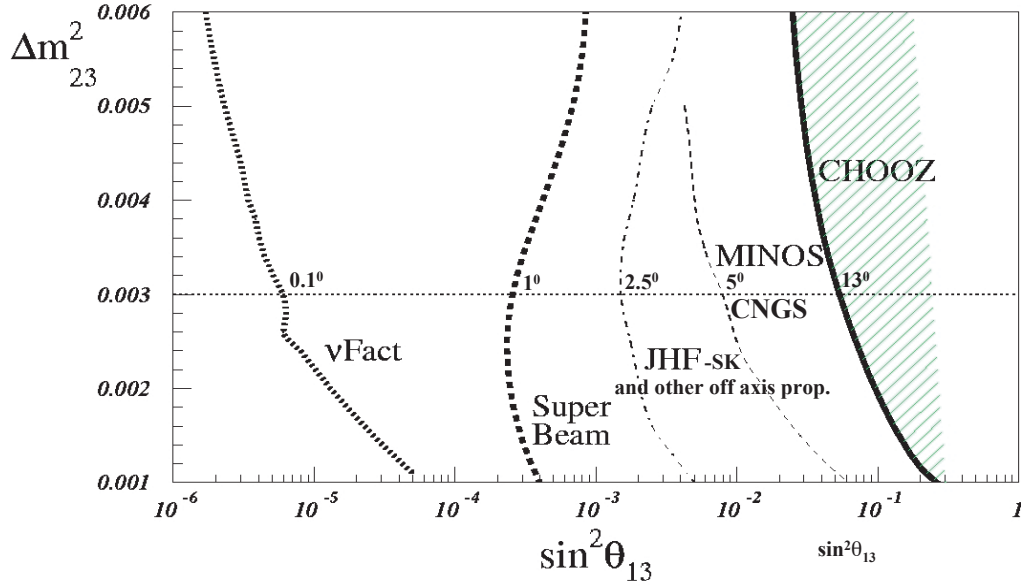
Figure 1.1: Sensitivity to $\sin^2 \theta_{13}$ with a neutrino factory (νFact) and conventional pion-based superbeams.

The physics goals of both (1) determination of θ_{13} and (2) determination of the sign of the Δm_{32}^2 need an energetic neutrino beam ($\sim$ a few 10 GeV) with a long oscillation distance ($\sim$ a few 1000 km). However, (3) search for CP (or T) violation requires some optimization on them. The CP asymmetry A_{CP} is known to scale with (L/E), where L and E are the baseline length and the energy of a neutrino beam, suggesting that having a long baseline length and a low energy is better. However, a figure of merit of the sensitivity is given by $A_{CP} \times \sqrt{N_{osc}}$ where N_{osc} is a number of the oscillating events and it is proportional to the energy of neutrino. It becomes clear that the search for CP violation at very low energy become difficult because statistics is simply not enough. At a long distance, the matter effect dominates over the intrinsic CP violation, and therefore it has to be discriminated. The other issues in the search for CP violation is whether we like to see the CP asymmetry or we just determine the imaginary phase in the MNS matrix. This two different approaches give two different optimization. For the latter, 50 GeV and 3000 km gives the best solution, and the former gives lower energy and shorter distance. For further studies, more inputs on the MNS mixing matrix elements are needed. Also the possibility of search for T-violation must be pursued.

Finally it should be stressed that neutrino physics is not just only oscillation physics. There could appear unexpected important physics topics. Therefore, the most important thing is to construct as a high intensity neu-
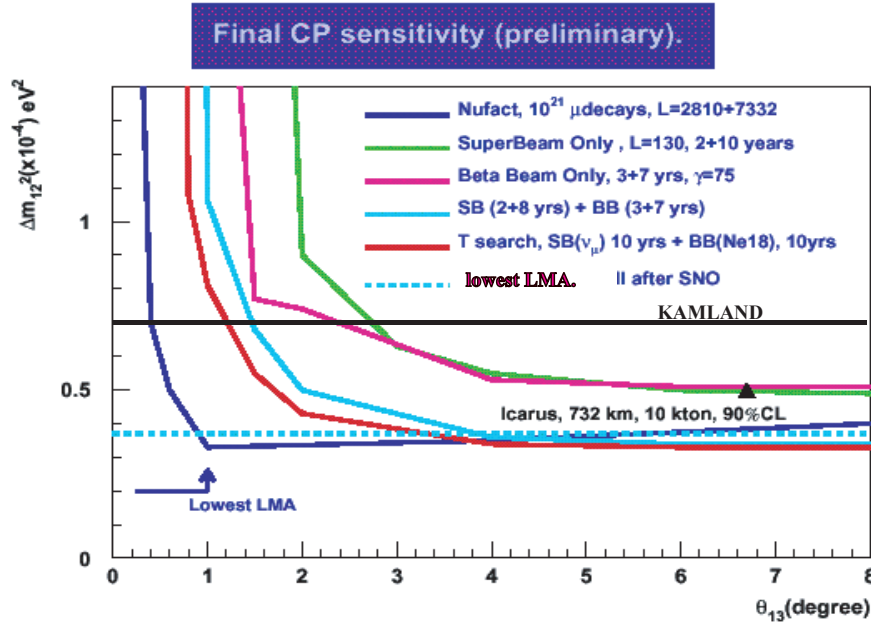
Figure 1.2: Sensitivity to CP violation with a neutrino factory and conventional pion-based superbeams as a function of Δm_{12}^2 and θ_{13}.

trino source as possible.

The Japanese Acceleration Scheme : The accelerator complex of the neutrino factory considered in Japan has significantly different aspect from the others in U.S. [2] and in Europe [3]. One of the major differences that should be stressed is to adopt a series of fix field alternating gradient synchrotrons (FFAG) for muon acceleration. FFAG is known to have wide longitudinal (momentum) acceptance, and wide transverce (geometrical) acceptance, compared with ordinary synchrotrons. It allows us to accelerate directly a muon beam of broad emittance, without involving any phase rotation and muon ionization cooling. Some of the advantages given by FFAG acceleration are listed as follows;

- simplicity of the accelerator complex,

- potential cost saving (because of adoption of circular rings instead of linear accelerators),

- earlier readiness of technology necessary (because of less R&D items, in particular the muon cooling is not involved),

The Japanese scheme for 20 GeV muon acceleration consists of four FFAG rings. The first ring accelerates the muons from 0.3 GeV/c to 1 GeV/c, the second ring does from 1 GeV/c to 3 GeV/c, the third ring does from 3 GeV/c

5

to 10 GeV/c, and the last ring does from 10 GeV/c to 20 GeV/c. Then, the accelerated muons are injected into a muon storage ring with a racetrack shape.
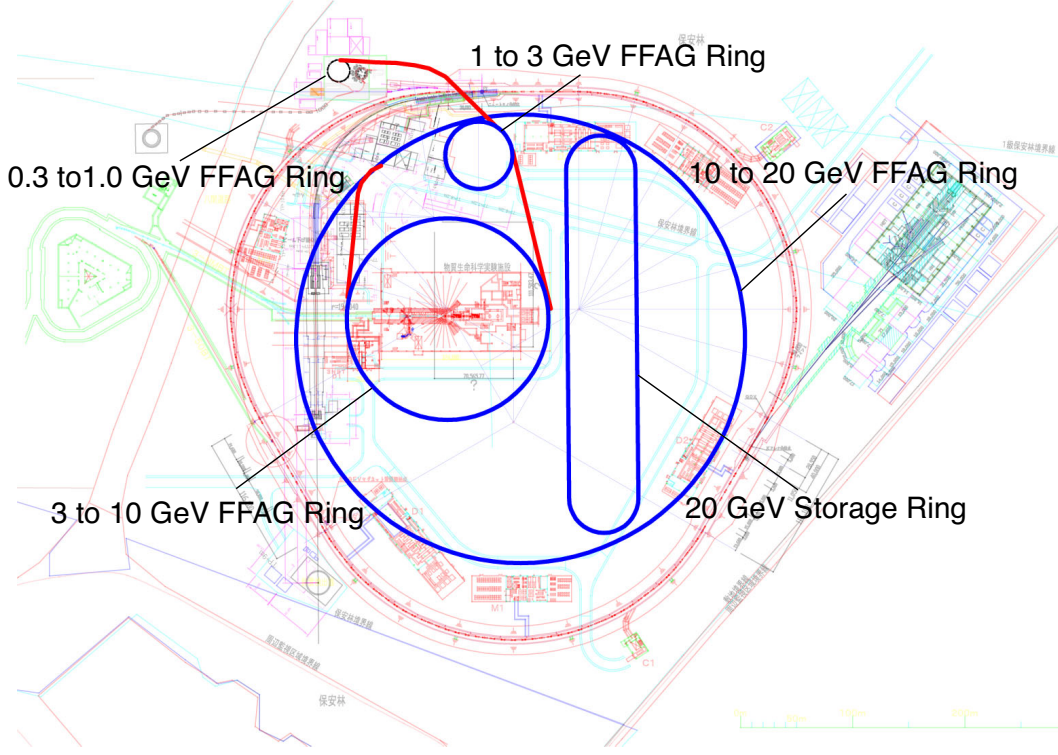
Figure 1.3: Schematic layout of a neutrino factory at J-PARC. The muon acceleration from low energy to 20 GeV/c is based on a series of four FFAG rings.

The Neutrino Factory at J-PARC : J-PARC is a natural place to construct a neutrino factory in Japan, since a high intensity proton accelerators, such as the J-PARC 50 GeV proton synchrotron, is planned to be built. The high beam power of about 1 MW, and its upgrade of 4.4 MW, would provide the best opportunity for the realization of a neutrino factory in the world. One of the drawbacks considered for the case at J-PARC is that the Tokai campus is not sufficiently large. Therefore, the construction of an underground facility must be considered. It is also the case once one tries to avoid neutrino hazard. A possible layout of the neutrino factory at J-PARC is shown in Fig.1.3.

The number of muon decays in the muon storage ring is aimed to be about 1×10^{20} muon decay/one straight section/year. The energy of muons is at most $10 - 20$ GeV in the first phase (J-PARC Phase-I), and will be

Table 1.1: Parameters of Neutrino Factory Scenario

	A Number of Muon Decays (/straight section/year)	Maximum Muon Energy	Proton Beam Power
Phase-I	1×10^{20}	$10 - 20$ GeV	1 MW
Phase-II	4.4×10^{20}	$20 - 50$ GeV	4.4 MW

improved to be 4.4×10^{20} muon decay/one straight section/year by increasing the primary proton beam intensity in the next phase (J-PARC Phase II). The muon energy could be increased to $20 - 50$ GeV if necessary. The determination of muon energy and intensity in the muon storage ring will be subject to physics demands and cost optimization. They are listed in Table 1.1.

Staging Approach : A staging approach should be seriously considered to construct a large scaled project like a neutrino factory. This staging approach is demanded in two folds. One is to maintain a total budget profile to be a reasonable size at different stages to get the funding easier. The second is that it will require a long term to establishing required technology, whereas we like to keep physics activities even in the R&D period. In our FFAG acceleration scheme, it is possible since we start with the first acceleration ring, and add downstream FFAG rings at a later time. Possible connection to physics programs is listed in Table 1.2.

Table 1.2: Possible scenario of the staging based on FFAG acceleration.

Stage	FFAG ring	Potential Physics Programs
0	Low energy (PRISM)	muon LFV
1	0.3-1 GeV/c (PRISM-II)	muon EDM and low-energy neutrino source
2	1-3 GeV/c	1 GeV neutrino source
3	3-10 GeV/c	an initial neutrino factory
4	10-20 GeV/c	a full size neutrino factory

Chapter 2

Overview

Japan has been taking a major leading role in neutrino physics at present. To keep this high level of physics contributions from Japan and go steps further, it is definitely required to have neutrino sources with higher intensity. To achieve this, a neutrino beam based on a muon storage ring has been considered extensively [2, 3].

2.1 What is a Neutrino Factory ?

A neutrino factory is a high-intensity neutrino source based on muon storage ring. The neutrino beam energy ranges from a few GeV to several 10 GeV. The beam intensity anticipated at a neutrino factory is about 100 times the present intensity of conventional beams based on pion decays in the corresponding energy region. It is firmly believed that a neutrino factory would open great opportunities for significant progress in neutrino physics. Historically, it was considered based on the R&D works of a $\mu^+\mu^-$ collider. Therefore, all the efforts towards a neutrino factory could have potentials leading the realization of future energy-frontier $\mu^+\mu^-$ colliders at TeV energy range.

In the design of a neutrino factory, muons of 20-50 GeV are injected into a storage ring. Muon decays in the long straight section of the muon storage ring would provide a high intensity beam of neutrinos. A number of neutrinos of about $10^{20} - 10^{21}$ neutrinos/year/straight section is aimed. Both μ^+s and μ^-s are used to produce four different flavors of neutrinos, ν_e, $\overline{\nu}_e$, ν_μ and $\overline{\nu}_\mu$ from $\mu^+ \rightarrow e^+ + \overline{\nu}_\mu + \nu_e$ and $\mu^- \rightarrow e^- + \nu_\mu + \overline{\nu}_e$ decays. To identify neutrino or anti-neutrino events at the detector, the charge discrimination is required at detection.

2.1.1 Advantages of neutrino factory

A neutrino factory is needed to make precision measurement of neutrino oscillation at a long baseline. The precision of 10^{-3} or better will be needed to determine all of the physics parameters in the lepton sector. To achieve, a

high intensity beam of neutrinos with full understanding of beam characteristic is required. To meet all the requirements, a neutrino beam from muon decays must be the best candidate in the following reasons:

1. higher neutrino-beam intensity at high energy, of $10^{20} - 10^{21}$ neutrinos/year, which is about 100 times intensity at a few 10 GeV energy range. In particular, energetic ν_e ($\bar{\nu}_e$) beams can be available at only a neutrino factory,

2. lower background of $10^{-4} - 10^{-3}$ level (which is compared with a few % level at the pion source), and

3. precise knowledge on neutrino intensity and emittance.

Thus, a neutrino factory is suitable for precision measurements.

2.1.2 Oscillation Signature

At the neutrino factory, the oscillation signature is determined by a wrong-signed lepton. For instance, when μ^-s are in the muon storage ring, they decay as $\mu^- \rightarrow e^- \nu_{mu}\, \bar{\nu}_e$. Thus, the beam contains 50 % neutrinos and 50 % anti-neutrinos. The only way to determine what the parent neutrino was is to measure the charge of the final state lepton. The oscillation of $\bar{\nu}_e \rightarrow \bar{\nu}_\mu$ would produce a wrong-sign μ^+. In practice, the discrimination of e^+ and e^- is more difficult than that of μ^+ and μ^-. And therefore, $\nu_e \rightarrow \nu_\mu$ ($\bar{\nu}_e \rightarrow \bar{\nu}_\mu$) are looked at at a neutrino factory.

2.1.3 Beam intensity and rates

The neutrino flux from a neutrino factory can be estimated [5, 7]. First of all, at the muon-rest frame, the distributions of neutrinos (anti-neutrinos) from (unpolarized) muon decays are given as follows.

$$
\begin{aligned}
\frac{d^2\sigma_{\nu_\mu,\bar{\nu}_\mu}}{dxdt} &= x^2(3 - 2x), \\
\frac{d^2\sigma_{\nu_e,\bar{\nu}_e}}{dxdt} &= 6x^2(1 - x),
\end{aligned}
\tag{2.1}
$$

where $x = 2E_\nu/m_\mu$. At the laboratory frame where muons are accelerated, the neutrino flux at a distance, L, along the forward direction of muon momentum are given by

$$
\begin{aligned}
\Phi_{\nu_\mu,\bar{\nu}_\mu} &= \gamma^2 \frac{n_\mu}{\pi L^2} \left\{ 2y^2(3 - 2y) \right\}, \\
\Phi_{\nu_e,\bar{\nu}_e} &= \gamma^2 \frac{n_\mu}{\pi L^2} \left\{ 12y^2(1 - y) \right\},
\end{aligned}
\tag{2.2}
$$

where n_μ is a number of decaying muons, $\gamma = E_\mu/m_\mu$ and $y = E_\nu/E_\mu$. It should be noted that the total neutrino flux increases with E_μ^2.

9

The charged-current rates, which arises as neutrino-nucleon scattering, can be estimated. For high-energy neutrinos ($\sim$ tens of GeV), the deep inelastic scattering ($\nu + A \rightarrow l + X$). The cross section (of deep inelastic scattering) are proportional to the neutrino energy, E_ν, and are given by

$$
\begin{aligned}
\sigma_{\nu N} &\sim 0.67 \times 10^{-38} \times E_\nu[\text{GeV}] \ (\text{cm}^2), \\
\sigma_{\bar{\nu} N} &\sim 0.34 \times 10^{-38} \times E_\nu[\text{GeV}] \ (\text{cm}^2).
\end{aligned}
\tag{2.3}
$$

From Eq.(2.2) and (2.3), the rates of charged-current events (in the case of no oscillation) can be estimated.

$$
\begin{aligned}
N_{\nu_\mu} &\sim 8 \times \frac{n_\mu[10^{21}]E_\mu^3[\text{GeV}]N_k[\text{kt}]}{L^2[1000\text{km}]}, \\
N_{\nu_e} &\sim 7 \times \frac{n_\mu[10^{21}]E_\mu^3[\text{GeV}]N_k[\text{kt}]}{L^2[1000\text{km}]}, \\
N_{\bar{\nu}_\mu} &\sim 4 \times \frac{n_\mu[10^{21}]E_\mu^3[\text{GeV}]N_k[\text{kt}]}{L^2[1000\text{km}]},
\end{aligned}
\tag{2.4}
$$

$$
N_{\bar{\nu}_e} \sim 3.5 \times \frac{n_\mu[10^{21}]E_\mu^3[\text{GeV}]N_k[\text{kt}]}{L^2[1000\text{km}]}.
\tag{2.5}
$$

2.2 Oscillation Physics at Neutrino Factory

One of the major physics topics at the neutrino factory is to measure and determine the neutrino mixing matrix, which is now called the Maki-Nakagawa-Sakata (MNS) matrix [1]. It is given by

$$
\begin{pmatrix} \nu_e \\ \nu_\mu \\ \nu_\tau \end{pmatrix} = U_{MNS} \cdot \begin{pmatrix} \nu_1 \\ \nu_2 \\ \nu_3 \end{pmatrix},
\tag{2.6}
$$

where the MNS matrix is

$$
U_{MNS} = \begin{pmatrix} c_{12}c_{13} & s_{12}c_{13} & s_{13}e^{-i\delta} \\ -s_{12}c_{23}-c_{12}s_{13}s_{23}e^{-i\delta} & c_{12}c_{23}-s_{12}s_{13}s_{23}e^{i\delta} & c_{13}s_{23} \\ s_{12}c_{23}-c_{12}s_{13}c_{23}e^{i\delta} & -c_{12}s_{23}-s_{12}s_{13}c_{23}e^{i\delta} & c_{13}c_{23} \end{pmatrix}
\tag{2.7}
$$

where $c_{ij} = \cos\theta_{ij}$ and $s_{ij} = \sin\theta_{ij}$. θ_{12}, θ_{13}, and θ_{23} are three mixing angles, and δ is a CP-violating phase. Other parameters are the mass squared difference, Δm_{21}^2 and Δm_{32}^2. The current knowledge on these parameters are obtained in Table 2.1. These parameters will be determined more precisely in the measurements of long-baseline neutrino oscillations at a neutrino factory.

Major goals of the oscillation physics program are such as

- determination of θ_{13},

Table 2.1: Current knowledge on the MNS mixing parameters

Parameters	Comments
$\Delta m_{32}^2 \sim 3 \times 10^{-3}$ eV^2 $\sin^2 \theta_{23} \sim (0.9 - 1.0)$	from atmospheric neutrinos
$\Delta m_{13}^2 < 0.1$	from CHOOZ
$\Delta m_{21}^2 \sim 7 \times 10^{-5}$ $\sin^2 2\theta_{12} \sim (0.5 - 0.8)$	from solar neutrinos (large angle MSW solution)
δ	unknown

- determination of the sign of Δm_{32}^2, and

- search for CP violation in the neutrino sector.

2.2.1 Oscillation event rates

In the three-generation neutrino mixing, when $|\Delta m_{21}^2| << |\Delta m_{32}^2|$, the oscillation probabilities in vacuum are given by

$$
\begin{aligned}
P(\nu_e \to \nu_\mu) &\approx \sin^2(2\theta_{13}) \sin^2(\theta_{23}) \sin^2\Big(\frac{1.27\Delta m_{32}^2 L}{E_\nu}\Big), \\
P(\nu_e \to \nu_\tau) &\approx \sin^2(2\theta_{13}) \cos^2(\theta_{23}) \sin^2\Big(\frac{1.27\Delta m_{32}^2 L}{E_\nu}\Big), \\
P(\nu_\mu \to \nu_\tau) &\approx \cos^4(\theta_{13}) \sin^2(2\theta_{23}) \sin^2\Big(\frac{1.27\Delta m_{32}^2 L}{E_\nu}\Big).
\end{aligned}
\tag{2.8}
$$

From Eq.(2.8), it is seen that the measurement of $P(\nu_e \to \nu_\mu)$ will determine for instance θ_{13}. In the currently-proposed scheme of a neutrino factory, E_ν is relatively high (of $20 - 50$ GeV), yielding $(\Delta m_{32}^2 \cdot L/E_\nu)$ is small. And thereby the oscillation probability is not terribly large but high statistics would give a good figure of merit in observing the oscillation phenomena. It will be shown below.

The charged neutrino current rate is given by

$$
N_{cc}(\nu_e \to e^-) \propto \theta_\nu^2 \cdot \sigma_{inela}(E_\mu) \propto \frac{E_\mu^2}{L^2} \cdot E_\mu = \frac{E_\mu^3}{L^2},
\tag{2.9}
$$

where θ_ν is an opening angle of the neutrino beam, and the fact that the neutrino inelastic interaction (σ_{inela}) is proportional to a neutrino energy (E_μ) is used. Typically, at 1500 km with the muon energy of 30 GeV, 0.5 M events can be expected for a 10 kton detector.

The oscillation event rate is then given by

$$
N_{osc}(\nu_e \to \mu^-) \propto \theta_\nu^2 \cdot \sigma_{inela}(E_\mu) \cdot P(\nu_e \to \nu_\mu) \propto \frac{E_\mu^3}{L^2} \cdot \frac{L^2}{E_\mu^2} = E_\mu
\tag{2.10}
$$

11

where the oscillation probability is assumed to be proportional to $P(\nu_e \rightarrow \nu_\mu) \propto L^2/E_\mu^2$ since $\Delta m^2 \cdot L^2/E_\mu^2$ is sufficiently small. Therefore, to observe more neutrino-oscillation events, a higher energy is better.

2.2.2   CP violation

The CP-odd oscillation probability is given by

$$P_{CPodd}(\nu_e \rightarrow \nu_\mu) \sim -4J \frac{\delta m_{21}^2 L}{2E_\nu} \sin^2 \Big(\frac{\delta m_{31}^2 L}{4E_\nu} \Big) \propto \Big(\frac{L^3}{E_\nu^3} \Big), \qquad (2.11)$$

where J is the Jarlskog parameter given by

$$J = c_{12} c_{13}^2 c_{23} s_{12} s_{13} s_{23} \sin(\delta). \qquad (2.12)$$

The observable of the CP-odd asymmetry is defined by

$$A_{CP-odd} \equiv \frac{P(\nu_e \rightarrow \nu_\mu) - P(\overline{\nu}_e \rightarrow \overline{\nu}_\mu)}{P(\nu_e \rightarrow \nu_\mu) + P(\overline{\nu}_e \rightarrow \overline{\nu}_\mu)} \propto \frac{L}{E_\nu} \qquad (2.13)$$

The CP-odd asymmetry is proportional to L/E_ν. Since the number of the oscillation events is given by Eq.(2.10). The figure of merit is given by

$$A_{CP-odd}^2 \cdot N_{osc} \propto \frac{L^2}{E_\nu}. \qquad (2.14)$$

To search for CP violation in neutrino sector, it cannot be simply concluded that a higher energy is better, rather a lower energy might be more preferable. But, if the neutrino energy is too low, the neutrino intensity is definitely not sufficient. To reduce the matter effect, it is also desirable to have a shorter distance. A study of all the optimization is underway.

2.2.3   T violation

The comparison of the time-reversed oscillation processes would give a good test of T-violation as follows,

$$A_T = \frac{P(\nu_\alpha \rightarrow \nu_\beta) - P(\nu_\beta \rightarrow \nu_\alpha)}{P(\nu_\alpha \rightarrow \nu_\beta) + P(\nu_\beta \rightarrow \nu_\alpha)} \qquad (2.15)$$

The T-violating asymmetry defined the above is known to have smaller contribution from the matter effect. It is also discussed that the intrinsic T-violating asymmetry can be modified slightly by the matter effects[6]. To observe T-violation, the detection of $\nu_\mu \rightarrow \nu_e$ oscillation is needed, where the naive charge identification of $e^\pm$ is believed to be difficult. Some consideration is underway to overcome this difficulty. But, if it become doable, the search for T-violation would give the best sensitivity to measure the CP-violating imaginary phase in the MNS matrix.

2.3 The Japanese Scheme of A Neutrino Factory

The Japanese scenario of a neutrino factory based on on the scheme of FFAG (Fixed-Field Alternating Synchrotron) acceleration.[1] In this scheme, after the muon capture, a series of FFAG rings are used to accelerate muons of large emittance. It could be possible since FFAG is the machine which has a large transverse and longitudinal acceptance. A possible layout is shown in Fig.2.1. In the layout, there are four rings, where the first ring is acceleration from 0.3 GeV/c to 1 GeV/c, the second is from 1 to 3 GeV/c, the third is for from 3 to 10 GeV/c, and the forth is from 10 to 20 GeV/c.

FFAG based neutrino factory

FFAG-2
1-3GeV/c

FFAG-I
0.3-1GeV/c

MSR
20GeV/c

FFAG-3
3-10GeV/c

100m

FFAG-4
10-20GeV/c
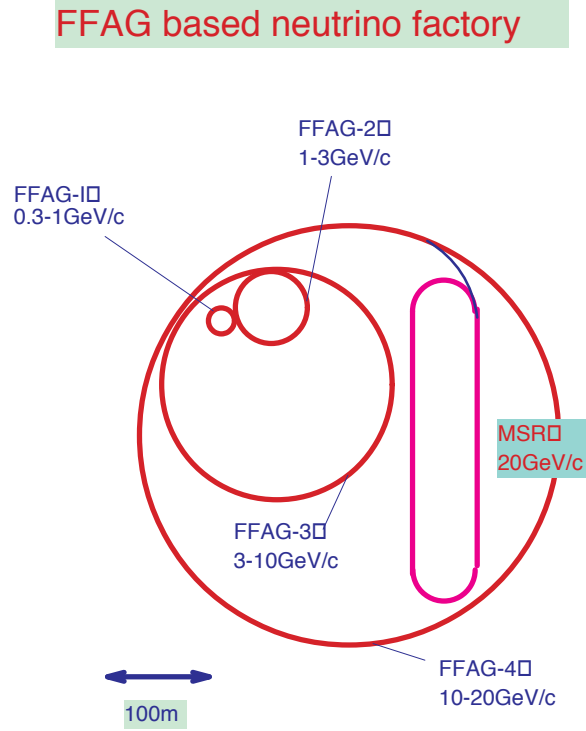
Figure 2.1: A neutrino factory based on FFAG acceleration.

The specifications of the Japanese neutrino factory at the two different stages are shown as follows:

- **Phase I**: 1.0×10^{20} muon decays/year at the one straight section. The initial beam power of the 50-GeV PS is 1 MW. The muon energy in the muon storage ring is 20 MeV.

- **Phase II**: 4.4×10^{20} muon decays/year at the one straight section. The beam power of the 50-GeV PS is upgraded to 4.4 MW by installing

---

[1]The details of the accelerators are shown in Chapter 3.

more rf cavities in the 50-GeV PS ring. The muon energy in the muon storage ring is from 20-50 GeV.

Chapter 3

Accelerators

The Japanese scenario of a neutrino factory is based on muon acceleration by fixed field alternating gradient synchrotrons (FFAG). In this chapter, a preliminary study of the accelerators is shown.

3.1 Overview

3.1.1 A neutrino factory in the linear system

The goal of a total number of muon decays in one straight section of the muon storage ring at the first stage of the neutrino factory is more than 1×10^{20} muon decays per year, and that at the second stage is about 5×10^{20} muon decays per year. A high accelerating gradient and a small total length of the accelerators should be needed to minimize beam loss caused by muon decay. But, it requires that the rf frequency used in the linear accelerator system should be relatively high. The typical rf frequency range utilized in this scheme is several 100 MHz. Moreover, a small total length of the linear accelerator system also helps to reduce the cost of the accelerator. The muon survival for various accelerating field gradients when the muons are accelerated from 300 MeV/c to 20 GeV/c is shown in Fig.3.1.

The conventional neutrino factory scheme, so called "PJK" scenario, which is based on the linear accelerators and muon storage ring, has been proposed [10]. In the linear accelerator based neutrino factory scenario, the accelerating field gradient should be more than 5 MV/m. This is not only to increase muon survival rates, but also because the total distance during the acceleration becomes tremendously large in the linear accelerator system if the accelerating field gradient is less than 5 MV/m.

In order to achieve such a high accelerating field gradient in an rf system, it is inevitable to adopt an rf system using relatively high frequency rf cavities where the frequency range is several 100 MHz. For such a high frequency rf accelerating system, the beam aperture size is limited to keep the shunt impedance of the rf cavity large enough. This limits the transverse acceptance of the system. Thus, transverse muon beam cooling before
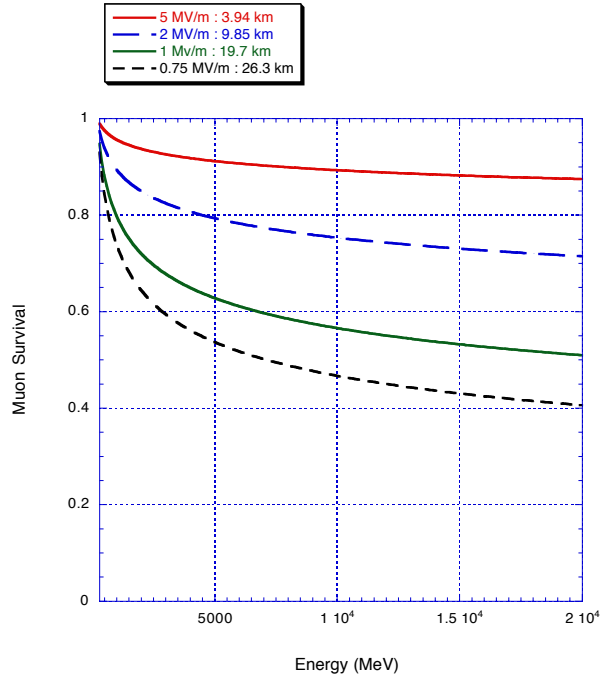
Figure 3.1: Muon survival during acceleration from 300 MeV/c to 20 GeV/c for various accelerating gradients and fractional distances along the machine

acceleration becomes essential in the high frequency rf accelerating system.

Any ordinary beam cooling such as stochastic cooling can obviously be useless since the cooling time is much longer than the muon lifetime. Ionization cooling consists of a number of energy degrading media between the rf accelerating cavities, and seems to be a possible solution. To make cooling efficient, the accelerating field gradient of the rf cavity has to be large and also a high frequency rf system whose frequency range is more than 100 MHz is unavoidable.

The initial pions and the product muons, however, have a large energy spread, which is much larger than the acceptance of the ionization cooling system. Phase rotation before cooling is also required to decrease the energy spread. Total beam loss in the cooling channel seems to be very large. According to detailed work done by the FNAL group, the muon beam intensity after cooling could drop substantially.

3.1.2 Why is the circular system ?

If a ring accelerator can be adopted to muon acceleration, this limitation becomes modest. Many turns for acceleration in the same ring using the same accelerating system help to reduce the total size of the accelerator and the total construction cost. As can be seen in Fig.3.1, even when the accelerating gradient is only 1 MV/m, the muon survival during acceleration up to 20 GeV/c is still more than 50 %, which should not be so painful.

16

Such a low accelerating field gradient can be realized with a rather low frequency rf accelerating system. For example, in the anti-proton decelerator (AD) at CERN, the 9.5 MHz rf cavity has achieved a field gradient of about 0.35 MV/m with a modest rf peak power of 0.19MW in burst mode operation[18]. If the rf power increases, the field gradient could reach 1 MV/m. One of the advantages in using a low frequency rf system is its large longitudinal acceptance. The typical longitudinal acceptance with such a low frequency rf system would be several eV·s or more. The particle distribution of the initial pions and the product muons in the longitudinal phase space after the captured solenoid when the 50 GeV proton driver described above is used are shown in Fig.3.2. In this case, the bunch length of the primary proton beam from the 50 GeV proton driver is assumed to be 6 nsec in rms value.
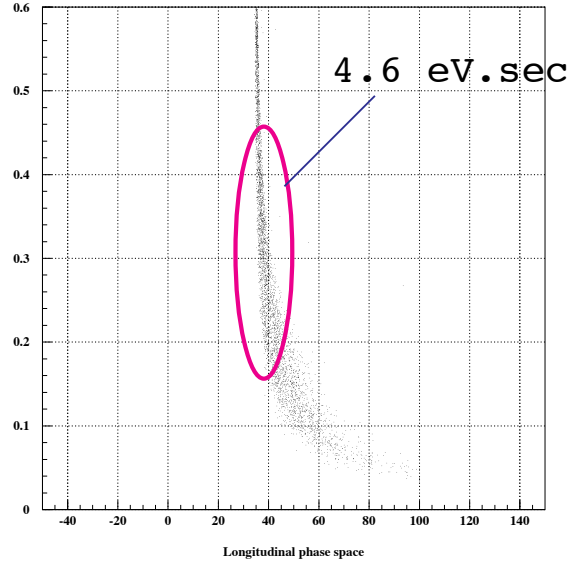

Figure 3.2: The particle distribution of the initial pions, and the product muons generated by a short bunched 50 GeV proton beam in the longitudinal phase space. (Horizontal axis: time of flight(ns) Vertical axis:total momentum(GeV/c))

As can be seen in the figure, the particles having central momentum and momentum spread of 300 MeV/c and $\pm50\%$, respectively, are well within the area of 4.6 eV.s.

This size of longitudinal acceptance can be realized by a low frequency rf accelerating system having an accelerating field gradient of 1 MV/m. Obviously, a linear accelerator with such a low frequency rf system is not suitable for accelerating muons to high energy because the total distance becomes too long. Thus, a ring accelerator is practically the only scheme possible for muon acceleration with a low frequency rf system.

17

3.1.3 Why is the FFAG ?

The ordinary synchrotron is obviously inadequate for accelerating muons. The magnetic field in an ordinary synchrotron must increase during acceleration and the ramping rate cannot be fast enough to compete with the muon lifetime. The maximum magnetic field ramping rate for a conventional steel electro-magnet is limited by eddy current loss to less than about 200T/sec. At least, time of the order of msec to reach the high magnetic field is needed, which is too long for accelerating muons within their lifetimes. A ferrite magnet has a 100 times larger maximum magnetic field ramping rate, but the maximum attainable magnetic field strength is about 0.1 T or less, making the ring size very big. Thus, we consider that a static magnetic field must be used in ring accelerators for muon acceleration.

The cyclotron is inadequate for accelerating muons to high energy. Keeping isochronous in this type of accelerator becomes rather difficult when accelerating relativistic particles. The FFAG (fixed-field alternating gradient) accelerator should be ideal for accelerating muons to high energy.

The FFAG is a strong focusing type of synchrotron having a static magnetic field. The concept of the FFAG accelerator was proposed by Ohkawa in 1953.[11] In the early 1960s, this type of accelerator was widely studied and small electron models were developed mostly in North America under the MURA project.[12] However, no practical FFAG had ever been built until recently.

In 1999, development of the proton model of the FFAG accelerator (POP model) was started at KEK and the first proton beam acceleration was successfully achieved in June of 2000[13].

A big advantage of the FFAG accelerator for accelerating short lived particles such as muons is that the beam guiding magnetic field is static. The acceleration time can be short enough to eliminate the particle decay if the rf voltage is large enough. Contrary to electron acceleration, acceleration of a heavy particle such as the proton in an FFAG accelerator is rather difficult, because the rf accelerating system must have a frequency modulation that matches the varying beam revolution time. In order to produce frequency modulation, a low frequency rf cavity inductive material such as ferrite has been used in the ordinary proton synchrotron. Since the bandwidth of ferrite is, however, rather small and the rf loss caused by hysteresis becomes very large at a field more than several hundred gauss, the ferrite loaded type of cavity is totally inadequate for the FFAG accelerator.

A new type of broadband rf cavity using a soft magnetic alloy (MA cavity) has been developed at KEK. The bandwidth of this type of rf cavity is very broad because of its small Q-value (Q<1). The attainable rf field strength becomes very large compared with that of ferrite which has been widely used as the inductive material for the proton synchrotron

Another advantage of the FFAG accelerator is that it has a large acceptance for both transverse and longitudinal directions. The horizontal accep-

tance of the FFAG accelerator is very large and normally exceeds 10000πmm·mrad in real phase space. The momentum acceptance is also very large and a beam having a large momentum spread of more than $\pm50\%$ can be accelerated. Thus, both muon cooling and, accordingly, phase rotation should not be necessary. That should be a straightforward option for muon acceleration in the neutrino factory.

In the FFAG accelerators, there are two different types from the beam dynamics point of view; one is the scaling type and the other the non-scaling type. In the scaling type of FFAG accelerator, the beam orbit scales for different energies, which means that the betatron tunes for both horizontal and vertical directions are always constant during acceleration. This is the so-called "zero-chromaticity" condition.

3.1.4   The Japanese Neutrino Factory

A preliminary layout of the neutrino factory of the FFAG version at the J-PARC is shown in Fig.3.3. The accelerators must be located deep underground. Since the practical momentum range from injection to extraction in the FFAG accelerator is about 3 to 4 times, there are four FFAG rings for each ring will be described later but the basic beam parameters for each one are summarized in Table 3.1.4.

Table 3.1: Main parameters of FFAG accelerator complex.

momentum (GeV/c)	0.3 to 1 (normal)	0.3 to 1 (super)	1 to 3 (normal)	1 to 3 (super)	3 to 10	10 to 20
average radius (m)	21	10	80	30	90	200
number of sector	32	16	64	32	64	120
k value	50	15	190	63	220	280
beam size at extraction(mm)	170×55	143×55	146×41	115×25	93×17	104×34

In this FFAG based neutrino factory, the expected muon intensity after acceleration exceeds more than 3×10^{20} muons/year with the 50 GeV and 1MW proton driver and about 1×10^{20} muon/decays/year/straight in the muon storage ring can be realized.[1] If the 50 GeV proton driver is upgraded to reach the beam power of 4 MW as described below, the more than 4×10^{20} muon decays/year/straight becomes possible.

In the following sections the preliminary design of FFAG-based neutrino factory is discussed.

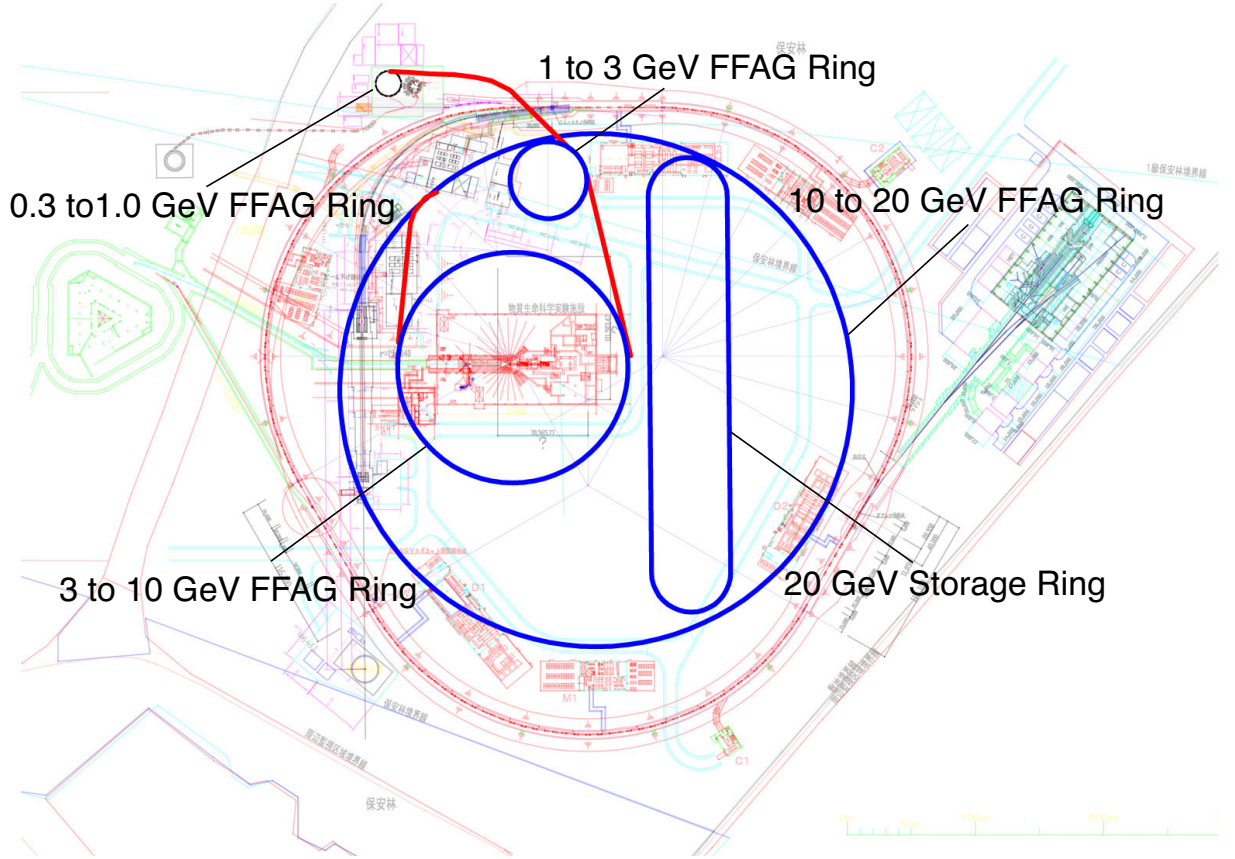[1]The fraction of the one long straight section is about 0.3.

Figure 3.3: Schematic layout of a FFAG-based neutrino factory at the Tokai campus

3.2 Pion Capture

The proton beam extracted from the proton driver is brought to the target and capture section. In the present design of the capture section, pion capture with superconducting solenoid magnets is employed. In this scheme, the issues to be considered in the FFAG scenario are the following two points.

1. Optimization of the Momentum range of pions

2. Realization of the Targetry, for instance

   - A superconducting solenoid magnet under a strong radiation environment.
   - A pion production target for huge energy dissipation.[2]

---

[2]typical power dissipation in the target is about 10∼15% of beam energy

The second one is common among the different neutrino factory scenarios[2, 3]. On the other hand, the first one is a proper issue for individual neutrino factory scenario. Thus, this note concentrates on the beam characteristics.

3.2.1 Geometry of pion production system

The hadron interaction in the production target was simulated by MARS14(00) which was developed by FNAL .The particle transport in the solenoid channel was simulated by GEANT3.14 for the events generated by MARS. Fig. 3.4 shows the setup used in the capture simulation.

In that study, as a typical capture field configuration, a field strength of 20 T (inner bore radius: 8cm) was taken for the capture solenoid. For the transport channel, 5 T (inner bore radius: 16cm) solenoid was assumed.
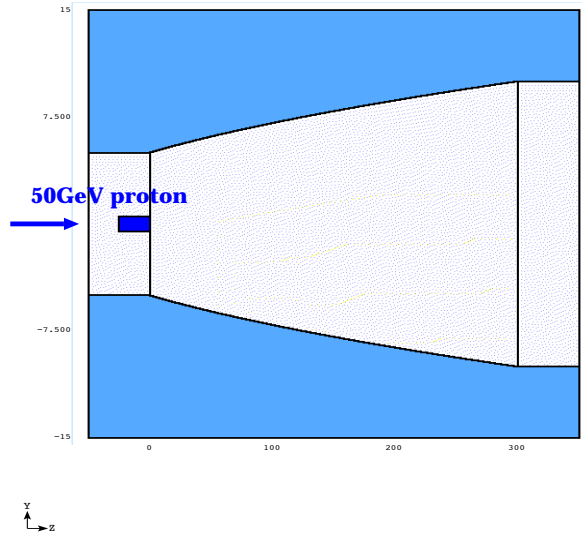

Figure 3.4: Schematic view of the setup for the pion capture simulation

As a typical target material, tungsten is employed. The dimension of the target is 0.5 cm (radius) × 20 cm (length). Here, the target length is 20cm, which corresponds to 2 nuclear interaction lengths of tungsten. The yield of secondary particles reaches its maximum at the almost center of the target. It should be noted that the target material species do not affect the spectrum of secondary particles so much but change the absolute yield. Considering the heat load in the production target, a graphite target, which is light material and is more tolerable against huge energy dissipation, is likely to be realistic. In the case of a graphite target, the only major difference is absolute yield. The yield reduces about 40% of that with a tungsten target.

Thus, except the absolute yield, the following discussion with a typical target material (tungsten) is valid.

3.2.2 Pion and muon production

Before going to the detail of the capture scheme, initial distribution at the exit of solenoid capture channel is presented.

Fig.3.5 shows typical momentum distribution of pions and muons together at 15-m downstream of the production target. The maximum transverse momentum of the pions captured is 0.24 GeV$/c$ $(= 0.3 \times 20(\text{T}) \times 0.08(\text{m})/2)$ The momentum is peaked around 150 MeV$/c$. The peak consists of mostly relatively low energy muons, and the pions are peaked around 250 MeV$/c$. In the case, the yield of the captured pions is about 1.2 /one 50-GeV proton.

Given the downstream acceptance, in comparison to the case without a magnetic field, the accepted increase in the momentum region less than 1 GeV$/c$. Above 1 GeV$/c$, there is no apparent increase. In the beam momentum region higher than 1GeV$/c$, the conventional horn magnet will be more effective.
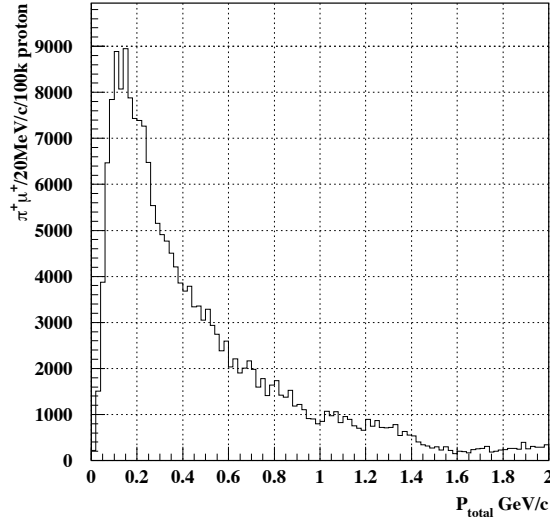

Figure 3.5: Momentum distribution of pions and muons at 10m downstream from the production target.

3.2.3 Capture of pions at high energy

As emphasized, in the FFAG scenario, phase rotation and muon ionization cooling are not mandatory, because of large transverse acceptance of FFAG. In addition, the momentum range of the muons accepted would be as large as ± 50 % in $\Delta p/p$, due to a large RF bucket.

Suppose we omit the muon ionization cooling, we have a freedom to choose the central momentum of the pions/muons to be accepted. In the ordinary scheme, the momentum range of pions/muons accepted is about $200-300$ MeV$/c$. If the momentum acceptance of $\Delta p/p$ to be typically $\sim 50\%$ is

fixed, the absolute momentum width gets larger, as the central momentum gets higher. As a result, even if the muon momentum distribution is peaked at 200 MeV/c (see Fig.3.5), the muon yield could increase when the higher central momentum is selected.

The muon yields with fixed momentum acceptance ($\Delta p/p$=0.5) were estimated by varying the central muon momentum. Fig.3.6 shows the muon yields, where the transverse phase space acceptance of 10000 πmm·mrad was applied. It should be noted that the unnormalized emittance was employed to apply the emittance cuts. From Fig.3.6, the muon yield reaches its maximum around the central energy of 0.9 GeV/c. The optimum energy tends to get lower, as the emittance cut point gets larger. For example, in the case of emittance cut of 20000 πmm·mrad., the optimum central momentum is about 0.6 GeV/c.
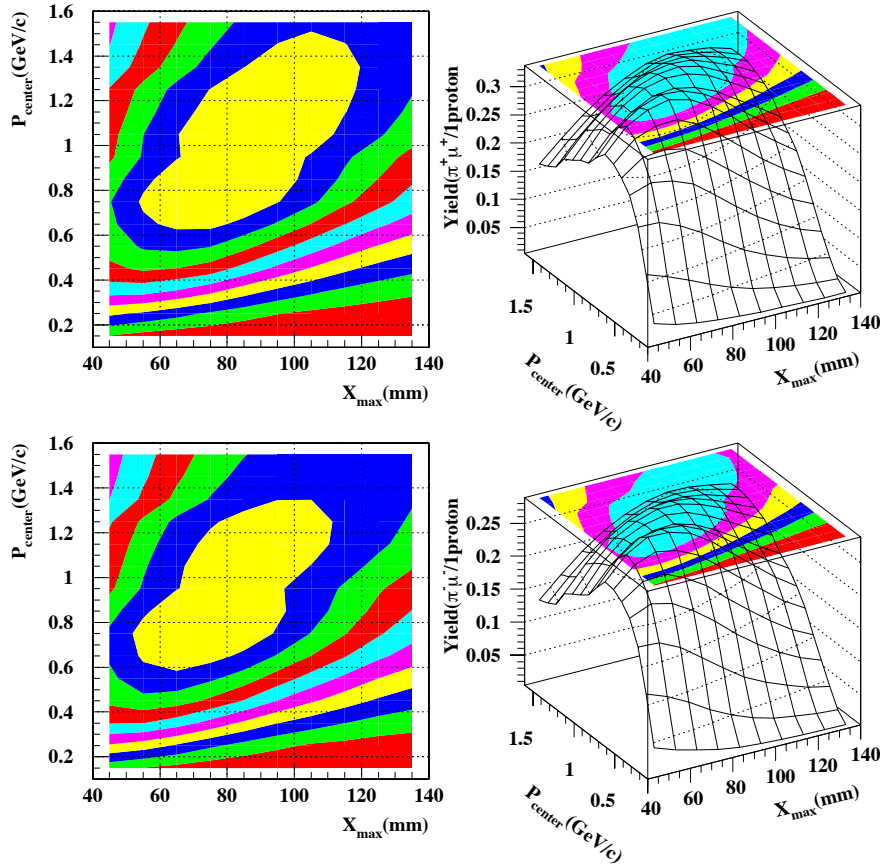

Figure 3.6: Muon and pion yield with fixed transverse acceptance, The top two figures : $\mu^+ + \pi^+$, the bottom two figures : $\mu^- + \pi^-$

In the geometry thus considered, the muon yields per one 50 GeV proton incident are ~0.3, ~0.5 for the case of emittance cut of 10000 πmm·mrad, and 20000πmm·mrad., respectively. It would give a sufficiently high yield.

Therefore, if the phase rotation and muon cooling stages can be skipped, the high energy capture might be an option. Another merit of the high energy capture is that the phase-slip due to the wide momentum spread is less serious compared to the lower energy case, since the velocity of the particles of interest is close to the speed of light (c). As shown in Fig.3.2, in high energy capture, the longitudinal emittance is about 4.6 eV·sec.

3.3   Muon Acceleration

Quick acceleration of muon beams becomes possible with a Fixed Field Alternating Gradient (FFAG) synchrotron and high voltage rf cavity such as 1 MV/m on average with very low frequency. We plan to capture muons with the central momentum of 0.3 GeV/c as discussed in the previous section. Large momentum acceptance of a FFAG ring makes it possible to accommodate the momentum spread of $\pm 50\%$ and to accelerate a beam up to the final momentum without any beam cooling.

There are several arguments what the optimized momentum is from the physics point of view. Nevertheless, 20 GeV/c is the upper bound if the whole accelerator complex should be fit in the area enclosed with 50 GeV PS in JAERI site. The final momentum is rather arbitrary within the range of 10 to 50 GeV/c. There are several arguments what the optimized momentum is from the physics point of view. Nevertheless, 20 GeV/c is the upper bound if the whole accelerator complex should be fit in the area enclosed with 50 GeV PS in JAERI site.

In order to accelerate muon beams from 0.3 GeV/c to 20 GeV/c, we have designed four FFAG rings, which are connected in cascade. The first ring accelerates muons from 0.3 GeV/c to 1 GeV/c, followed by the second one of 1 GeV/c to 3 GeV/c, the third one of 3 GeV/c to 10 GeV/c, and the final one of 10 GeV/c to 20 GeV/c. The momentum ratio of each injection and extraction is about 3 except for the final ring. That is a moderate design and gives small orbit excursion, say 0.5m.

3.3.1   0.3 to 1GeV/c FFAG

The first (and second) FFAG accelerator can be either normal conducting magnet FFAG or superconducting one. The main difference exists in a bending strength and an average radius. They are 1.8T and 21m, respectively, for normal conducting and 2.8T and 10m, respectively, for superconducting. Fig. 3.7 and 3.8 show a footprint of the normal conducting version and its lattice functions in one sector and those for superconducting one, respectively. Table 3.2 summarizes the main parameters.

Obviously the normal conducting one has more cells, twice as many, although the length of each cell is about the same for two versions, that is 4 meters, resulting in the similar maximum value of beta functions. The

dispersion function of the superconducting version is 50% more.

Table 3.2: Main parameters of 0.3 to 1 GeV/c FFAG.

	normal conducting	superconducting
number of sector	32	16
k value	50	15
transition gamma	7.1	4
orbit excursion	0.50 m	0.77 m
average radius	21 m	10 m
B@F/D	1.8 T	2.8 T
F/2 angle	0.026 rad	0.052 rad
D angle	0.018 rad	0.036 rad
F/2 bend angle	17 degree	26 degree
packing f	0.45	0.46
phase advance(H/V)	120/61 deg.	131/103 deg.
drift length	2.060 m	2.120 m
BF length	1.104 m	1.065 m
BD length	0.382 m	0.367 m

3.3.2   1 to 3 GeV/c FFAG

The second FFAG can be also either normal or superconducting magnet. The field strength of the normal conducting magnet is 1.8T and that of superconducting one is 3.6T. The number of sector in the normal one is twice as much compared with superconducting one. Fig. 3.9 and 3.10 show a footprint of the normal conducting version and its lattice functions in one sector and those for superconducting one, respectively. Table 3.3 summarizes main parameters.

3.3.3   3 to 10GeV/c FFAG

The third one will be superconducting magnet FFAG because the normal conducting version becomes too large to fit in the area enclosed with 50 GeV PS. Fig. 3.11 shows a footprint of the superconducting version and its lattice functions in one sector. Table 3.4 summarizes main parameters.

3.3.4   10 to 20 GeV/c FFAG

By the same reason of the preceding ring, the final FFAG will use super-conducting magnet. Furthermore, the 20 GeV/c is the maximum available energy if we set a limit on the magnet strength of 6.0T and average radius of
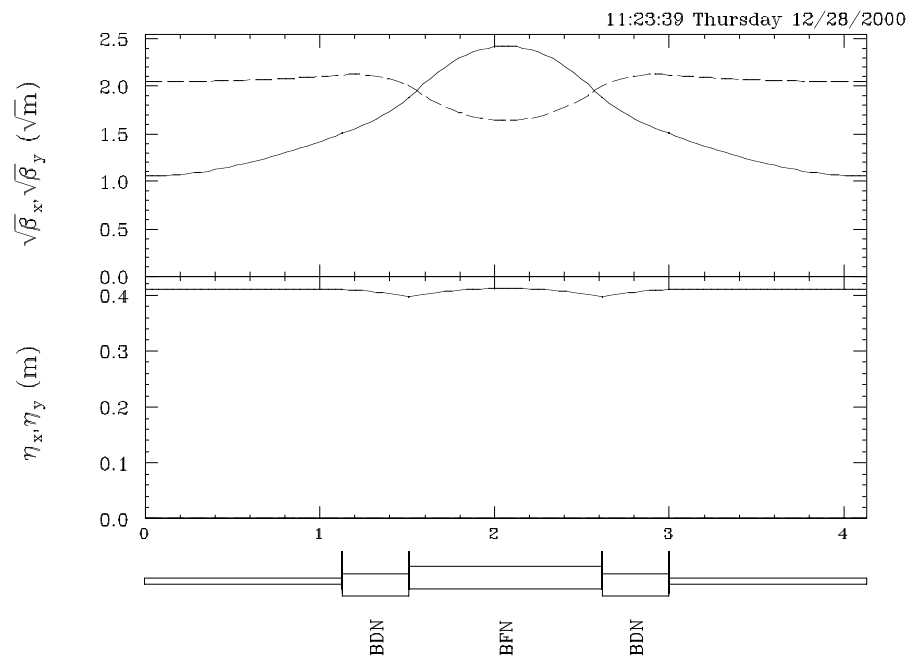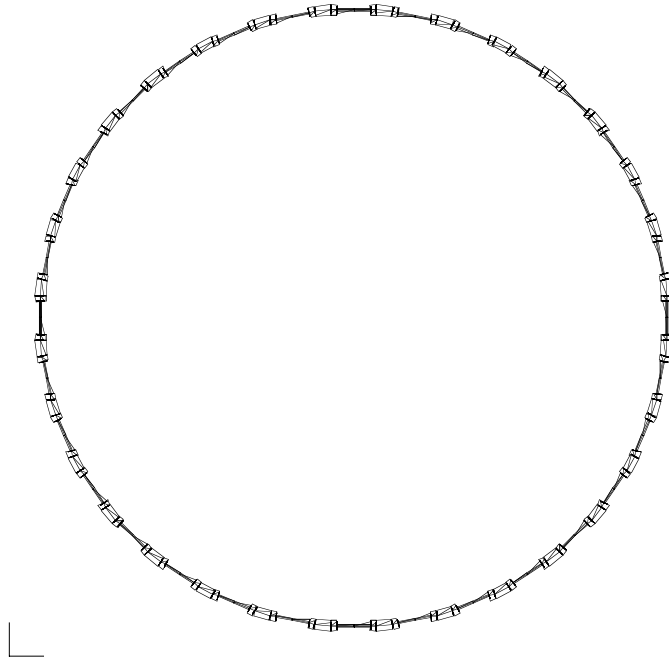
Figure 3.7: 0.3 to 1 GeV/c FFAG accelerator with normal conducting magnets.

Table 3.3: Main parameters of 1 to 3 GeV/c FFAG.

	normal conducting	superconducting
number of sector	64	32
k value	190	63
transition gamma	13.8	8
orbit excursion	0.46 m	0.52 m
average radius	80 m	30 m
B@F/D	1.8 T	3.6 T
F/2 angle	0.0127 rad	0.026 rad
D angle	0.0093 rad	0.018 rad
F/2 bend angle	10.5 degree	16 degree
packing f	0.45	0.45
phase advance(H/V)	132/33 deg.	154/46 deg.
drift length	4.325 m	3.229 m
BF length	2.041 m	1.575 m
BD length	0.747 m	0.544 m

Table 3.4: Main parameters of 3 to 10 GeV/c FFAG.

	superconducting
number of sector	64
k value	220
transition gamma	14.9
orbit excursion	0.49 m
average radius	90 m
B@F/D	5.4 T
F/2 angle	0.012 rad
D angle	0.009 rad
F/2 bend angle	10 degree
packing f	0.43
phase advance(H/V)	157/23 deg.
drift length	5.046 m
BF length	2.169 m
BD length	0.813 m

150m, which is the requirement to locate the machine in the area inside the 50 GeV PS. Fig. 3.12 show a footprint of the superconducting version and its lattice functions in one sector. Table 3.5 summarizes main parameters.

Table 3.5: Main parameters of 10 to 20 GeV/c FFAG.

	superconducting
number of sector	120
k value	280
transition gamma	16.8
orbit excursion	0.49 m
average radius	200 m
B@F/D	6.0 T
F/2 angle	0.0067 rad
D angle	0.0053 rad
F/2 bend angle	6.8 degree
packing f	0.46
phase advance(H/V)	67/19 deg.
drift length	5.668 m
BF length	2.685 m
BD length	1.062 m

3.4   Storage Ring

A storage ring is designed and main parameters are listed in Table 3.6. It has two of approximately 300 m straight sections. At the straight section, beam size is enlarged and the rms divergence of beams becomes 0.92. That satisfies the condition of

$$D_{beam} < \frac{1}{5\gamma}, \qquad (3.1)$$

where γ is a relativistic Lorentz factor.

Table 3.6: Muon Storage Ring Design Parameters and Constraints

Storage Ring Geometry		racetrack
Storage Ring Energy	GeV	20
$\epsilon(100\%)$ (normalized)	mm·mrad	30,000π
$\Delta p/p$ (%)	%	1
maximum poletip field	T	<5.0
arc cell phase advance	deg	90

Table 3.7: Parameters of the large-momentum acceptance arc cells for a 20-GeV muon storage ring

General: tungsten shield thickness	cm	1.0
beam-stay clear	cm	1.0
inter-magnet spacing	m	0.75
Dipoles:		
dipole length	m	2.4
dipole bend	rad	0.1654
dipole field	T	4.6
beam size (6σ, max), W$\times$H	cm	12.8$\times$5.3
dipole full aperture**, W$\times$H	cm	14.8$\times$9.3
sagitta	cm	2.67
Quadrupoles:		
quadrupole length	m	1
arc quadrupole strength	m^{-2}	.3
arc quadrupole poletip field	T	1.8
beam size (6σ), W$\times$H		
F quad	cm	13.2$\times$4.3
D quad	cm	6.2$\times$5.0
arc quadrupole bore**	cm	18
Sextupoles (overlay on quad field)		
horiz. sextupole strength	m^{-2}	0.26
vert. sextupole strength	m^{-2}	0.51
horiz. sextupole poletip field	T	0.14
vert. sextupole poletip field	T	0.27
Arc FODO cell parameters:		
cell length	m	9.8
cell phase advance	deg	90
β_{max}	m	16.2
$D_x(max)$	m	2.2
total number arc cells		15
total number disp. sup. cells		8

09:51:49 Friday 09/29/2000
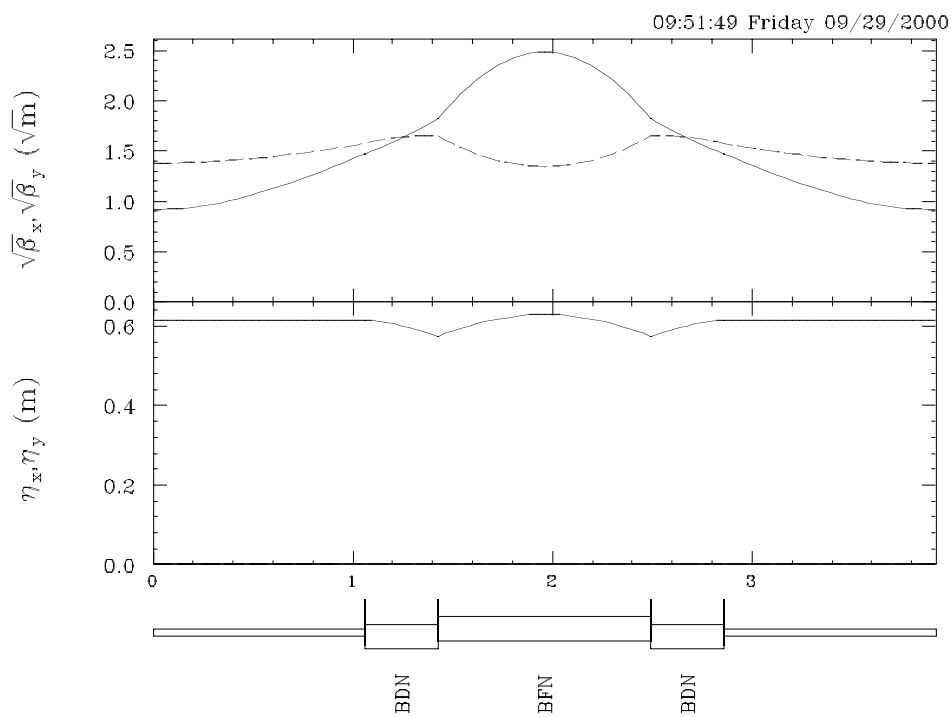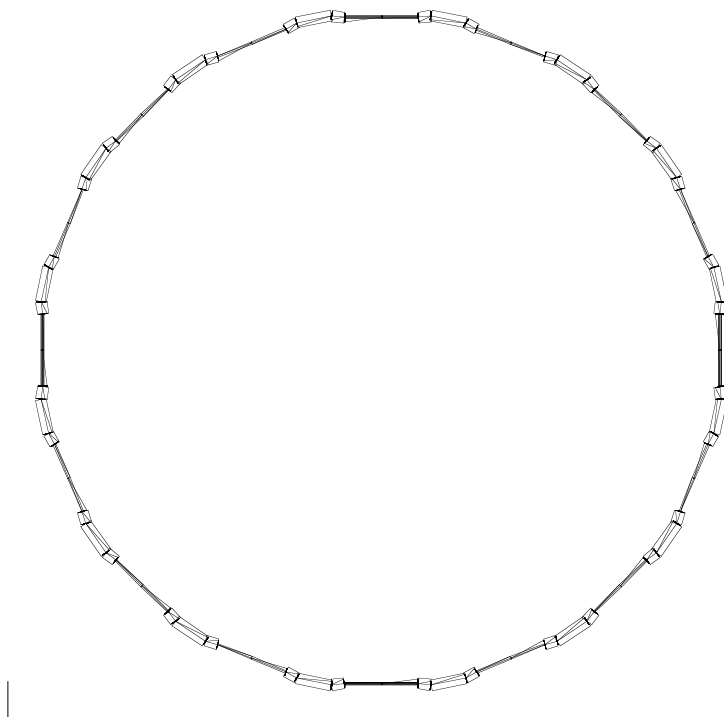
Figure 3.8: 0.3 to 1 GeV/c FFAG accelerator with superconducting magnets.
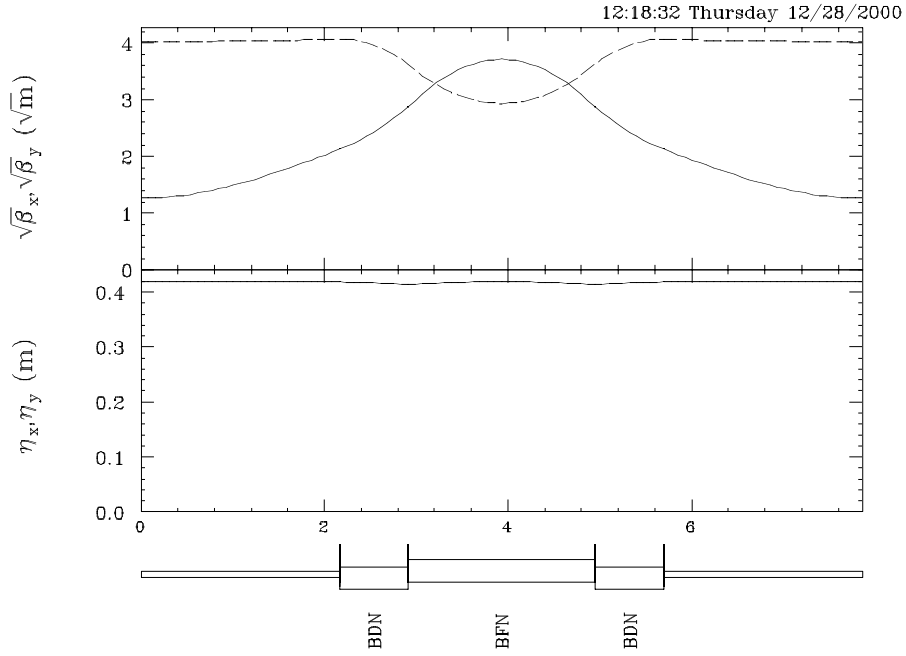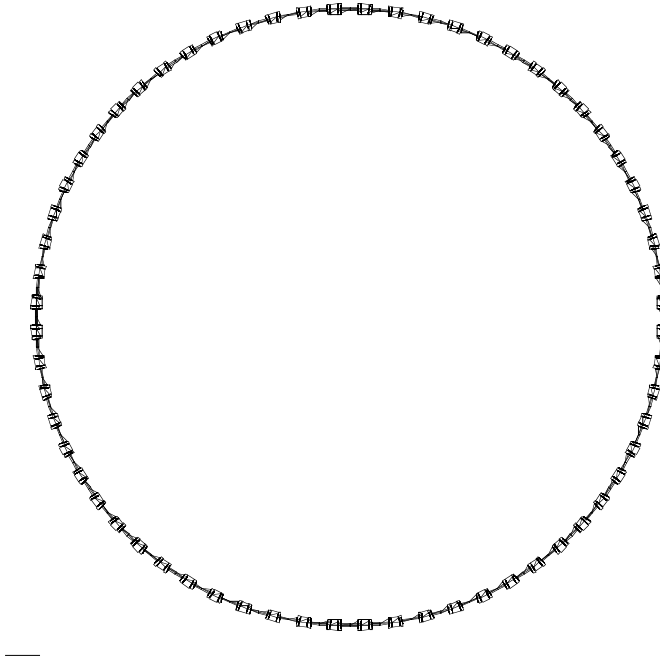
Figure 3.9: 1 to 3 GeV/c FFAG accelerator with normal conducting magnets.

31
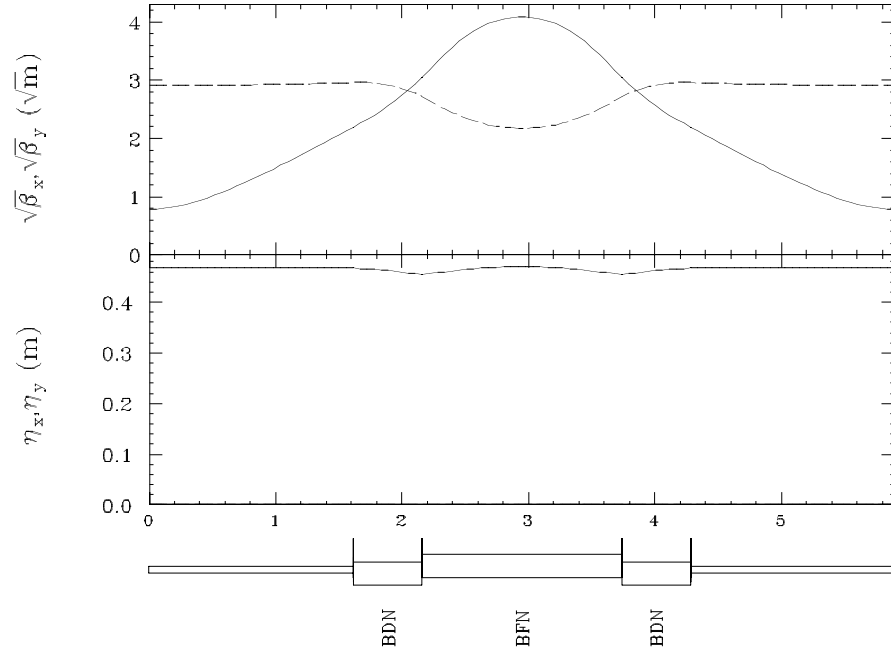
Figure 3.10: 1 to 3 GeV/c FFAG accelerator with superconducting magnets.

$\sqrt{\beta}_x, \sqrt{\beta}_y$ ($\sqrt{\mathrm{m}}$)

η_x, η_y (m)

BDN   BFN   BDN
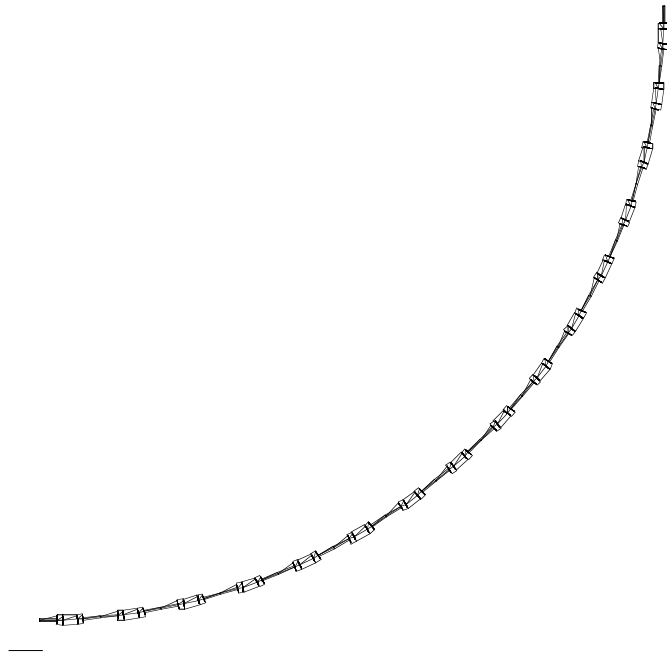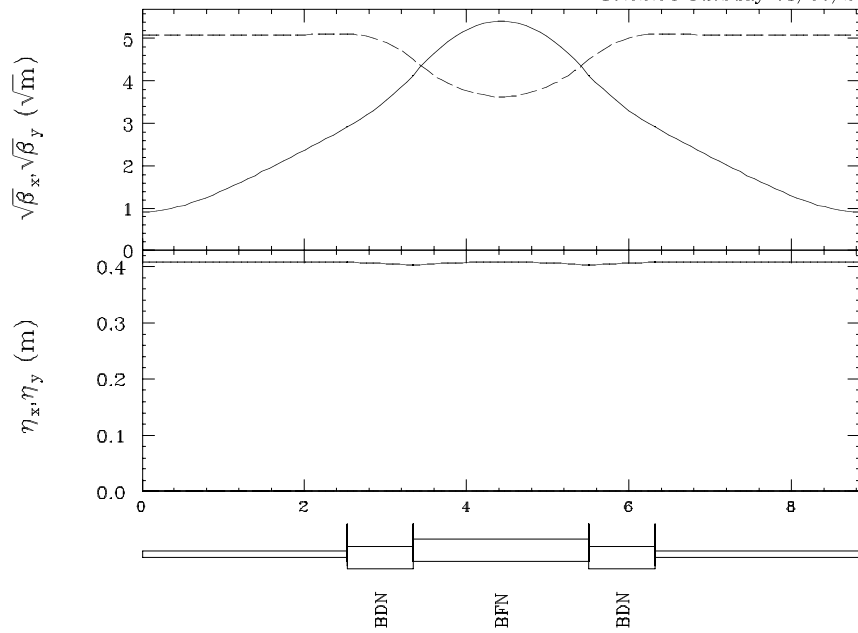
Figure 3.11: 3 to 10 GeV/c FFAG accelerator with superconducting magnets.
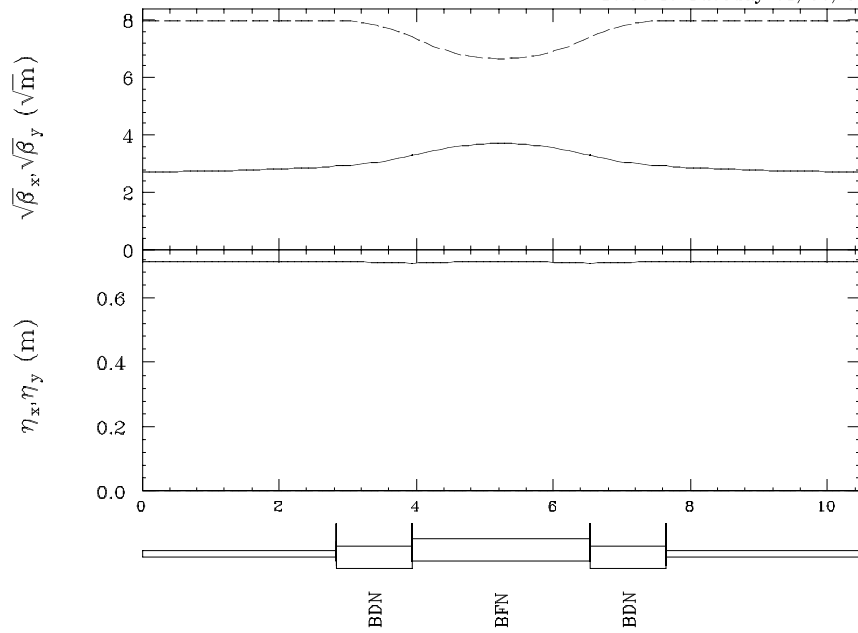
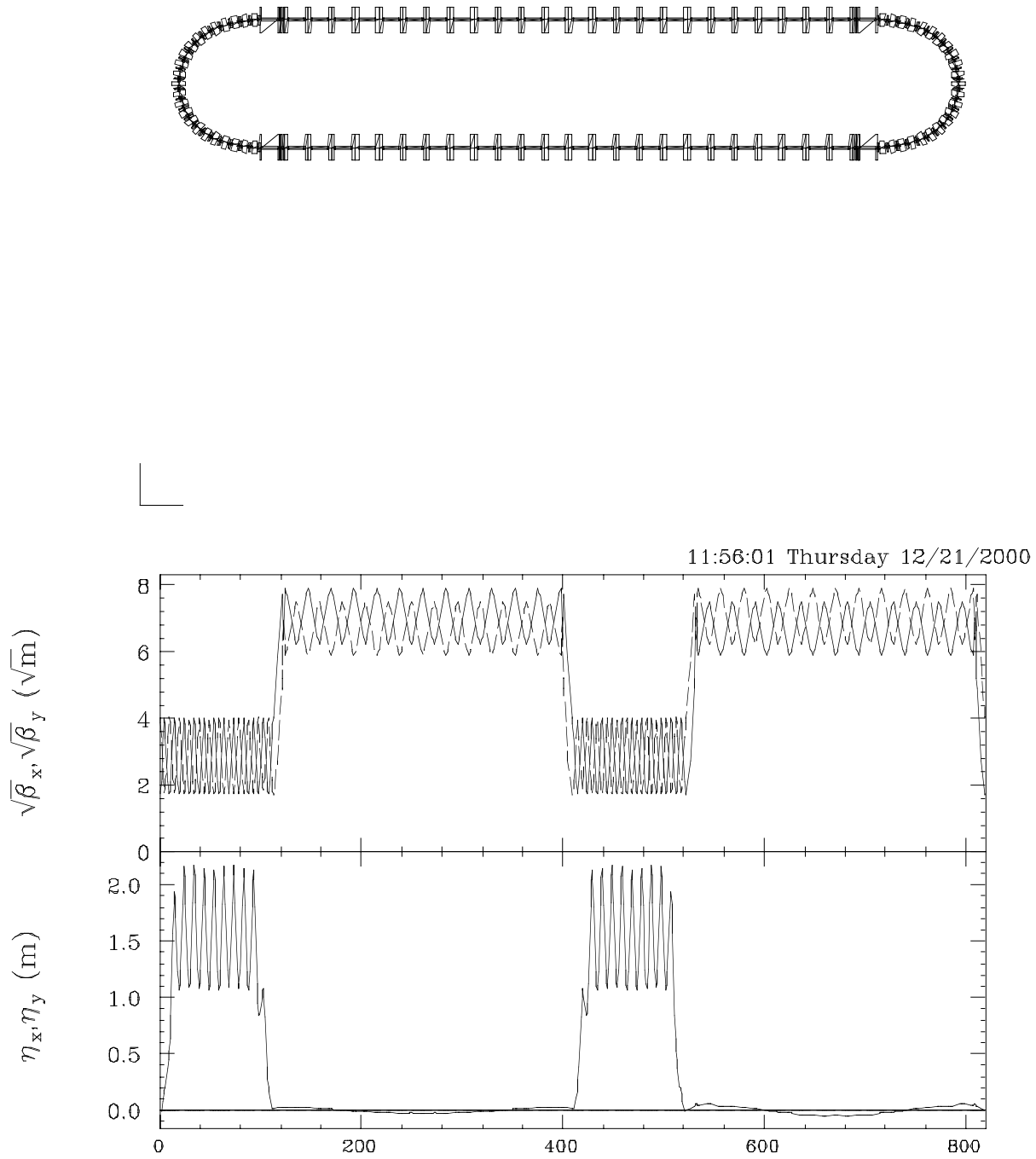Figure 3.12: 10 to 20 GeV/c FFAG accelerator with superconducting magnets.

34

Figure 3.13: Muon storage ring design.

35

Table 3.8: Parameters of the high-beta cells for neutrino production in a 20-GeV muon storage ring

drift length	m	7.4
quadrupole length	m	3
quadrupole strength	m^{-2}	0.016
quadrupole poletip field	T	0.12
quadrupole bore	cm	24
total cell length	m	22.8
cell phase advance	deg	$\approx 4 - 5$
β_{max}	m	62.6
rms divergence	mr	0.92
number of high-beta cells		12

Table 3.9: Storage Ring Parameters at 20-GeV

Circumference	m	819.0
Neutrino decay fraction		33.4%
Production region:		
matching	m	23.2
High-β FODO straight	m	273.6
$\beta_{xmax}/\beta_{ymax}$	m	62.6/56.2
$\nu_x/\nu y$		8.26/8.17
natural chromaticity		-10.4/-10.5

Chapter 4

Physics

4.1 Neutrino Oscillation Phenomenology

There have been several experiments [21, 22, 23, 24, 25, 26, 27, 28, 29, 30, 31, 32] which suggest neutrino oscillations [33, 34].

It has been shown in the two flavor framework that the solar neutrino mixing can be explained by neutrino oscillation with the set of parameters $(\Delta\, m_\odot^2, \sin^2 2\theta_\odot) \simeq (\mathcal{O}(10^{-5}\mathrm{eV}^2), \mathcal{O}(10^{-2}))$ (SMA (small mixing angle) MSW solution), $(\mathcal{O}(10^{-5}\mathrm{eV}^2), \mathcal{O}(1))$ (LMA (large mixing angle) MSW solution), $(\mathcal{O}(10^{-7}\mathrm{eV}^2), \mathcal{O}(1))$ (LOW solution) or $(\mathcal{O}(10^{-10}\mathrm{eV}^2), \mathcal{O}(1))$ (VO (vacuum oscillation) solution). Among these, recently KamLAND has confirmed that the LMA MSW solution would be most likely. On the other hand, the atmospheric neutrino mixing can be accounted for by dominant $\nu_\mu \leftrightarrow \nu_\tau$ oscillations with $(\Delta m_\mathrm{atm}^2,\ \sin^2 2\theta_\mathrm{atm}) \simeq (10^{-2.5}\mathrm{eV}^2, 1.0)$.

In the three flavor framework there are two independent mass squared differences and it is usually assumed that these two mass differences correspond to $\Delta m_\odot^2$ and Δm_atm^2. Throughout this report we will assume three neutrino species which can account for only the solar neutrino deficit and the atmospheric neutrino mixing [1]. Without loss of generality we assume $|\Delta m_{21}^2| < |\Delta m_{32}^2| < |\Delta m_{31}^2|$ where $\Delta m_{ij}^2 \equiv m_i^2 - m_j^2$. The flavor eigenstates are related to the mass eigenstates by $U_{\alpha j}$ ($\alpha = e, \mu, \tau$), where $U_{\alpha j}$ are the elements of the MNS mixing matrix U [34]:

$$\begin{pmatrix} \nu_e \\ \nu_\mu \\ \nu_\tau \end{pmatrix} = U \begin{pmatrix} \nu_1 \\ \nu_2 \\ \nu_3 \end{pmatrix},$$

$$U \equiv \begin{pmatrix} U_{e1} & U_{e2} & U_{e3} \\ U_{\mu 1} & U_{\mu 2} & U_{\mu 3} \\ U_{\tau 1} & U_{\tau 2} & U_{\tau 3} \end{pmatrix}$$

---

[1]To explain the LSND mixing [32] one would need at least four neutrino species.

$$
= \begin{pmatrix}
c_{12}c_{13} & s_{12}c_{13} & s_{13}e^{-i\delta} \\
-s_{12}c_{23} - c_{12}s_{23}s_{13}e^{i\delta} & c_{12}c_{23} - s_{12}s_{23}s_{13}e^{i\delta} & s_{23}c_{13} \\
s_{12}s_{23} - c_{12}c_{23}s_{13}e^{i\delta} & -c_{12}s_{23} - s_{12}c_{23}s_{13}e^{i\delta} & c_{23}c_{13}
\end{pmatrix}.
$$

With the mass hierarchy $|\Delta m_{21}^2| \ll |\Delta m_{32}^2|$ there are two possible mass patterns which are depicted in Fig. 4.1, depending on whether Δm_{32}^2 is positive or negative.
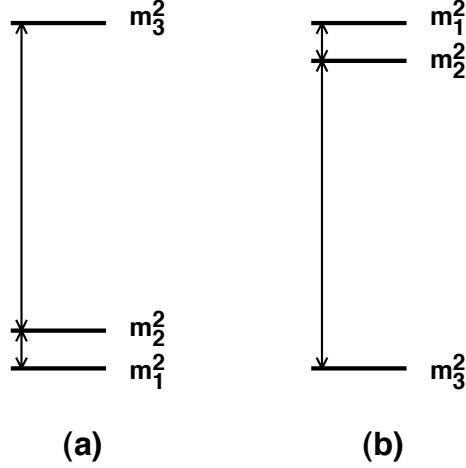

Figure 4.1: Two mass patterns. (a), (b) correspond to $\Delta m_{32}^2 > 0$, $\Delta m_{32}^2 < 0$, respectively.

It has been shown in the three flavor framework [36, 37, 38] that combination of the CHOOZ reactor data [39] and the atmospheric neutrino data implies small θ_{13}, i.e., $\sin^2 2\theta_{13} < 0.1$ which is essentially the result of the CHOOZ data [2]. When $|\theta_{13}|$ is small, the MNS matrix looks like

$$
U \simeq \begin{pmatrix}
c_\odot & s_\odot & \epsilon \\
-s_\odot c_{\text{atm}} & c_\odot c_{\text{atm}} & s_{\text{atm}} \\
s_\odot s_{\text{atm}} & -c_\odot s_{\text{atm}} & c_{\text{atm}}
\end{pmatrix},
$$

where θ_{12}, θ_{23} have been replaced by $\theta_\odot$ and θ_{atm}, respectively. According to the most up–to–date analysis [41, 42, 43, 44, 45] (See Figs. 4.2 and 4.3), assuming the LMA MSW solution [35], these mixing angles and the mass squared differences satisfy at 3σ and 90%C.L, respectively.

$$
\begin{aligned}
0.25 \leq\ & \tan^2\theta_\odot & \leq 0.9, \\
2.5 \times 10^{-5}\text{eV}^2 \leq\ & \Delta m_{21}^2 & \leq 3.3 \times 10^{-4}\text{eV}^2, (3\sigma) \\
0.92 \leq\ & \sin^2 2\theta_{\text{atm}} & \leq 1.0, \\
1.6 \times 10^{-3}\text{eV}^2 \leq\ & \Delta m_{32}^2 & \leq 3.9 \times 10^{-3}\text{eV}^2. (90\%)
\end{aligned}
$$

---

[2]If one does not include the constraint of the Kamiokande data then one get milder bound on θ_{13}, i.e., $\sin^2 2\theta_{13} \lesssim 0.25$ [40].
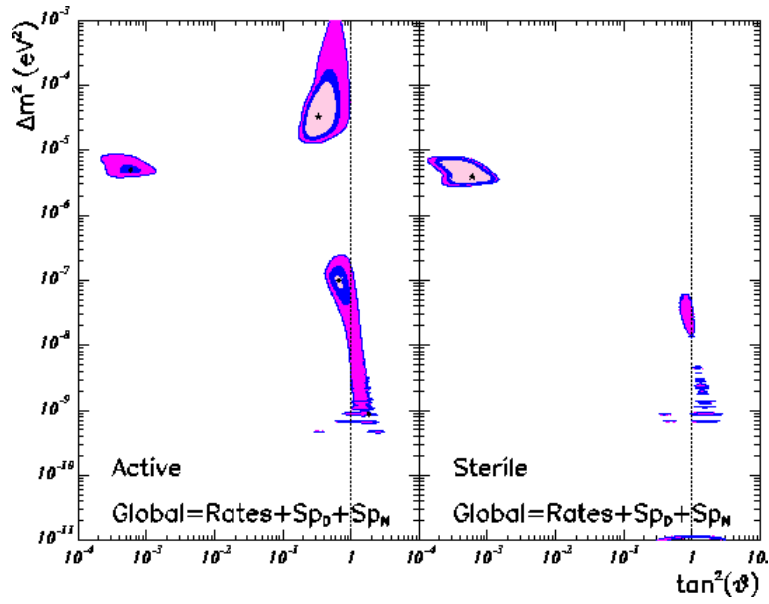
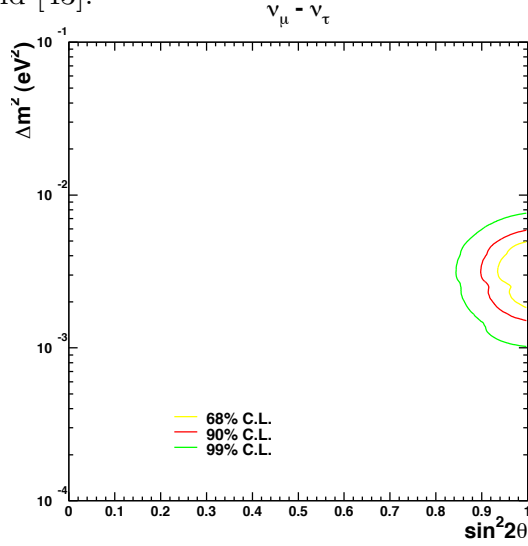Figure 4.2: Results of recent analysis on solar neutrinos [41], which almost agrees with [42] and [43].

Figure 4.3: Allowed region from Superkamiokande contained and partially contained event for $\nu_\mu - \nu_\tau$ oscillations. The figure is from [44].

The measurement of $\theta_\odot \equiv \theta_{12}$ and $\theta_{\mathrm{atm}} \equiv \theta_{23}$ is expected to be greatly improved in the future experiments on solar and atmospheric neutrinos, so the remaining problems in the three flavor framework are to determine (1) the sign of Δm^2_{32}, (2) the magnitude of θ_{13}, (3) the magnitude of the CP phase δ. Recently a lot of research have been done on neutrino factories, [46, 5, 7, 47, 48, 49, 50, 51, 52, 53, 54, 55, 56, 57, 58, 59, 60, 61] and the three problems mentioned above may be solved at neutrino factories. In the following, we discuss these three topics.

4.1.1 Sensitivity to θ_{13}

The main channels which are supposed to be measurable at neutrino factories are $\nu_e \rightarrow \nu_\mu$ and $\bar{\nu}_e \rightarrow \bar{\nu}_\mu$. When the contributions from Δm_{21}^2 are negligible, the appearance probabilities $P(\nu_e \rightarrow \nu_\mu)$ and $P(\bar{\nu}_e \rightarrow \bar{\nu}_\mu)$ are given by (on the assumption of constant density of the matter)

$$
\begin{aligned}
P(\nu_e \rightarrow \nu_\mu) &= s_{23}^2 \sin^2 2\theta_{13}^{M^{(-)}} \sin^2 \left(\frac{B^{(-)}L}{2} \right) \\
P(\bar{\nu}_e \rightarrow \bar{\nu}_\mu) &= s_{23}^2 \sin^2 2\theta_{13}^{M^{(+)}} \sin^2 \left(\frac{B^{(+)}L}{2} \right),
\end{aligned}
\tag{4.1}
$$

where $A \equiv \sqrt{2}G_F N_e$ stands for the matter effect of the Earth, $\theta_{13}^{M^{(\pm)}}$ is the effective mixing angle in matter given by

$$
\tan 2\theta_{13}^{M^{(\pm)}} \equiv \frac{\Delta E_{32} \sin 2\theta_{13}}{\Delta E_{32} \cos 2\theta_{13} \pm A},
$$

and

$$
B^{(\pm)} \equiv \sqrt{(\Delta E_{32} \cos 2\theta_{13} \pm A)^2 + (\Delta E_{32} \sin 2\theta_{13})^2}.
$$

The number of muon decays needed to observe 10 $\nu_e \rightarrow \nu_\mu$ events is shown in Fig. 4.4 as a function of E_μ [47]. As can be seen from Fig. 4.4, the sub–leading contributions from Δm_{21}^2 may be observed in a high intensity neutrino source even if $\theta_{13} = 0$. In the following discussions on the magnitude of θ_{13}, this sub–leading contributions will not be taken into account.

The asymptotic sensitivities to θ_{13} has been studied by taking into account realistic background and efficiencies as well as the spectral information for detectors, or without consideration of backgrounds and systematic errors [60]. It is studied [7] that the sensitivity for a 40 kt magnetized iron calorimeter at L= 732km, 3500km, 7332 km, E_μ=50 GeV with 10^{21} useful muon decays, and it was done [54] for a liquid argon detector at L= 7400 km, E_μ=30 GeV with 10^{20} and 10^{21} useful muon decays (See Fig. 4.6). It was studied [60] that the sensitivity for the case $N_\mu = 2 \times 10^{21}$ kt·yr with correlation of all errors and without the background effect and the systematic errors taken into account. When only the statistical errors are considered, the asymptotic sensitivity to the angle is naively expected to improve at shorter baselines, but it has been shown [7] that background contamination makes the sensitivity poorer at shorter baselines.

The optimum baseline L and muon energy E_μ to measure $\sin^2 2\theta_{13}$ is studied [60] and it was shown that $L \sim 6000$km, $30\text{GeV} \lesssim E_\mu \lesssim 50\text{GeV}$ optimizes the sensitivity to $\sin^2 2\theta_{13}$.

4.1.2 Determination of the sign of Δm_{32}^2

As was mentioned earlier, in the three flavor framework, the mass pattern corresponds to either Fig. 4.1 (a) or (b), depending on whether Δm_{32}^2 is
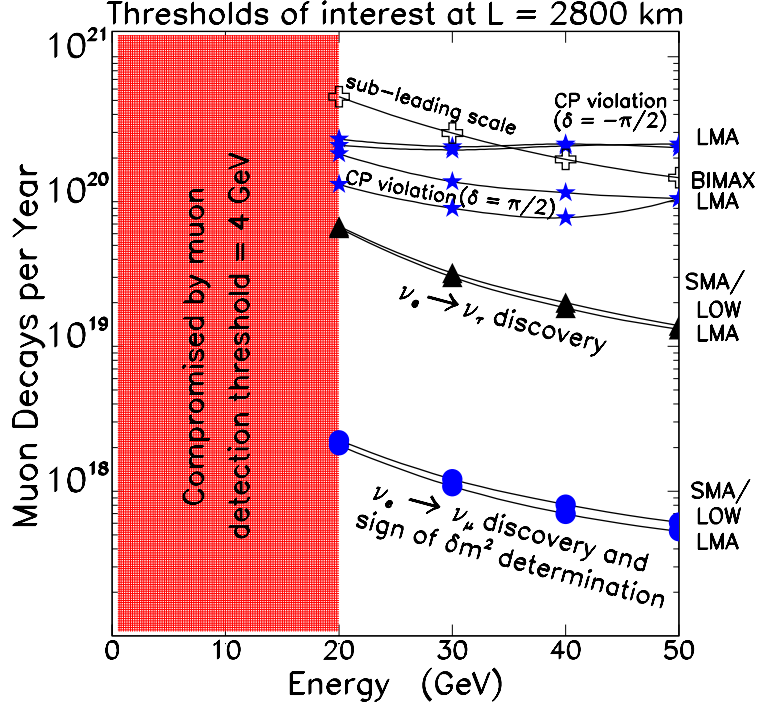
Figure 4.4: The required number of muon decays needed in the beam for the LMA solution and the others for a 50 kt detector (a 5 kt detector in the case of $\nu_e \rightarrow \nu_\tau$ appearance) at L=2800km with a muon detection threshold of 4 GeV [47].

positive or negative. Determination of this mass pattern is important, since Figs. 4.1 (a) and (b) correspond to one and two massive states, assuming that the lowest mass is almost zero. As we can see from (4.1), if $\Delta m_{32}^2 > 0$ then the effective mixing angle $\theta_{13}^{M(-)}$ is enhanced and $P(\nu_e \rightarrow \nu_\mu)$ increases. On the other hand, if $\Delta m_{32}^2 < 0$ then $\theta_{13}^{M(+)}$ is enhanced and $P(\bar{\nu}_e \rightarrow \bar{\nu}_\mu)$ increases. So, at neutrino factories where baseline is relatively large and therefore the matter effect plays an important role, the sign of Δm_{32}^2 can be determined by looking at the difference between neutrino and anti-neutrino events which should reflect the difference between $P(\nu_e \rightarrow \nu_\mu)$ and $P(\bar{\nu}_e \rightarrow \bar{\nu}_\mu)$. The ratio $N(\bar{\nu}_e \rightarrow \bar{\nu}_\mu)/N(\nu_e \rightarrow \nu_\mu)$ is plotted as a function of the baseline L in Fig. 4.9 for E_μ=20GeV [47]. From Fig. 4.9 we observe that we can determine the sign of Δm_{32}^2 for $L \gtrsim$ 2000km.

4.1.3 Precise measurements of the oscillation parameters

Once the wrong sign muons are observed, the next thing to do is to determine the precise values of the mixing angles and the mass squared differences. Cor-
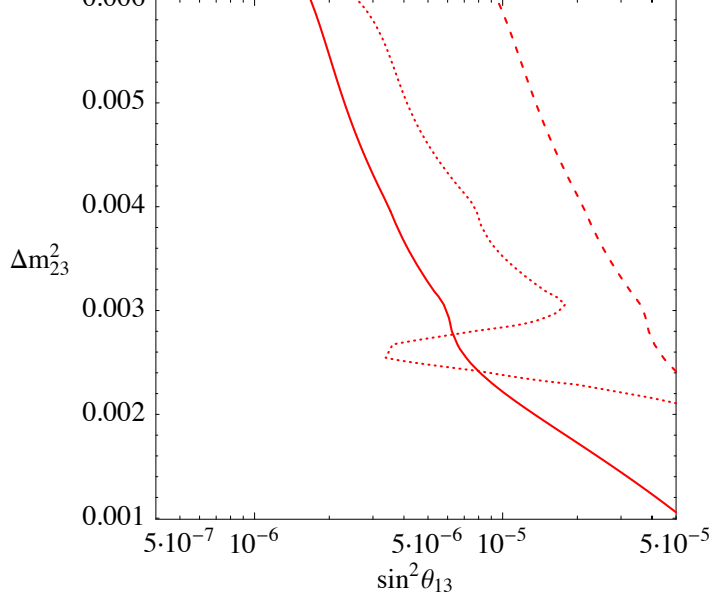
Figure 4.5: The asymptotic sensitivity to $\sin^2\theta_{13}$ as a function of Δm_{23}^2 at 90% CL for a 40 kt magnetized iron calorimeter at $L=$ 732km (dashed lines), 3500km (solid lines), 7332 km (dotted lines), $E_\mu=$50 GeV with 10^{21} useful muon decays [7]. Backgrounds and detection efficiencies are included.

relations of the errors in the mixing angles and the mass squared differences have been studied by several groups.

The correlation of θ_{13} and the matter effect is given in Fig.4.10 for a 40 kt Fe-scintillator detector at a distance $L = 732$km, 3500km, 7332km, $E_\mu = 50$ GeV, 10^{21} muon decays ($\Delta m_{21}^2 = 6 \times 10^{-6}$eV^2, $\sin^2 2\theta_{12}=0.006$) [7]. At 732 km there is no sensitivity to the matter term. At the larger baseline, while the precision in A improves, the precision in θ_{13} gets worse due to the loss in statistics.

The correlation of θ_{13} and θ_{23} is given in Fig.4.11 for a 10 kt ICANOE–type detector at $L=7400$ km with 10^{19}, 10^{20}, 10^{21} μ^+ decays followed by the same number of μ^- decays [54]. In Fig.4.11, the density ρ is either considered as a free parameter (lower plot) or fixed (upper plot) in a fit but there is no much difference.

The correlation of θ_{13} and Δm_{21}^2 is shown in Fig.4.12 [7]. This correlation is potentially large, but the authors of [7] assume that Δm_{21}^2 and θ_{12} are known by the time the neutrino factory will be operational. In fact, Kam-LAND is expected to improve Δm_{21}^2 and θ_{12} with more precision within a few years. Even if the errors in these two parameters of solar neutrino oscillation are as large as 50 %, the effect on the precision in θ_{13} is not so serious and the precision 5 % in θ_{13} can be expected from the analysis of [7].

It was shown [55] that if θ_{13} turns out to be relatively large ($\sin^2 2\theta_{13} \gtrsim 0.01$), by the total number of muons without charge identification, a similar precision in the determination of θ_{13} is obtained as using the wrong–sign muon signal (cf. Fig.4.13).
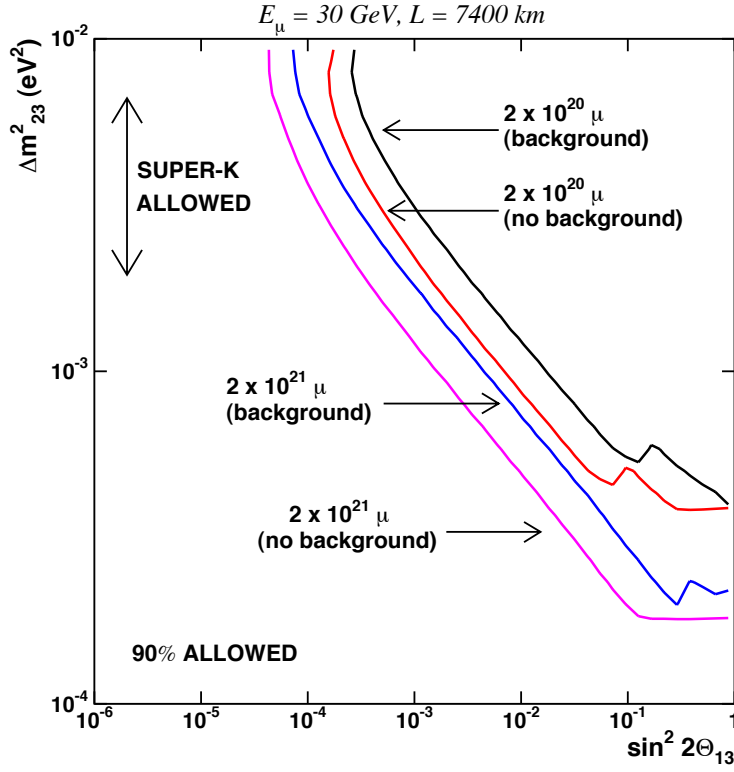
Figure 4.6: The asymptotic sensitivity to θ_{13} for a 10 kt ICANOE–type detector at $L=$ 7400 km, E_μ=30 GeV with 10^{20} and 10^{21} useful muon decays [54]. Backgrounds and detection efficiencies are included.

The correlation of θ_{23} and Δm_{32}^2 is given in Fig.4.9 using disappearance of right-sign muons for E_μ=30 GeV, L=2800 km, 2×10^{20} muon decays [47]. The precision for the Δm_{32}^2 and $\sin^2 2\theta_{23}$ measurements is a few %, which is one order of magnitude better than that expected at MINOS and OPERA.

4.1.4 The measurement of δ

4.1.4.1 CP violation at neutrino factories

For the LMA MSW solution which has been confirmed by KamLAND, CP violation may be large enough to be measured. This fact gives us a hope for measurements of CP violation.

There have been a lot of works on CP violation at neutrino factories [46, 5, 7, 47, 48, 49, 50, 51, 52, 53, 54, 56, 57, 58, 59, 60, 61]. Some of earlier works [49, 50, 51] used an asymmetry parameter between ν and $\bar\nu$ after subtracting the matter effect, and some [56, 57] discussed T violation. Most of these works concluded that the baseline $L \sim$3000km and the muon energy $E_\mu \sim$50GeV optimizes the signal. On the other hand, there have
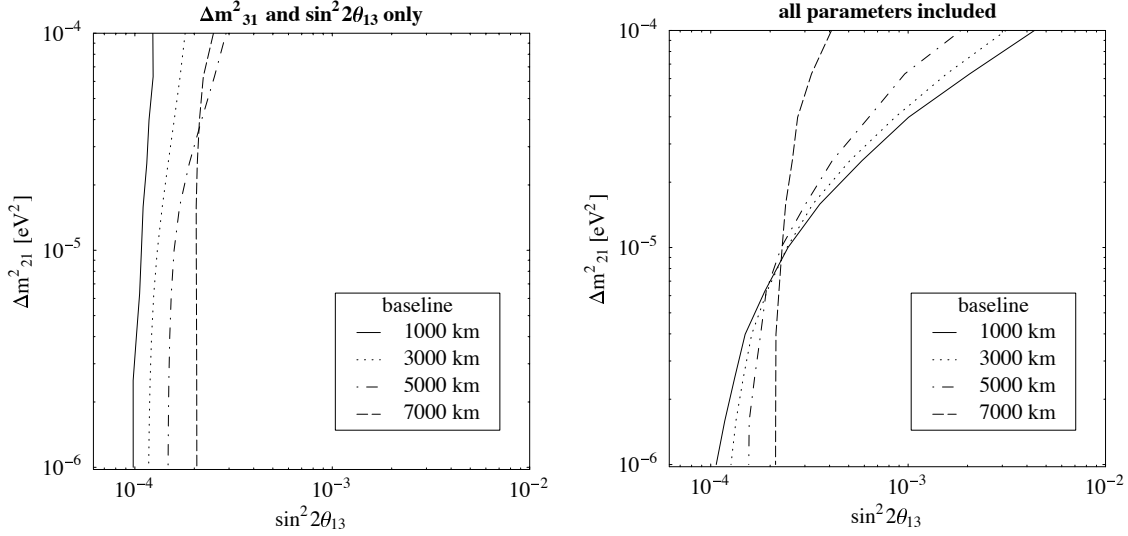
Figure 4.7: Sensitivity reach for measurements of $\sin^2 2\theta_{13}$ [60]. The area to the left of the lines indicates the parameter range where measurements are compatible with $\sin^2 2\theta_{13} = 0$ at 99% C.L. The calculation was performed with a beam energy of 50GeV. The different line types are for different baseline as explained in the legend. For comparison to older studies, the left panel displays the result obtained from a two parameter fit of only $\sin^2 2\theta_{13}$ and Δm_{31}^2. Backgrounds and experimental uncertainties are not taken into account. The right panel displays the result of [60] with all parameters taken into account.
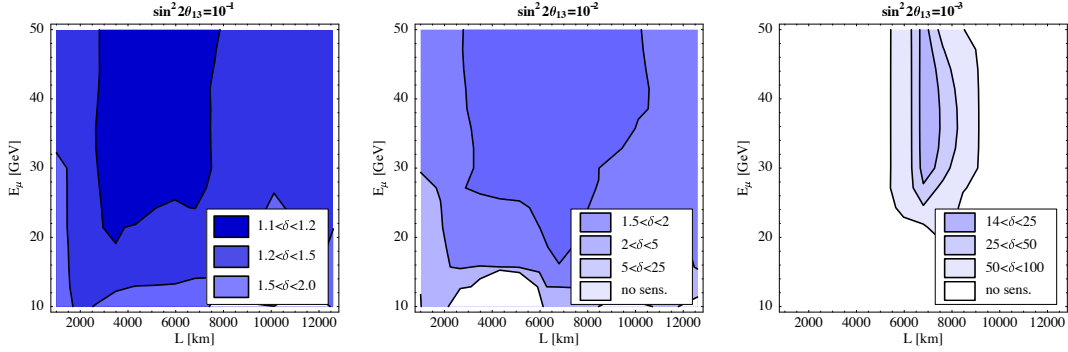

Figure 4.8: Statistical error of the quantity $\sin^2 2\theta_{13}$ as function of the baseline L and the muon energy E_μ for $\Delta m_{31}^2 = 3.5 \cdot 10^{-3} \text{eV}^2$, $\sin^2 2\theta_{23} = 1$, $N_\mu\, m_{\text{kt}} = 2 \cdot 10^{21}$ kt year and three values of $\sin^2 2\theta_{13}$ (10^{-1}, 10^{-2}, 10^{-3}) [60]. Backgrounds and experimental uncertainties are not taken into account. Dark shading indicates the preferred regions. The parameters Δm_{21}^2 and δ_{cp} play a role mainly for small values of θ_{13}. Here, they are assumed as unknown.

44
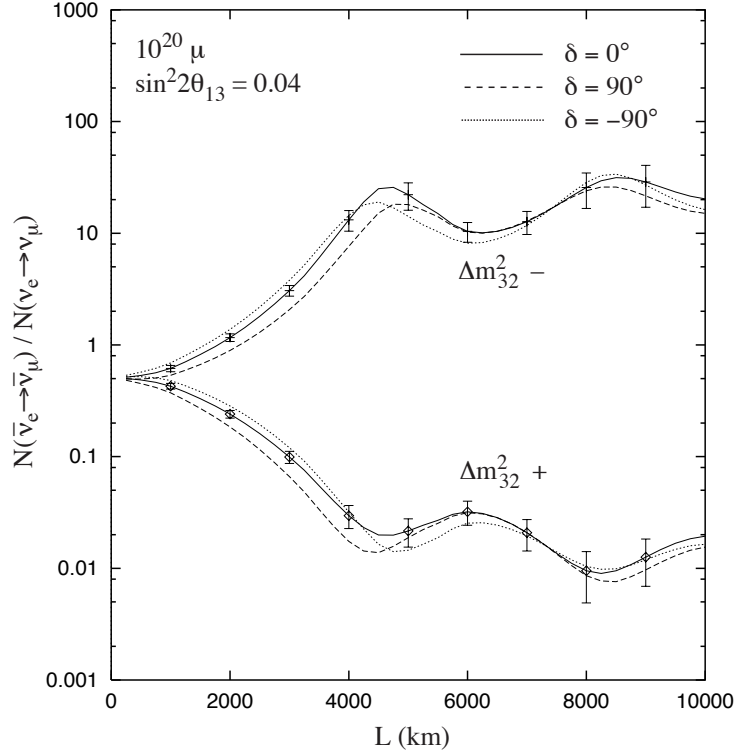
Figure 4.9: The ratio of $\bar{\nu}_e \rightarrow \bar{\nu}_\mu$ to $\nu_e \rightarrow \nu_\mu$ event rates at $E_\mu=20$GeV for $\delta = 0, \pm\pi/2$ [47]. The upper (lower) group of curves is for $\Delta m_{32}^2 < 0$ ($\Delta m_{32}^2 > 0$), and the statistical errors correspond to 10^{20} muon decays of each sign and a 50 kt detector. The oscillation parameters correspond to the LAM solar solution with $|\Delta m_{32}^2| = 3.5 \times 10^{-3}$ eV^2 and $\sin^2 2\theta_{13} = 0.04$.

been works [56, 62, 63, 64] which advocated the advantage of conventional low energy neutrino beams over neutrino factories with high energy.

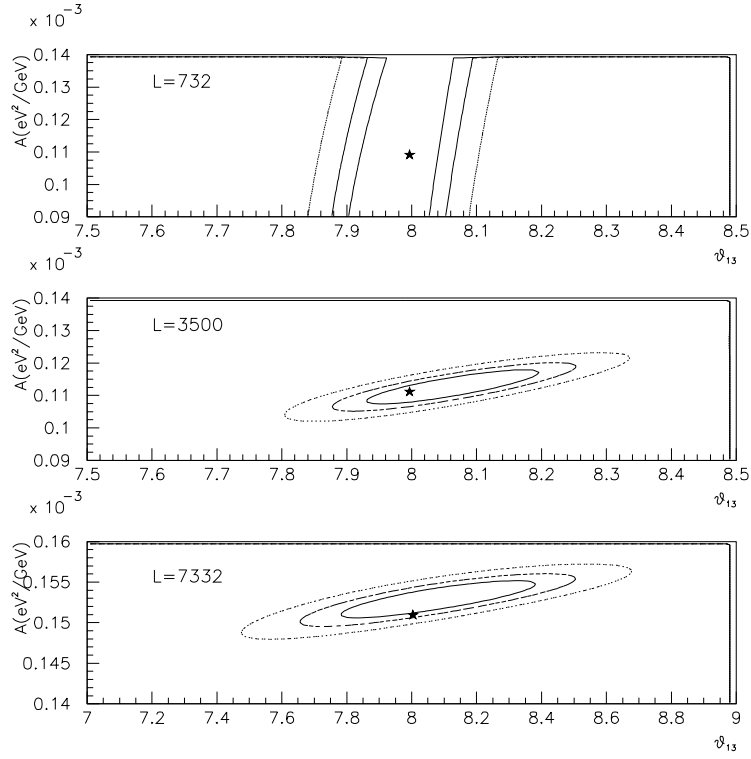Figure 4.10: 68.5, 90, 99 % CL resulting from a simultaneous fit of θ_{13} and the matter effect A for a 40 kt magnetized iron calorimeter at $L=$ 732km, 3500km, 7332 km, E_μ=50 GeV with 10^{21} useful muon decays including backgrounds and efficiencies [7]. The star indicates the parameters used to generate the "data".
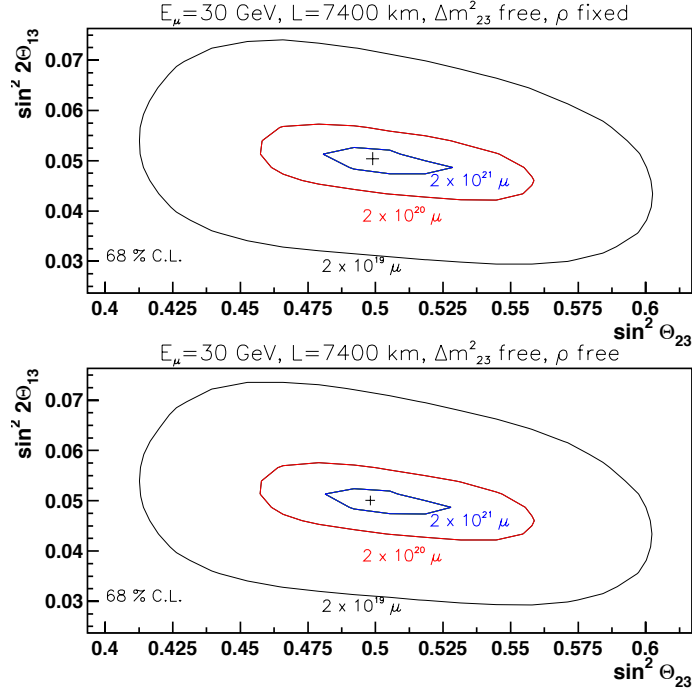
Figure 4.11: 68%C.L. two-dimensional contours for $\sin^2 2\theta_{13}$ and $\sin^2 \theta_{23}$ for a 10 kt ICANOE–type detector at $L= 7400$ km, E_μ=30 GeV with 10^{20} and 10^{21} useful muon decays [54]. Backgrounds and detection efficiencies are included. In the upper plot ρ is fixed during the fit, while in the lower one is taken as a free parameter. Influence of the density ρ in the determination of the mixing angles is not large for three different muon normalizations and for E_μ=30GeV at $L = 7400$ km.
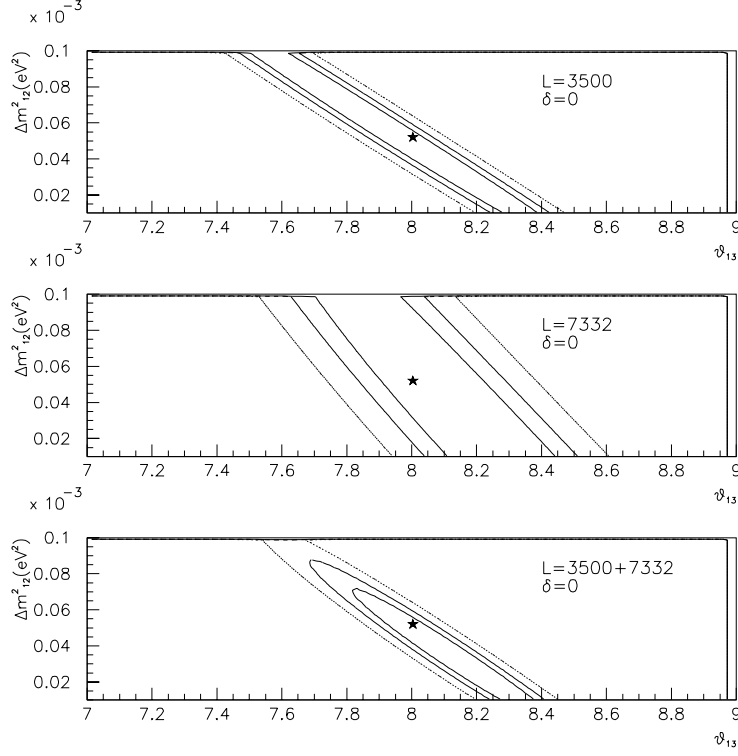
Figure 4.12: Simultaneous fit to θ_{13} and Δm_{12}^2 for a 40 kt magnetized iron calorimeter at $L=$ 3500km, 7332 km, 3500km + 7332 km, E_μ=50 GeV with 10^{21} useful muon decays [7]. The range shown in the vertical axis is the presently allowed LMA-MSW range. The star indicates the parameters used to generate the "data" and the CP-odd phase is set to zero. Backgrounds and detection efficiencies are included.
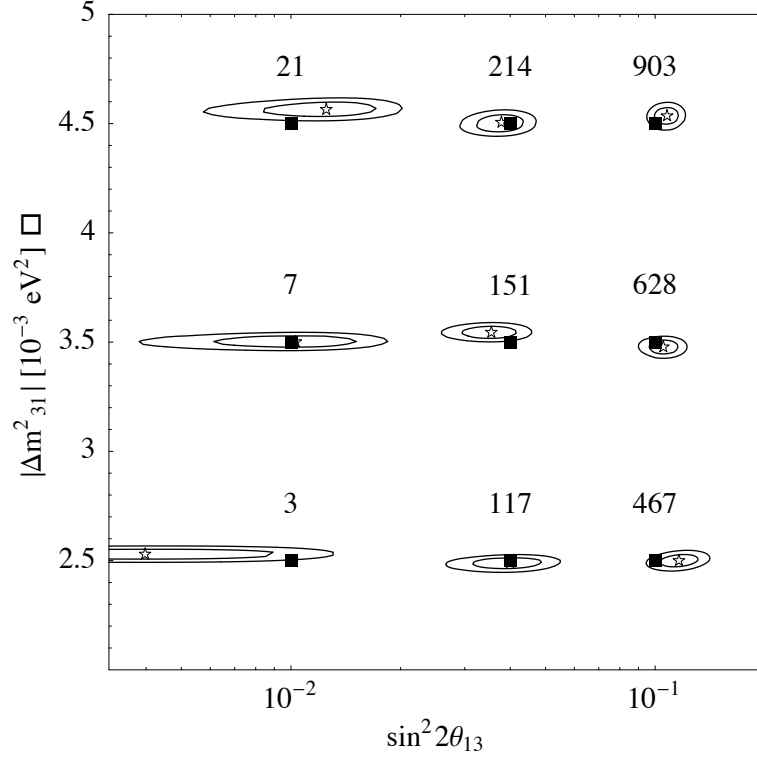
Figure 4.13: The 1σ and 2σ contours in the $(\sin^2\theta_{13}, \Delta m^2_{23})$ plane which can be achieved without charge identification (i.e., the sum of the total muons) for E_μ=30 GeV at L=7332km with 2×10^{21} useful μ^+ and μ^- decays [55]. The rectangles denote the parameter pair for which the data were generated and the stars denote the obtained best fit. The numbers printed next to each case are the values of χ^2 per 2 d.o.f for the best fit with the wrong sign of Δm^2_{31}.

49
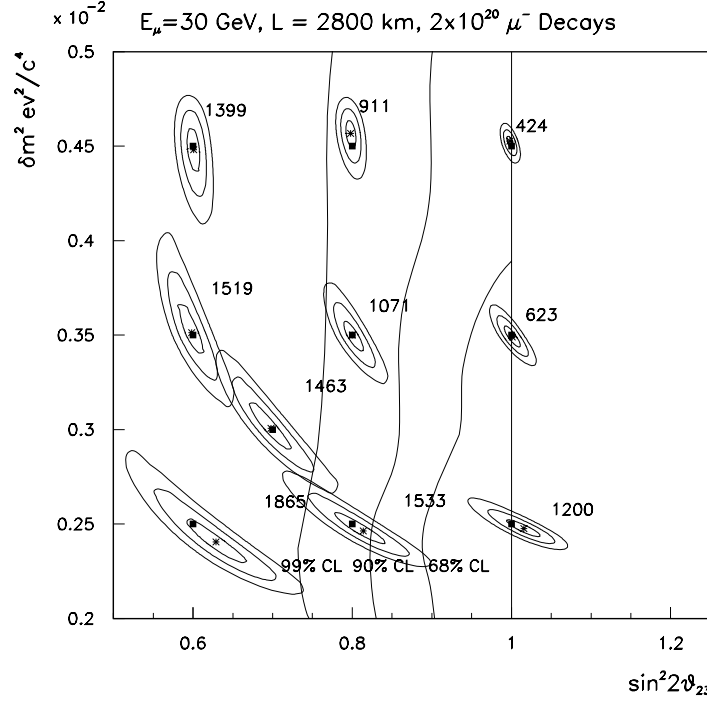
Figure 4.14: Fit results for simulated ν_μ disappearance measurements with a 10 kt MINOS-type detector 2800 km downstream of a 30 GeV neutrino factory in which there are $2 \times 10^{20} \mu^-$ decays. For each trial point the 1σ, 2σ, and 3σ contours are shown for a perfect detector (no backgrounds) and no systematic uncertainty on the beam flux. The 68%, 90% and 95% SuperK regions are indicated. Results are from Ref. [47].

Chapter 5

Pulsed Proton Beam Facility and Staging Scenario

5.1 A Pulsed Proton Beam Facility

The neutrino factory complex would require an initial proton beam to be pulsed with very narrow width. The present nuclear and particle experimental hall (NP hall) at the 50-GeV PS is planned to have only a continuous proton beam from slow extraction, and does not have any capability having a pulsed proton beam. The neutrino beam line which uses a fast-extracted proton beam can not accommodate a room for other experiments. Therefore, **we would like to strongly request the construction of a dedicated pulsed proton beam facility**. A possible location will be north from the 50-GeV PS tunnel near the pacific ocean. A preliminary layout of the pulsed proton beam facility is presented in Fig.5.1. A letter of intent on the pulsed proton beam facility is separately submitted. Here, a brief overview is presented.

Proton bunches in the 50-GeV ring are kicked off outward with respect to the 50-GeV ring toward the pulsed proton beam facility, in a single-kicking mode. It is noted that protons to the neutrino beam line are kicked inward. The presently-designed kicker magnet does already have a both-side kick since there is an abort beam line outside the 50-GeV tunnel. Our proton beam line is split from the proton abort line, and is extended to the experimental hall. Fig.5.2 shows a possible layout of such a beam line.

A layout of the facility, where the pion production target system and the first FFAG acceleration ring from 0.3 GeV/c to 1 GeV/c could be placed, is shown in Fig.5.3. The first acceleration FFAG ring could be used for another physics experiment, such as a search for the muon electric dipole moment (EDM). That ring is called PRISM-II.
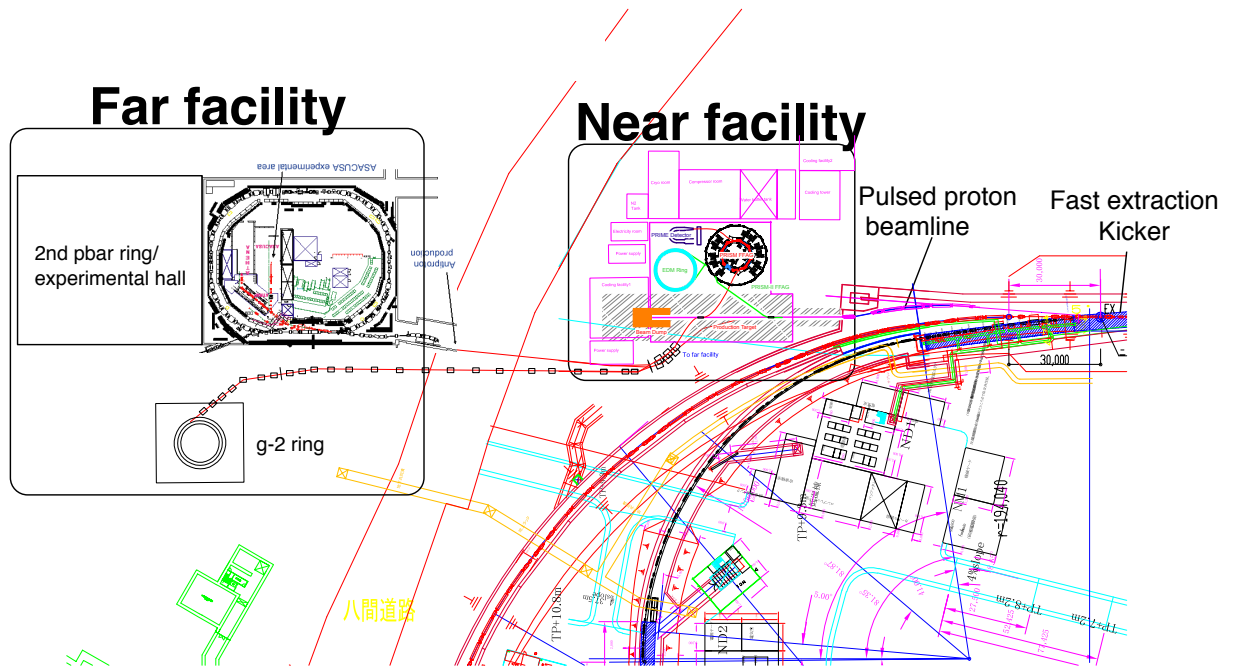
Figure 5.1: A possible layout of the pulsed proton beam facility, which consists of the near facility and the far facility.
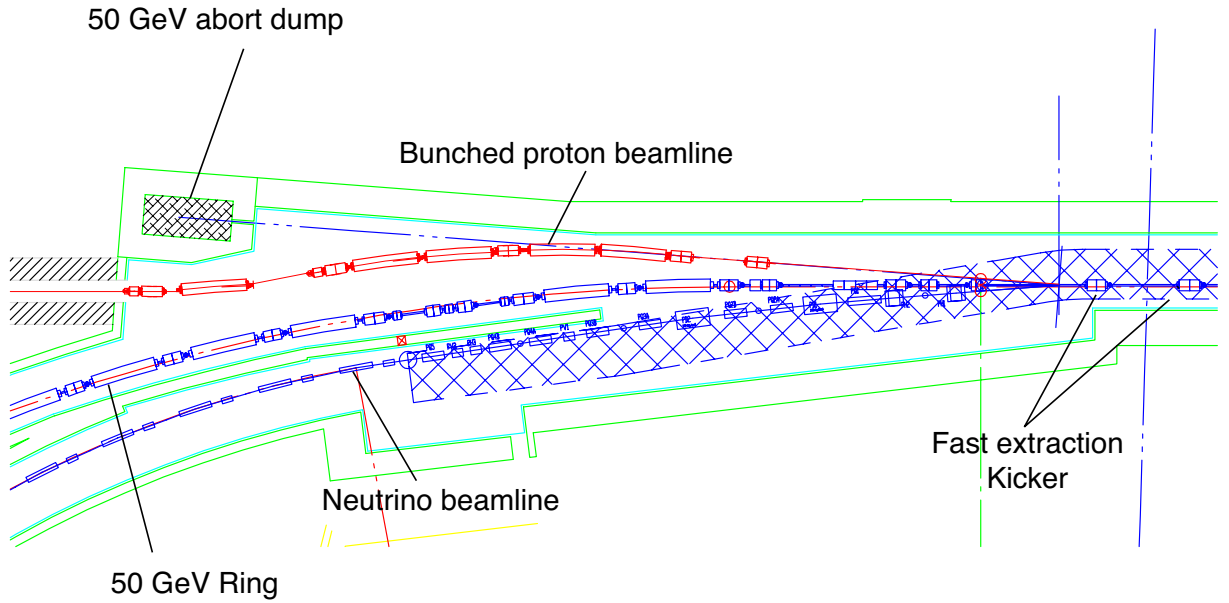
Figure 5.2: A possible layout of the pulsed (bunched) proton beam line.

5.2 Request at Phase-I

The construction of the pulsed proton beam facility is not included in the Phase-I plan of J-PARC according to the J-PARC schedule. However, it is
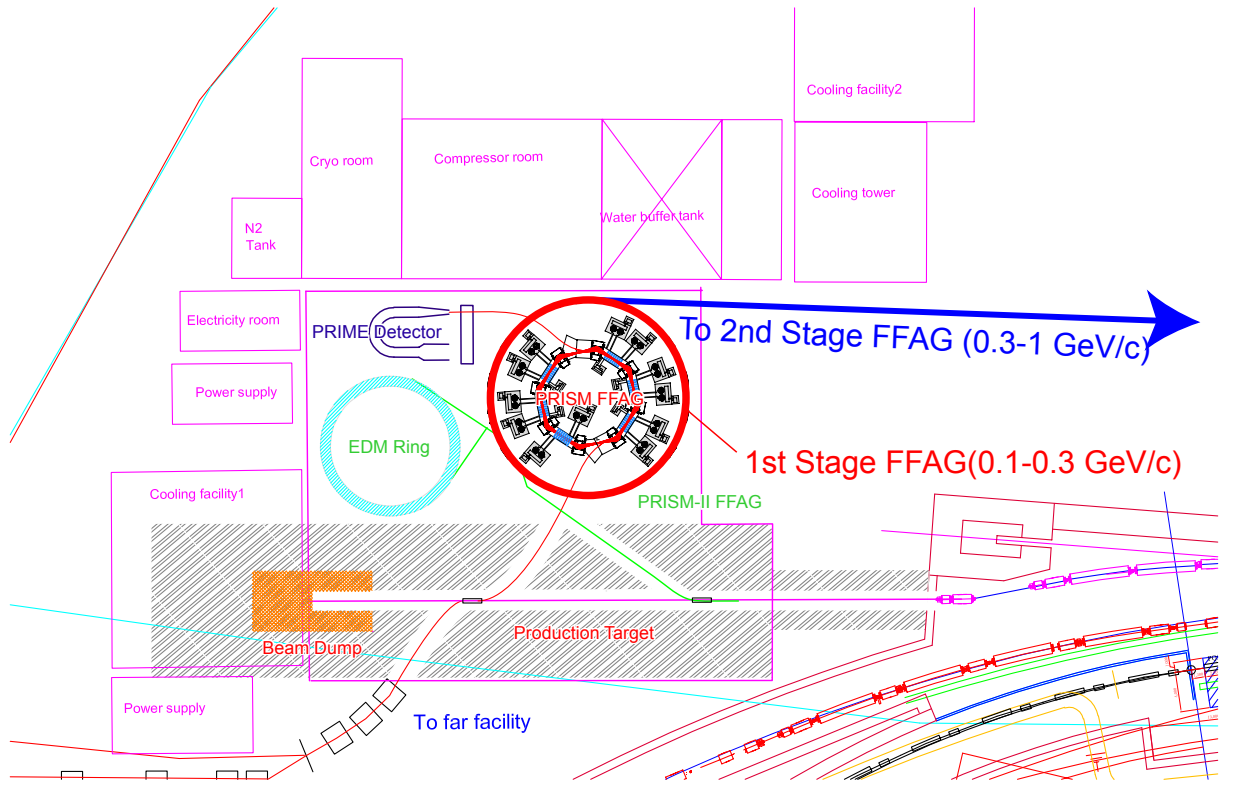
Figure 5.3: A possible layout of the near facility where PRISM and PRISM-II are installed.

important to keep its possibility at the phase-I construction. One concern is activation of soils around the area of the fast extraction port from the 50-GeV protons in the ring. If soils at that area are activated, future excavation for the tunnel of the proton beam line would become severely difficult. To avoid activation, we like to place some concrete shielding blocks at the location of proton extraction. Possible arrangement which we are considering is shown in Fig.5.4.

The thickness of the shielding blocks required was calculated based on the Moyer formula which assumes a linear radiation loss. From the calculation, with a concrete shielding of 2.2 meter thick in addition to the 0.8 meter thick of the 50-GeV tunnel wall, soil activation would be about 0.07 msv/h and 0.02 Bq/g. It is much less than the acceptable level of 0.3 msv/h and 0.1 Bq/g. From this, it is shown that the concrete shielding blocks of 2.2 meter thickness would be sufficient.

5.3 Staging Approach based on FFAG Acceleration

A staging approach should be seriously considered to construct a large scaled project like a neutrino factory. This staging approach is demanded in two folds. One is to maintain a total budget profile to be a reasonable size at different stages to get the funding easier. The second is that establishing required technology will require a long term, whereas we like to keep physics activities even in the R&D period. In our FFAG acceleration scheme, it is possible since we start with the first acceleration ring, and add downstream FFAG rings at a later time.

In fact, the first ring is located at the proposed pulsed proton beam facility[1]. The second, third and forth rings would be in the area surrounded by the 50-GeV PS tunnel. They should be located deep underground. It should be noted that the second ring is the one that we call PRISM-II, which would be used for a search for the muon electric dipole moment (EDM).

Possible connection to physics programs is listed in Table 5.1.

Table 5.1: Possible scenario of the staging based on FFAG acceleration.

Stage	FFAG ring	Potential Physics Programs
0	Low energy (PRISM)	muon LFV
1	0.3-1 GeV/c (PRISM-II)	muon EDM and low-energy neutrino source
2	1-3 GeV/c	1 GeV neutrino source
3	3-10 GeV/c	an initial neutrino factory
4	10-20 GeV/c	a full size neutrino factory

In particular, at a very early stage, we consider to have a very small FFAG ring for stopped muon experiments, where searches for muon lepton flavor violation can be carried out. It is noted that the search for muon lepton flavor violation has attracted much interest as good testing ground of supersymmetric grand unification [20]. The project is called PRISM[2]. PRISM would have many common technical challenges with R&D for neutrino factories. They are such as a large-solid angle pion capture with high-field solenoid magnet, phase rotation, high-gradient rf cavity, and a FFAG ring itself.

---

[1] Please refer to a separate Letter of Intent on the pulsed proton beam facility.
[2] A separate Leter of Intent on PRISM is available.
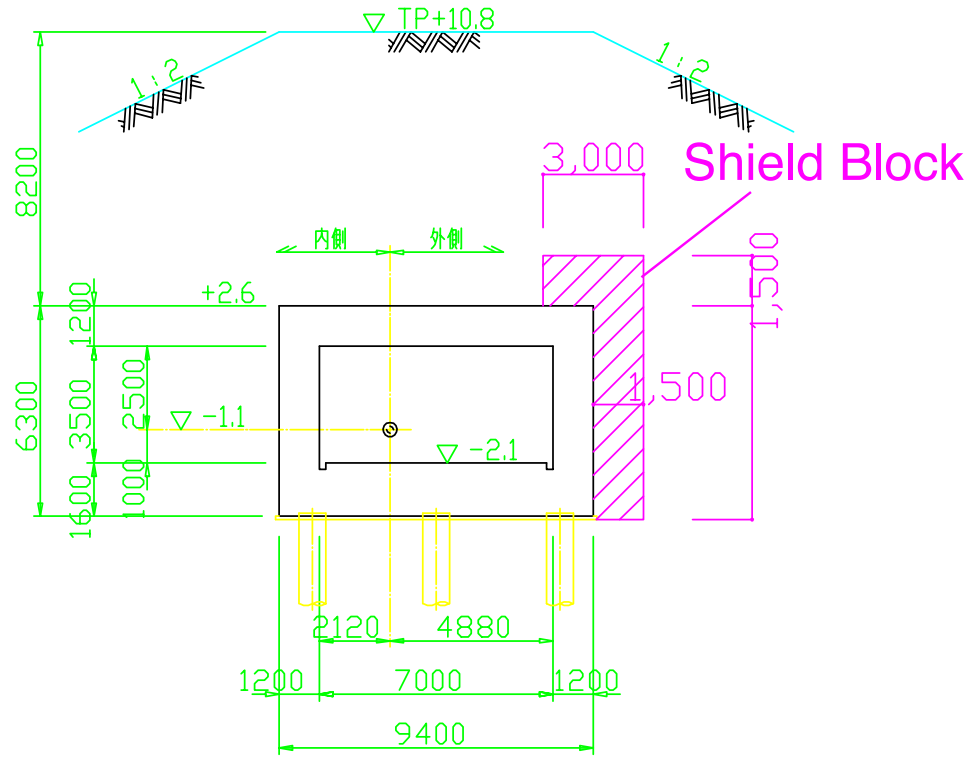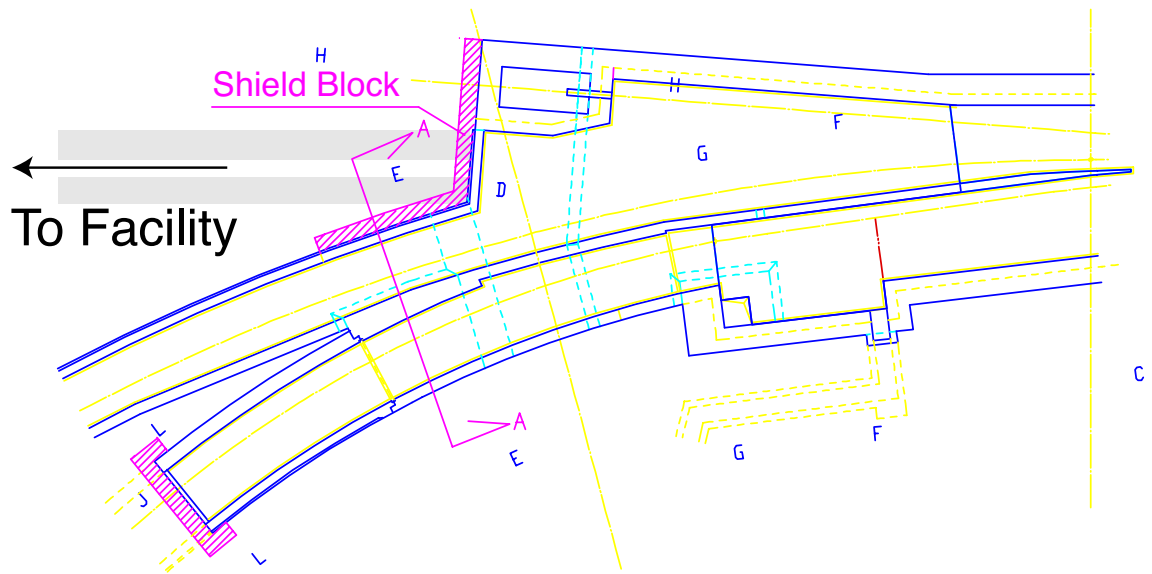
Figure 5.4: Possible arrangement to avoid soil activation around the location of proton extraction.

Chapter 6

Conclusion

Our preliminary study on a neutrino factory in Japan, at the location of J-PARC, has been presented. The Japanese scheme of a neutrino factory is based on muon accelerator by a series of FFAG rings. We have shown the physics cases of a neutrino factory, the preliminary design of the accelerator complex, and a possible layout at J-PARC. To aim at the realization, we have shown our staging approach, in which we would start with a low energy muon FFAG ring (PRISM) for the search for lepton flavor violating $\mu^- - e^-$ conversion, and then a 500-MeV/c muon FFAG ring (PRISM-II) for the search for the muon electric dipole moment (EDM). For each stage, significant physics outcomes can be anticipated with large discovery potentials. In particular, the PRISM-II ring is identical to the first muon acceleration ring in a neutrino factory in our scheme. To realize these staging approach, it would be very important to construct a proposed pulsed proton beam facility where the pion collection, and the first accelerator ring for the neutrino factory would be placed.

Acknowledgment

Bibliography

[1] Z. Maki, M. Nakagawa, and S. Sakata, Prog. Theor. Physics **28** (1962) 870.

[2] FNAL report "A Feasibility Study of a neurtino Source Based on a Muon Storage Ring" edited by N. holtkamp and D. Finley : "Physics at a Neutrino Factory", FERMILAB-FN-692, April, 2000.

[3] CERN report 99-02 and ECFA 99-197, "Prospective Study of muon Storage Rings at CERN", edited by B. Autin, A. Blondel and J. Ellis.

[4] V. Barger, S. Geer, R. Raja, and K. Whisnant, hep-ph/0012017.

[5] V. Barger, S. Geer and K. Whisnant, Phys. Rev. **D61** (2000) 053004.

[6] P.F.Harrison and W.G. Scott, Phys. Lett. B **476** (2000) 349 : H.Yokomakura, K.Kimura and A. Takamura, Phys. Lett. B **496** (2000) 175 : S.J. Park, T. Weiler, hep-oh/0011247

[7] A. . Cervera , A. Donini, M.B. Gavela, J.J. Gomez Cadenas, P. Hernandez, O. Mena and S. Rigolin, hep-ph/0002108.

[8] JAERI/KEK Joint Project Proposal, 1999, unpublished.

[9] Y. Kuno *et al.*, in Proceedings of Workshop on "High Intensity Muon Sources", December, 1999, World Scientific.

[10] R.Palmer, C.Johnson, E.Keil: CERN-SL-99-070-AP, 1999.

[11] C.Ohkawa: Bulletin of Physical Society of Japan, 1953.

[12] K.R.Symon et al.: Phys. Rev., 103,(1956)1837.

[13] Y. Mori and FFAG group at KEK: Proc. European Particle Accelerator Conference, 2000, Vienna, Austria, pp581.

[14] JHF Project Office: "Proposal of High Intensity Proton Accelerators",2000.

[15] H. Shonauer, Workshop on FFAG accelerator, FFAG00, KEK,2000

[16] W.D.Kilpatrick, et al., "Criterion for Vacuum Sparking Designed to Include Both rf and dc", The Review of Scientific Instruments, Vol. 28, No.10, 824-826, 1957

[17] K. W. Shepard and W.C. Sellyey: "A Low-Frequency RFQ for a Low-Charge-State Injector for ATLAS", Proc. of the 18th International Linac Conf. 26-30 Aug. 1996, Geneva, Switzerland, pp.68-70

[18] J. Boucheron, R. Garoby, D. Grier, M. Paoluzzi, F. Pedersen: "A 1 MV 9.5MHz RF System for the CERN Antiproton Collector", Proc of the European Particle Accelerator Conference", 11-16 June, 1990, Nice, France, pp.958-960

[19] Y. Mori et al., Proceedings of EPAC, 1998, p.299-301

[20] Y. Kuno and Y. Okada, Review of Modern Physics, **73** (2001) 151.

[21] B.T. Cleveland et al., Nucl. Phys. B (Proc. Suppl.) **38**, 47 (1995).

[22] K.S. Hirata et al., Phys. Rev. Lett. **63**, 16 (1989); *ibid.* **65**, 1297 (1990); *ibid.* **65**, 1301 (1990); *ibid.* **66**, 9 (1991); Phys. Rev. **D44**, 2241 (1991); Y. Fukuda et al., Phys. Rev. Lett. **77**, 1683 (1996).

[23] Y. Fukuda et al., Phys. Rev. Lett. **81**, 1158 (1999); *ibid.* **82**, 1810 (1999); *ibid.* **82**, 2430 (1999).

[24] VA. I. Abazov et al., Phys. Rev. Lett. **67**, 3332 (1991); J. N. Abdurashitov et al., Nucl. Phys. B (Proc. Suppl.) **38**, 60 (1995); Nucl. Phys. B (Proc. Suppl.) **77**, 20 (1999).

[25] P. Anselmann et al., Phys. Lett. **B285**, 376 (1992); *ibid.* **B314**, 445 (1993); *ibid.* **327**, 377 (1994); *ibid.* **B342**, 440 (1995); *ibid.* **B357**, 237 (1995); *ibid.* **B388**, 384 (1996); Nucl. Phys. B (Proc. Suppl.) **77**, 26 (1999).

[26] M. Altmann et al., Phys. Lett. **B490**, 16 (2000).

[27] K.S. Hirata et al., Phys. Lett. **B205**, 416 (1988); Phys. Lett. **B280**, 146 (1992); Y. Fukuda et al., Phys. Lett. **B335**, 237 (1994); S. Hatakeyama et al., Phys. Rev. Lett. **81**, 2016 (1998).

[28] D. Casper et al., Phys. Rev. Lett. **66**, 2561 (1989); R. Becker-Szendy et al., Phys. Rev. **D46**, 3720 (1992).

[29] Y. Fukuda et al., Phys. Lett. **B433**, 9 (1998); Phys. Lett. **B436**, 33 (1998); Phys. Rev. Lett. **81**, 1562 (1998); Phys. Rev. Lett. **82**, 2644 (1999); Phys. Rev. Lett. **82**, 5194 (1999); Phys. Lett. **B467**, 185 (1999); Phys. Rev. Lett. **85**, 3999 (2000); C. McGrew, talk at *The 2nd Workshop on "Neutrino Oscillations and Their Origin"*, December 6-8, 2000,

University of Tokyo, Tokyo, Japan
(http://www-sk.icrr.u-tokyo.ac.jp/noon/2/transparency/1207/08/index.html).

[30] W.W.M. Allison et al., Phys. Lett. **B391**, 491 (1997); Phys. Lett. **B449**, 137 (1999).

[31] F. Ronga, Nucl. Phys. B (Proc. Suppl.) **77**, 117 (1999).

[32] C. Athanassopoulos *et al.*, (LSND Collaboration), Phys. Rev. Lett. **77**, 3082 (1996); Phys. Rev. C **54**, 2685 (1996); Phys. Rev. Lett. **81**, 1774 (1998); Phys. Rev. C **58**, 2489 (1998); D.H. White, Nucl. Phys. Proc. Suppl.**77** 207 (1999); G. Mills, talk at *19th International Conference on Neutrino Physics and Astrophysics* (Neutrino 2000), Sudbury, Canada, June 16-22, 2000
(http://nu2000.sno.laurentian.ca/G.Mills/).

[33] B. M. Pontecorvo, Sov. Phys. JETP **34**, 247 (1958).

[34] Z. Maki, M. Nakagawa and S. Sakata, Prog. Theor. Phys. **28**, 870 (1962).

[35] Y. Suzuki, talk at *19th International Conference on Neutrino Physics and Astrophysics* (Neutrino 2000), Sudbury, Canada, June 16-22, 2000
(http://nu2000.sno.laurentian.ca/ Y.Suzuki/).

[36] O. Yasuda, Acta Phys. Pol. **B30**, 3089 (1999).

[37] M.C. Gonzalez-Garcia, M. Maltoni, C. Pena-Garay, J.W.F. Valle, Phys. Rev. **D63**,033005 (2001).

[38] G.L. Fogli, E. Lisi, A. Marrone, D. Montanino and A. Palazzo, hep-ph/0104221.

[39] M. Apollonio *et al.*, Phys. Lett. B **338**, 383 (1998); Phys. Lett. B **466**, 415 (1999).

[40] G.L. Fogli, E. Lisi, A. Marrone and D. Montanino, hep-ph/0009269; M.C. Gonzalez-Garcia, M. Maltoni, C. Pena-Garay and J.W.F. Valle, Phys. Rev. **D63**, 033005 (2001).

[41] M.C. Gonzalez-Garcia and C. Pena-Garay, hep-ph/0009041.

[42] G.L. Fogli, E. Lisi, D. Montanino, and A. Palazzo, Phys. Rev. **D62** (2000) 113003; G.L. Fogli, E. Lisi, A. Marrone, D. Montanino, and A. Palazzo, Phys. Rev. **D66** (2002) 053010.

[43] A.Yu. Smirnov, talk at Europhysics Neutrino Oscillation Workshop (NOW2000), Conca Specchiulla (Otranto, Italy), September 9-16, 2000
(http://www.ba.infn.it/ now2000/views/slides/Smirnov/) and private communication.

[44] J.G. Learned, hep-ex/0007056.

[45] The Super-Kamiokande collaboration, Phys. Rev. Lett. **86**(2002) 5651; Phys. Rev. Lett. **86**(2002) 5656.

[46] B. Autin et al., CERN-SPSC-98-30; Neutrino Factory and Muon Collider Collaboration (D. Ayres *et al.*), physics /9911009; C. Albright *et al.*, hep-ex/0008064.

[47] V. Barger, S. Geer, R. Raja and K. Whisnant, Phys. Rev. **D62**, 013004 (2000); Phys. Lett. **B485** (2000) 379; hep-ph/0007181.

[48] V. Barger, S. Geer, R. Raja and K. Whisnant, Phys. Rev. **D62**, 073002 (2000);

[49] A. De Rujula, M. B. Gavela and P. Hernandez, Nucl. Phys. **B547**, 21 (1999).

[50] A. Donini, M. B. Gavela, P. Hernandez and S. Rigolin, Nucl. Phys. **B574**, 23 (2000).

[51] A. Romanino, Nucl. Phys. **B574**, 675 (2000).

[52] K. Dick, M. Freund, M. Lindner, and A. Romanino, Nucl. Phys. **B562**, 29 (1999).

[53] M. Freund, M. Lindner, S.T. Petcov and A. Romanino, Nucl. Phys. **B578**, 27 (2000).

[54] M. Campanelli, A. Bueno and A. Rubbia, hep-ph/9905240; A. Bueno, M. Campanelli and A. Rubbia, Nucl. Phys. **B573**, 27 (2000); Nucl. Phys. **B589**, 577 (2000).

[55] M. Freund, P. Huber and M. Lindner, Nucl. Phys. **B585**, 105 (2000).

[56] J. Sato, Nucl. Instrum. Meth. **A451**, 36 (2000); hep-ph/0006127, hep-ph/0008056; M. Koike and J.Sato, Phys. Rev. **D61**, 073012 (2000); talk at International Workshop on Muon Storage Ring for a Neutrino Factory (NUFACT'00), Monterey, California, 22 – 26 May 2000; talk at the Joint U.S./Japan Workshop On New Initiatives In Muon Lepton Flavor Violation and Neutrino Oscillation With High Intense Muon and Neutrino Sources, Honolulu, Hawaii, Oct. 2–6, 2000; talk at JSPS-KOSEF Joint Workshop on "New Developments in Neutrino Physics", Korea Institute for Advanced Study, Seoul, Korea, 16 - 20 October 2000; T. Ohta and J. Sato, Phys. Rev. **D63**, 093004 (2001); M. Koike, T. Ohta and J. Sato, hep-ph/0011387.

[57] O. Yasuda, talk at KEK International Workshop On High Intensity Muon Sources (HIMUS 99), Tsukuba, Japan, 1 – 4 December 1999, hep-ph/0005134.

[58] T. Miura, E. Takasugi, Y. Kuno, M. Yoshimura, hep-ph/0102111.

[59] J. Burguet-Castell, M.B. Gavela, J.J. Gomez-Cadenas, P. Hernandez, O. Mena, hep-ph/0103258.

[60] M. Freund, P. Huber and M. Lindner, hep-ph/0105071.

[61] J. Pinney and O. Yasuda, hep-ph/0105087

[62] A. Konaka, talk at the 1st Tokutei-RCCN Workshop on Neutrinos, ICRR, Univ. of Tokyo, Kashiwa, Japan, May 12, 2000.

[63] H. Minakata and H. Nunokawa, Phys. Lett. **B495**, 369 (2000).

[64] B. Richter, hep-ph/0008222.

[65] M. Nakahata et. al., J. Phys. Soc. Japan, **55**, 3786 (1986).

[66] P. Lipari, M. Lusignoli and F. Sartogo, Phys. Rev. Lett. **74**, 4384 (1995).

[67] K. Nakamura, talk at the Joint U.S./Japan Workshop On New Initiatives In Muon Lepton Flavor Violation and Neutrino Oscillation With High Intense Muon and Neutrino Sources, Honolulu, Hawaii, Oct. 2–6, 2000,
http://meco.ps.uci.edu/lepton_workshop/talks/nakamura.pdf.

[68] D. Casper, talk at Joint U.S. / Japan Workshop on New Initiatives in Lepton Flavor Violation and Neutrino Oscillation with High Intense Muon and Neutrino Sources, Honolulu, Hawaii, 2-6 Oct 2000,
http://meco.ps.uci.edu/lepton_workshop/talks/casper/uno.pdf.

[69] F. Stacey, *Physics of the Earth, 2nd ed.* (J. Wiley and Sons, Chichester, 1977).

[70] V. Barger, S. Geer, R. Raja and K. Whisnant, hep-ph/0012017.

[71] Y. Itow et al., Letter of Intent,
http://www-jhf.kek.jp/JHF_WWW/LOI/jhfnu_loi.ps.

[72] Y. Obayashi, talk at the Joint U.S./Japan Workshop On New Initiatives In Muon Lepton Flavor Violation and Neutrino Oscillation With High Intense Muon and Neutrino Sources, Honolulu, Hawaii, Oct. 2–6, 2000,
http://meco.ps.uci.edu/lepton_workshop/talks/obayashi.pdf.

[73] T. Kobayashi, talk at the 5th Tokutei-RCCN Workshop on Neutrinos, ICRR, Univ. of Tokyo, Kashiwa, Japan, Feb. 23–24, 2001.

[74] M. Maris and S.T. Petcov, Phys. Rev. **D56**, 7444 (1997).

[75] D.L. Anderson, private communication.

[76] T. Tanimoto, private communication.

[77] T. Tanimoto, J. Phys. Earth **38**, 493 (1990).

[78] J. Resovsky, private communication.

[79] R. Geller, private communication.

[80] J. Sato, Nucl. Instrum. Meth. **A451**, 36 (2000), hep-ph/0006127, hep-ph/0008056; A. Konaka, unpublished; B. Richter, hep-ph/0008222; H. Minakata and H. Nunokawa, Phys. Lett. **B495**, 369 (2000); V. Barger, S. Geer, R. Raja and K. Whisnant, hep-ph/0012017.

[81] Y. Ohbayashi, talk at Workshop on New Initiatives in Muon Lepton Flavor Violation and Neutrino Oscillation with High Intense Muon and Neutrino Sources, Honolulu, Hawaii, 2-6 Oct 2000. http://meco.ps.uci.edu/lepton_workshop/talks/obayashi.pdf

[82] M. Koike, T. Ota and J.Sato, hep-ph/0011387.

Appendix A

Bunch structure of the Proton Beam in the 50-GeV PS

In the linac-based neutrino factory, phase rotation in longitudinal phase space to decrease the momentum spread of the muon beams becomes essential. Thus, the bunch length of the beam from the proton driver should be rather short in the linac based neutrino factory. The required bunch length in this case is about 3 ns or less in rms size.

On the other hand, in the FFAG based scenario, the requirement of the bunch length is much more modest compared with this because the longitudinal acceptance of the FFAG using a low frequency rf system is relatively large. The expected bunch width from the proton beam is 6 ns or more in rms size. In fact, the rf frequency at 50 GeV is about 2 MHz and the bunching factor at 50 GeV becomes about 0.038. Thus, the rms bunch length at 50 GeV is approximately 6 ns in ordinary operation, which is exactly the same as required in the FFAG based neutrino factory. This means that no special treatment to the bunch shortening is necessary for the 50GeV proton driver in our FFAG based neutrino factory.

If we need in future a bunch shortening for some reasons, we may take the several schemes for this purpose as described below.

1. Multi harmonic number
   The peak beam current at 50 GeV reaches almost 200 A, This is not an easy value to compensate for its beam loading effects on the rf system. It is preferable not to exceed the peak beam current from 200 A, which means that the bunching factor should be around 0.038 even when we shorten the bunch width to a half of the ordinary one. To shorten a bunch width of less than 6 ns in a rms size, while keeping the same bunching factor, we increase the harmonic number to a higher one at the top energy of the 50-GeV ring. It is rather hard to change all of the harmonic numbers from the 3-GeV booster to 50-GeV main ring. In order to realize this, another harmonic rf system at the top energy of the 50 GeV ring should be introduced, and bunch manipulation with de- bunching and re-bunching could be applied.

Broadband rf cavities with soft magnetic alloy (MA cavity) are used for acceleration in the 50 GeV ring. The Q-value of this type of cavity can be rather low and controllable by cutting cores. In case of the 50 GeV ring, any Q values between 1 and 10 can be set by varying the core spacing. The second harmonic rf cavities using the same material are installed in the 50 GeV ring for increasing the bunching factor at beam injection to reduce the transverse space charge effect. These rf cavities may also be used for the bunch shortening. The main items to be examined from the beam dynamics view in this scheme are microwave instability during the debunching and coupled bunch instability after rebunching. As for the microwave instability, the stability condition would be the same as that of the ordinary operation, which is Z/n $< 2\Omega$, because the bunching factor and $\Delta p/p$ is the same. Low Q cavities are used in the rf acceleration of the 50 GeV ring. Provided the low Q cavities are also utilized for doubling the harmonic number, the coupled-bunch instability can be avoided.

2. Other scheme

There are a couple of other methods to achieve a short bunch as shown in ref.[2]: (1) rf amplitude jump, (2) rf phase jump, and (3) Γt manipulation. Method (1) is a common one, however, very high gradient and low frequency rf cavities are necessary and transient beam loading effect has to be cured carefully. Methods (2) and (3) has been preliminarily tried at the HIMAC synchrotron[3] and the KEK 12-GeV PS[4], respectively. It seems to work at the intensity level of 10^{12} ppp for the method (3), however, further intensive studies including simulations and experiments should be done.

Appendix B

FFAG Muon Ionization Cooling

In the FFAG based neutrino factory, muon cooling is not mandatory, because of large beam acceptance of the FFAG accelerators. Nevertheless, it would be helpful to reduce the technical difficulties of making superconducting magnets with large aperture for the high energy rings and the storage ring, and also the initial investment cost for them if the muon cooling works effectively, in particular, at low energy.

The potential of transverse ionization cooling in the FFAG ring scenario has been examined by Shonauer.[15] Transverse ionization cooling process is expressed by the following differential equation. [2]

$$\frac{d\epsilon_n}{\epsilon_n ds} = -\frac{1}{\beta^2 E}\frac{dE}{ds} + \frac{(13.6 MeV)^2}{2\beta^3 m_\mu c^2 L_R}\frac{\beta_T}{E\epsilon_n} \tag{B.1}$$

Here, L_R is the radiation length of the absorber material and β_T the average transverse beta function at absorber, respectively. In his study of the transverse ionization cooling in the FFAG ring, a absorber with pressurized gas filling the beam pipe is distributed in the ring. The effect of the main parameters, such as transverse beta functions and rf accelerating field gradient, on cooling and transmission can be examined by solving the above equation. The cooling effect depends strongly on the transverse beta function values. The heating caused by multiple scattering becomes dominant at lower energy for larger beta function values and the emittance blows up. According to Shonauer, when the H_2 gas of 25 bar is filled into the 0.3-1 GeV/c FFAG ring where the average beta function value is 2 meters, the cooling factor becomes 0.57 and the transmission is 83% of its no- cooling value as shown in Fig. B.1. He is also claiming that, in order to gain additional cooling, it is preferable to insert cooling sections or rings between the FFAG's at energies between 1 and 3 GeV/c.
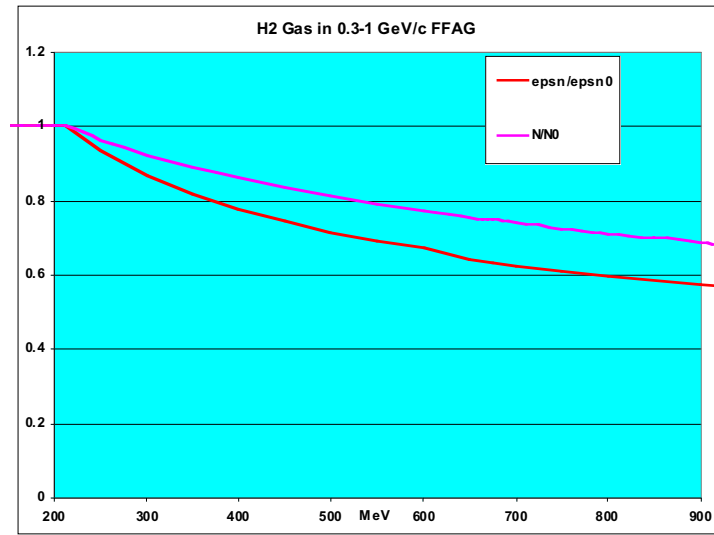
Figure B.1: Cooling factor and transmission as function of muon energy for 0.3-1 GeV/c FFAG ring. The H2 gas pressure is 25 bar

.

Appendix C

The Measurement of δ

C.1 Definition of $\Delta\chi^2$

One of the purposes of this section is to show that neutrino factories with high or medium muon energy (20 GeV $\lesssim E_\mu \lesssim$ 50 GeV) are more advantageous over experiments with low energy ($E_\mu \ll$ 10 GeV). In the present report we use the result of [61] in which correlations of errors of δ and all the oscillations parameters as well as the matter effect have been taken into account and the data size to reject a hypothesis $\delta = 0$ has been obtained. The statistical significance of possible CP violation in neutrino factory type experiments is evaluated for a range of the muon energy 0.5GeV$\leq E_\mu \leq$50 GeV and the baseline 10 km $\leq L \leq 10^4$km and it is shown that the case $E_\mu \lesssim$ a few GeV is always inferior to the option with higher energy. It is also shown analytically that the two kinds of $\Delta\chi^2$ which will be used, one of which is defined through the difference of $\delta \neq 0$ and $\delta = 0$ and the other of which through T violation, decrease for large muon energy $E_\mu \gg$50 GeV.

Our strategy here is to examine whether a hypothesis with a vanishing CP phase is rejected or not by taking into consideration all channels $\nu_e \to \nu_\mu$, $\bar{\nu}_e \to \bar{\nu}_\mu$, $\nu_\mu \to \nu_\mu$ and $\bar{\nu}_\mu \to \bar{\nu}_\mu$. For this purpose we define $\Delta\chi^2$ to test a hypothesis that a CP phase is given by $\bar{\delta}$ in the case where the true value is δ:

$$
\begin{aligned}
&\Delta\chi^2(\theta_{k\ell}, \Delta m_{k\ell}^2, \delta, C; \bar{\theta}_{k\ell}, \overline{\Delta m_{k\ell}^2}, \bar{\delta}, \bar{C}) \\
&\equiv \sum_j \frac{\left[N_j^{\text{wrong}}(\mu^-; \theta_{k\ell}, \Delta m_{k\ell}^2, \delta, C) - N_j^{\text{wrong}}(\mu^-; \bar{\theta}_{k\ell}, \overline{\Delta m_{k\ell}^2}, \bar{\delta}, \bar{C})\right]^2}{N_j^{\text{wrong}}(\mu^-; \theta_{k\ell}, \Delta m_{k\ell}^2, \delta, C)} \\
&+ \sum_j \frac{\left[N_j^{\text{wrong}}(\mu^+; \theta_{k\ell}, \Delta m_{k\ell}^2, \delta, C) - N_j^{\text{wrong}}(\mu^+; \bar{\theta}_{k\ell}, \overline{\Delta m_{k\ell}^2}, \bar{\delta}, \bar{C})\right]^2}{N_j^{\text{wrong}}(\mu^+; \theta_{k\ell}, \Delta m_{k\ell}^2, \delta, C)}
\end{aligned}
$$

---

[1]This work is done by Dr. Osamu Yasuda.

$$+ \sum_j \frac{\left[N_j^{\text{right}}(\mu^-; \theta_{k\ell}, \Delta m_{k\ell}^2, \delta, C) - N_j^{\text{right}}(\mu^-; \bar{\theta}_{k\ell}, \overline{\Delta m_{k\ell}^2}, \bar{\delta}, \bar{C})\right]^2}{N_j^{\text{right}}(\mu^-; \theta_{k\ell}, \Delta m_{k\ell}^2, \delta, C)}$$

$$+ \sum_j \frac{\left[N_j^{\text{right}}(\mu^+; \theta_{k\ell}, \Delta m_{k\ell}^2, \delta, C) - N_j^{\text{right}}(\mu^+; \bar{\theta}_{k\ell}, \overline{\Delta m_{k\ell}^2}, \bar{\delta}, \bar{C})\right]^2}{N_j^{\text{right}}(\mu^+; \theta_{k\ell}, \Delta m_{k\ell}^2, \delta, C)} \tag{C.1}$$

where j runs over energy bins and the numbers of events are given by

$$N_j^{\text{wrong}}(\mu^-; \theta_{k\ell}, \Delta m_{k\ell}^2, \delta, C)$$
$$= \frac{12 N_0 E_\mu}{\pi L^2 m_\mu^2} \int_{E_j}^{E_{j+1}} dE_\nu \left(\frac{E_\nu}{E_\mu}\right)^2 \left(1 - \frac{E_\nu}{E_\mu}\right) \sigma_{\nu N}(E_\nu) P(\nu_e \to \nu_\mu; \theta_{k\ell}, \Delta m_{k\ell}^2, \delta, C)$$

$$N_j^{\text{wrong}}(\mu^+; \theta_{k\ell}, \Delta m_{k\ell}^2, \delta, C)$$
$$= \frac{12 N_0 E_\mu}{\pi L^2 m_\mu^2} \int_{E_j}^{E_{j+1}} dE_{\bar{\nu}} \left(\frac{E_{\bar{\nu}}}{E_\mu}\right)^2 \left(1 - \frac{E_{\bar{\nu}}}{E_\mu}\right) \sigma_{\bar{\nu} N}(E_{\bar{\nu}}) P(\bar{\nu}_e \to \bar{\nu}_\mu; \theta_{k\ell}, \Delta m_{k\ell}^2, \delta, C)$$

$$N_j^{\text{right}}(\mu^-; \theta_{k\ell}, \Delta m_{k\ell}^2, \delta, C)$$
$$= \frac{2 N_0 E_\mu}{\pi L^2 m_\mu^2} \int_{E_j}^{E_{j+1}} dE_\nu \left(\frac{E_\nu}{E_\mu}\right)^2 \left(3 - 2\frac{E_\nu}{E_\mu}\right) \sigma_{\nu N}(E_\nu) P(\nu_\mu \to \nu_\mu; \theta_{k\ell}, \Delta m_{k\ell}^2, \delta, C)$$

$$N_j^{\text{right}}(\mu^+; \theta_{k\ell}, \Delta m_{k\ell}^2, \delta, C)$$
$$= \frac{2 N_0 E_\mu}{\pi L^2 m_\mu^2} \int_{E_j}^{E_{j+1}} dE_{\bar{\nu}} \left(\frac{E_{\bar{\nu}}}{E_\mu}\right)^2 \left(3 - 2\frac{E_{\bar{\nu}}}{E_\mu}\right) \sigma_{\bar{\nu} N}(E_{\bar{\nu}}) P(\bar{\nu}_\mu \to \bar{\nu}_\mu; \theta_{k\ell}, \Delta m_{k\ell}^2, \delta, C),$$

where E_μ is the muon energy, L is the length of the neutrino path, N_0 is the number of the target nucleons times the number of useful decays of muons, $\sigma_{\nu N}(E_\nu)$ and $\sigma_{\bar{\nu} N}(E_{\bar{\nu}})$ are the (anti-)neutrino nucleon cross sections. We adopt the cross section which is the sum of those [65] of the quasi elastic scattering, one pion production, and inelastic scattering, where double counting of the latter two is suitably subtracted [66]. Throughout this section the threshold energy is assumed to be 0.1GeV which is close to what has been assumed for liquid argon detectors [54] and which may be realized in possible mega ton water Cherenkov detectors [67, 68].

The number of the free parameters in the present case is six (δ, θ_{12}, θ_{13}, θ_{23}, Δm_{21}^2, Δm_{21}^2), but the density $N_e(x) = Y_e(x)\rho(x)$ of electrons is not known exactly ($Y_e(x)$ is the ratio of the number of electrons to that of protons and neutrons, and $\rho(x)$ is the density of the Earth at a distance x from the beam production point), so we have to vary $N_e(x)$ also. Here for simplicity we assume the PREM (Preliminary Reference Earth Model) [69] and vary the overall normalization of the PREM:

$$A(x) = C A_0(x) = \sqrt{2} C G_F Y_e(x) N_e(x),$$

where $C = 1$ corresponds to the PREM. We have to consider correlations of errors of the CP phase and six other quantities and taking into account all

these errors we obtain the probability of rejecting a hypothesis $\bar{\delta} = 0$. To do that we look for the minimum value of $\Delta\chi^2(\theta_{k\ell}, \Delta m^2_{k\ell}, \delta, C; \bar{\theta}_{k\ell}, \overline{\Delta m^2_{k\ell}}, \bar{\delta}, \bar{C})$ by varying the six parameters $(\bar{\theta}_{12}, \bar{\theta}_{13}, \bar{\theta}_{23}, \overline{\Delta m^2_{21}}, \overline{\Delta m^2_{32}}, \bar{C})$:

$$\Delta\chi^2_{\min} \equiv \min_{\bar{\theta}_{k\ell}, \overline{\Delta m^2_{k\ell}}, \bar{C}} \Delta\chi^2(\theta_{k\ell}, \Delta m^2_{k\ell}, \delta, C; \bar{\theta}_{k\ell}, \overline{\Delta m^2_{k\ell}}, \bar{\delta} = 0, \bar{C}),$$

where C stands for the overall normalization of the electron density.

C.2 Correlations of errors of δ and other parameters

Let us first discuss correlations of two variables $(\bar{\delta}, \bar{X})$ where a parameter X stands for C, θ_{13}, θ_{12}, θ_{23}, Δm^2_{21} and Δm^2_{32}.

We have studied numerically correlations of errors between δ and the other oscillation parameters $(\theta_{k\ell}, \Delta m^2_{k\ell})$ as well as the normalization C of the matter effect for the case where the central values for these parameters are those of the best fit point, i.e., $\sin^2 2\theta_{12} = 0.75$, $\Delta m^2_{21} = 3.2 \times 10^{-5} \text{eV}^2$; $\sin^2 2\theta_{23} = 1.0$, $\Delta m^2_{32} = 3.2 \times 10^{-3} \text{eV}^2$, C=1.0 and we have used a reference value $8°$. The values of

$\Delta\chi^2(\theta_{12}, \theta_{13}, \theta_{23}, \Delta m^2_{21}, \Delta m^2_{32}, \delta, C; \theta_{12}, \theta_{13}, \theta_{23}, \Delta m^2_{21}, \Delta m^2_{32}, \bar{\delta}, \bar{C})$,
$\Delta\chi^2(\theta_{12}, \theta_{13}, \theta_{23}, \Delta m^2_{21}, \Delta m^2_{32}, \delta, C; \theta_{12}, \bar{\theta}_{13}, \theta_{23}, \Delta m^2_{21}, \Delta m^2_{32}, \bar{\delta}, C)$,
$\Delta\chi^2(\theta_{12}, \theta_{13}, \theta_{23}, \Delta m^2_{21}, \Delta m^2_{32}, \delta, C; \bar{\theta}_{12}, \theta_{13}, \theta_{23}, \Delta m^2_{21}, \Delta m^2_{32}, \bar{\delta}, C)$,
$\Delta\chi^2(\theta_{12}, \theta_{13}, \theta_{23}, \Delta m^2_{21}, \Delta m^2_{32}, \delta, C; \theta_{12}, \theta_{13}, \bar{\theta}_{23}, \underline{\Delta m^2_{21}}, \Delta m^2_{32}, \bar{\delta}, C)$,
$\Delta\chi^2(\theta_{12}, \theta_{13}, \theta_{23}, \Delta m^2_{21}, \Delta m^2_{32}, \delta, C; \theta_{12}, \theta_{13}, \theta_{23}, \Delta m^2_{21}, \underline{\Delta m^2_{32}}, \bar{\delta}, C)$,
$\Delta\chi^2(\theta_{12}, \theta_{13}, \theta_{23}, \Delta m^2_{21}, \Delta m^2_{32}, \delta, C; \theta_{12}, \theta_{13}, \theta_{23}, \Delta m^2_{21}, \overline{\Delta m^2_{32}}, \bar{\delta}, C)$

are plotted in Fig.C.1 – C.7 in the case of $\delta = \pi/2$ for E_μ=3, 20, 50 GeV, L=100 km, 1000 km, 2500 km, 6300 km, where the data size $10^{21}\mu\cdot10$kt is used as a reference value and no backgrounds are assumed. Since the number of degrees of freedom is 2, $\Delta\chi^2$=0.18, 0.34, 0.73 correspond to 1σ, 90%, 99% confidence level to reject a hypothesis with $\bar{\delta} = 0$.
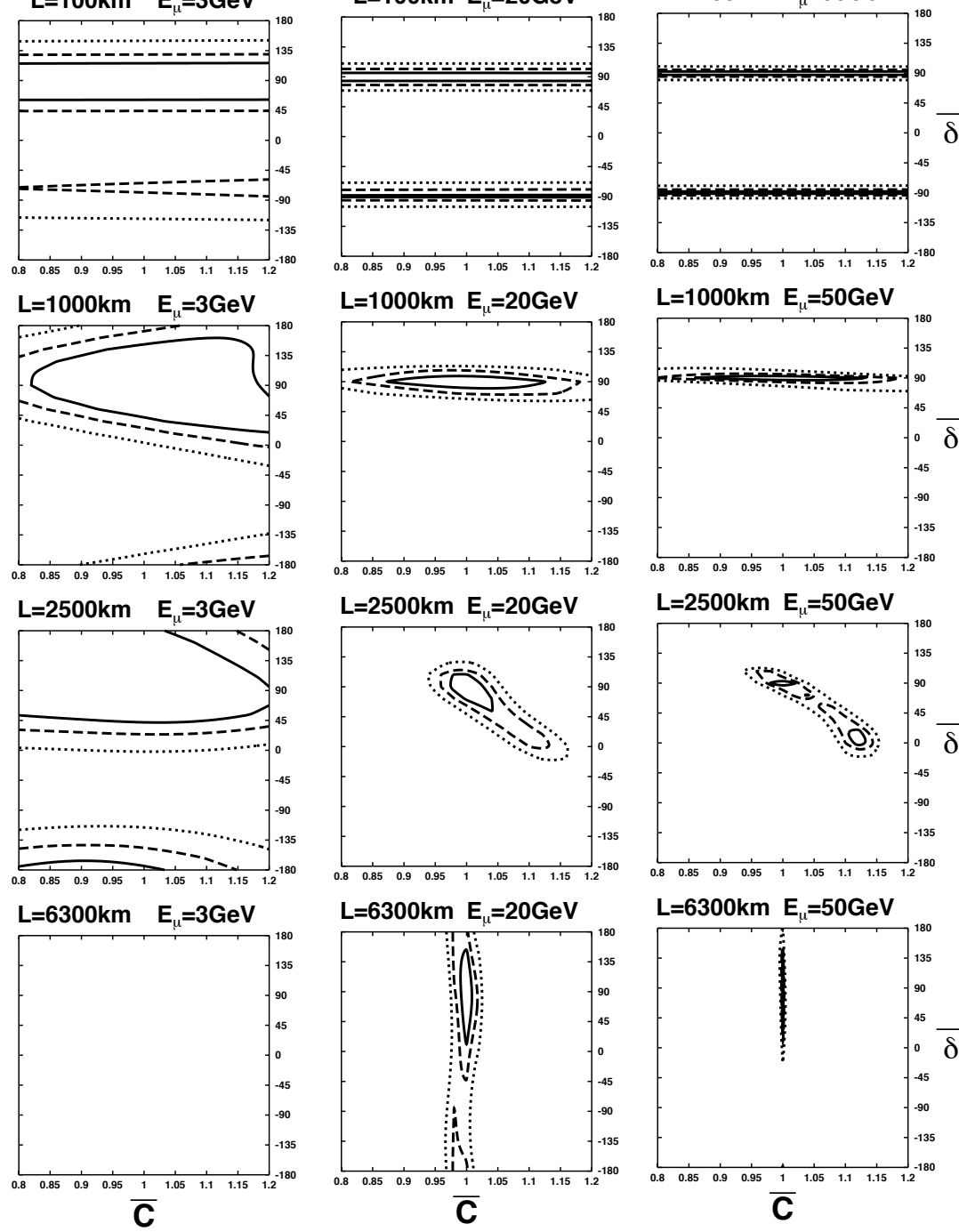
Figure C.1: Correlations of errors of $\bar{\delta}$ and the normalization $\bar{C}$ for L=100 km, 1000 km, 2500 km, 6300 km and for E_μ=3GeV, 20 GeV, 50 GeV. $\Delta\chi^2 = 0.18, 0.37, 0.73$ corresponds to 1σCL, 90%CL, 99%CL, respectively for two degrees of freedom. The oscillation parameters are $\Delta m_{21}^2 = 1.8 \times 10^{-5}\text{eV}^2$, $\Delta m_{32}^2 = 3.5 \times 10^{-5}\text{eV}^2$, $\sin^2 2\theta_{12} = 0.76$, $\sin^2 2\theta_{23} = 1.0$, $\theta_{13} = 8°$, $\delta = \pi/2$. The number of useful muon decays is $10^{21}\mu \cdot 10\text{kt}$. No backgrounds are taken into consideration in Figs. C.1 – C.7.

As can be seen in Fig.C.1, the correlation $(\bar{\delta}, \bar{C})$ for $L \sim 3000$ km is strong for $\theta_{13} = 8°$. The correlation $(\bar{\delta}, \bar{C})$ turns out to be small for larger values of Δm_{21}^2 or for smaller value of θ_{13} (i.e., $\theta_{13} \lesssim 3°$; See Fig.C.1b), as the gradient of the ellipse in the $(\bar{\delta}, \bar{C})$ plane becomes smaller for larger values of Δm_{21}^2. This is why strong correlations were not found in [54] where the set of parameters $(\sin^2 2\theta_{12} = 1.0, \Delta m_{21}^2 = 1.0 \times 10^{-4}\text{eV}^2; \sin^2 2\theta_{23} = 1.0, \Delta m_{32}^2 = 3.5(5,7) \times 10^{-3}\text{eV}^2)$ and $\sin^2 2\theta_{13} = 0.05$, $E_\mu = 30\text{GeV}$ were used. If we assume that the uncertainty in the overall normalization C is at most 5%, then the correlation $(\bar{\delta}, \bar{C})$ is not so serious, but if we assume that the uncertainty is as large as 20 % then the set of the parameters $(E_\mu \sim 50$ GeV, $L \sim 3000$ km) is not a good option. We will discuss this issue later.

¿From Figs. C.3 – C.7, we see that the correlations of $(\bar{\delta}, \bar{\theta}_{k\ell})$ and $(\bar{\delta}, \overline{\Delta m_{k\ell}^2})$ are not large for $L \gtrsim 1000$ km, $E_\mu \gtrsim 20$ GeV. As we will show analytically later, the value of $\Delta\chi^2(\theta_{k\ell}, \Delta m_{k\ell}^2, \delta, C; \bar{\theta}_{k\ell}, \overline{\Delta m_{k\ell}^2}, \bar{\delta} = 0, \bar{C})$ increases for $E_\mu \gg 50$ GeV and $L \ll 1000$ km unless we minimize it with respect to $\theta_{k\ell}$ and $\Delta m_{k\ell}^2$, but because of strong correlations in $(\bar{\delta}, \bar{\theta}_{13})$, $(\bar{\delta}, \bar{\theta}_{23})$ and $(\bar{\delta}, \overline{\Delta m_{32}^2})$, the value of $\Delta\chi^2_{\min}$, which is minimized with respect to $\theta_{k\ell}$ and $\Delta m_{k\ell}^2$, decreases for $E_\mu \gg 50$ GeV.

C.3 Data size to reject a hypothesis with $\bar{\delta} = 0$

The quantity $\Delta\chi^2_{\min}$ can be regarded as the deviation of χ^2 from the best fit point (the best fit point in eq. (C.1) is of course $\bar{\theta}_{k\ell} = \theta_{k\ell}, \overline{\Delta m_{k\ell}^2} = \Delta m_{k\ell}^2$, $\bar{\delta} = \delta$ and $\bar{C} = C$ for which we have $\Delta\chi^2_{\min} = 0$) and for six degrees of freedom the value of $\Delta\chi^2_{\min}$ which corresponds to 3σ (4σ) is 20.1 (28.9). From this we can estimate the necessary data size D to reject a hypothesis $\bar{\delta} = 0$ at 3σ by dividing 20.1 by $\Delta\chi^2_{\min}$ for each value of δ. On the other hand, it is important to include the effect of the backgrounds in the analysis [7, 54, 70]. Here we assume that the fraction f_B of backgrounds to right sign muon events is given by $f_B = 10^{-3}$ or 10^{-5} and that the systematic error of backgrounds is $\sigma_B = 0.1$ as in [70] for simplicity. We also assume the number of muons $10^{21}\mu \cdot 10\text{kt}$ as a reference value. Thus $\Delta\chi^2$ is modified as

$$\Delta\chi^2(\theta_{k\ell}, \Delta m_{k\ell}^2, \delta, C; \bar{\theta}_{k\ell}, \overline{\Delta m_{k\ell}^2}, \bar{\delta}, \bar{C})\Big|_{f_B}$$

$$\equiv \sum_j \frac{\left[N_j^{\text{wrong}}(\mu^-) - \bar{N}_j^{\text{wrong}}(\mu^-)\right]^2}{\left[\sqrt{N_j^{\text{wrong}}(\mu^-) + f_B N_j^{\text{right}}(\mu^+) + 1 + \frac{11}{9}}\right]^2 + \left[\sigma_B f_B N_j^{\text{right}}(\mu^+)\right]^2}$$
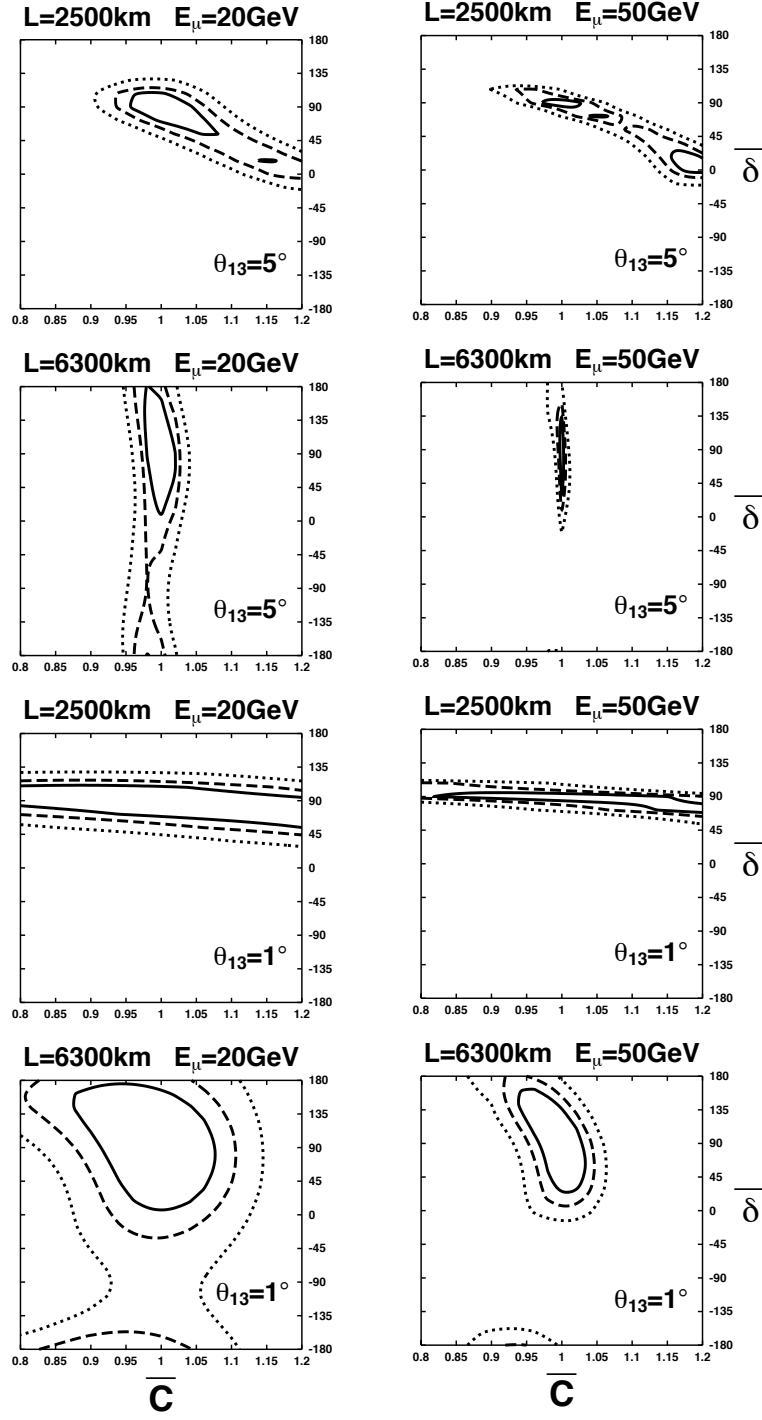
Figure C.2: The same correlation as Fig.1a for $\theta_{13} = 5°$, $1°$. The oscillation parameters and other reference values are the same as in Fig.C.1.

Figure C.3: Correlations of errors of $\bar{\delta}$ and $\bar{\theta}_{13}$. The oscillation parameters and other reference values are the same as in Fig.C.1.

74

L=100km E$_\mu$=3GeV

L=100km E$_\mu$=20GeV

L=100km E$_\mu$=50GeV

L=1000km E$_\mu$=3GeV

L=1000km E$_\mu$=20GeV

L=1000km E$_\mu$=50GeV

L=2500km E$_\mu$=3GeV

L=2500km E$_\mu$=20GeV

L=2500km E$_\mu$=50GeV

L=6300km E$_\mu$=3GeV

L=6300km E$_\mu$=20GeV

L=6300km E$_\mu$=50GeV

$\bar{\theta}_{12}$

$\bar{\delta}$

68%CL —— **90%CL** — — **99%CL** ⋅⋅⋅⋅⋅

Figure C.4: Correlations of errors of $\bar{\delta}$ and $\bar{\theta}_{12}$. The oscillation parameters and other reference values are the same as in Fig.C.1.

75
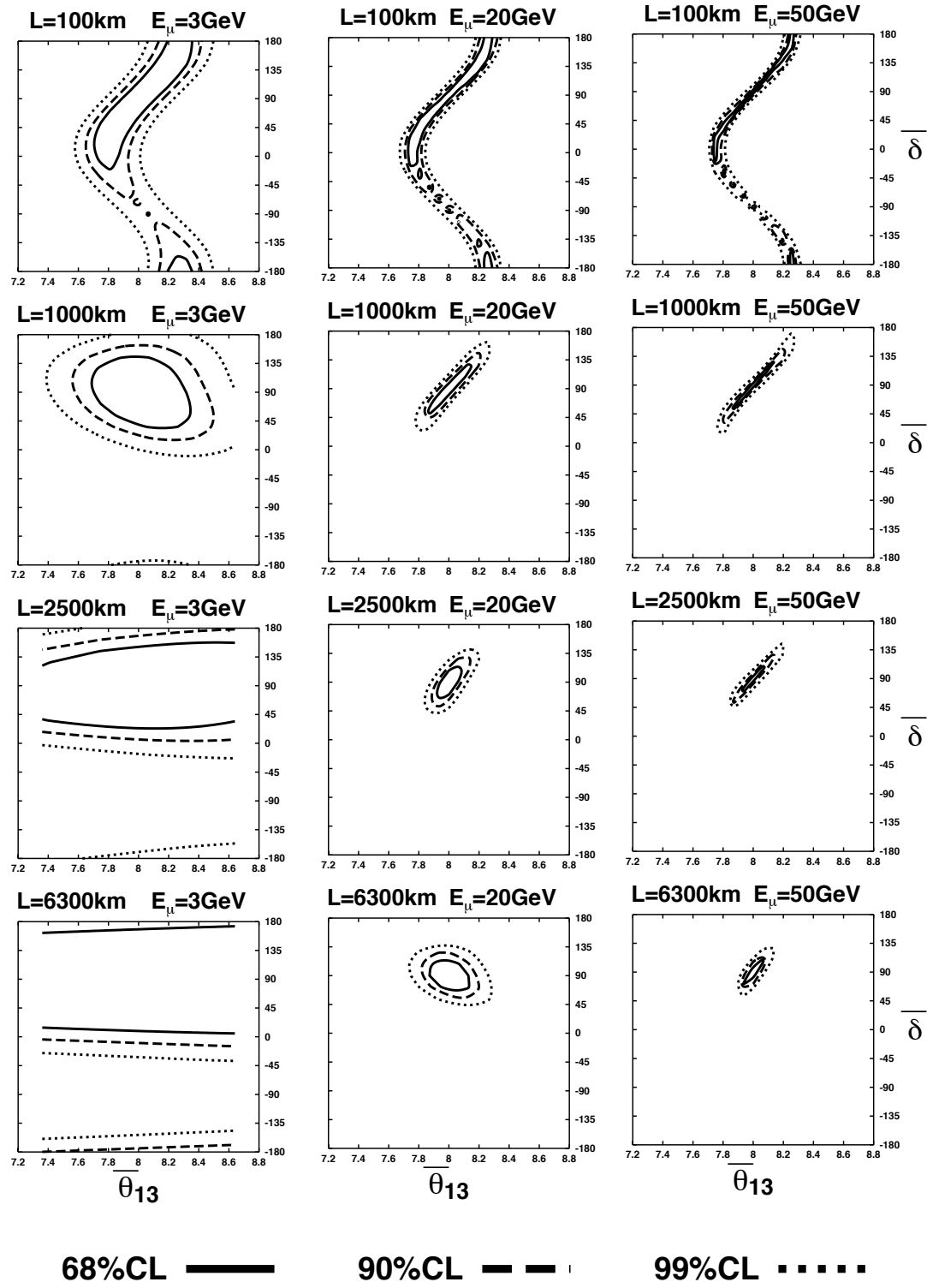
Figure C.5: Correlations of errors of $\bar{\delta}$ and $\bar{\theta}_{23}$. The oscillation parameters and other reference values are the same as in Fig.C.1.

Figure C.6: Correlations of errors of $\bar{\delta}$ and $\overline{\Delta m_{21}^2}$. The oscillation parameters and other reference values are the same as in Fig.C.1.

77

Figure C.7: Correlations of errors of $\bar{\delta}$ and $\overline{\Delta m_{32}^2}$. The oscillation parameters and other reference values are the same as in Fig.C.1.
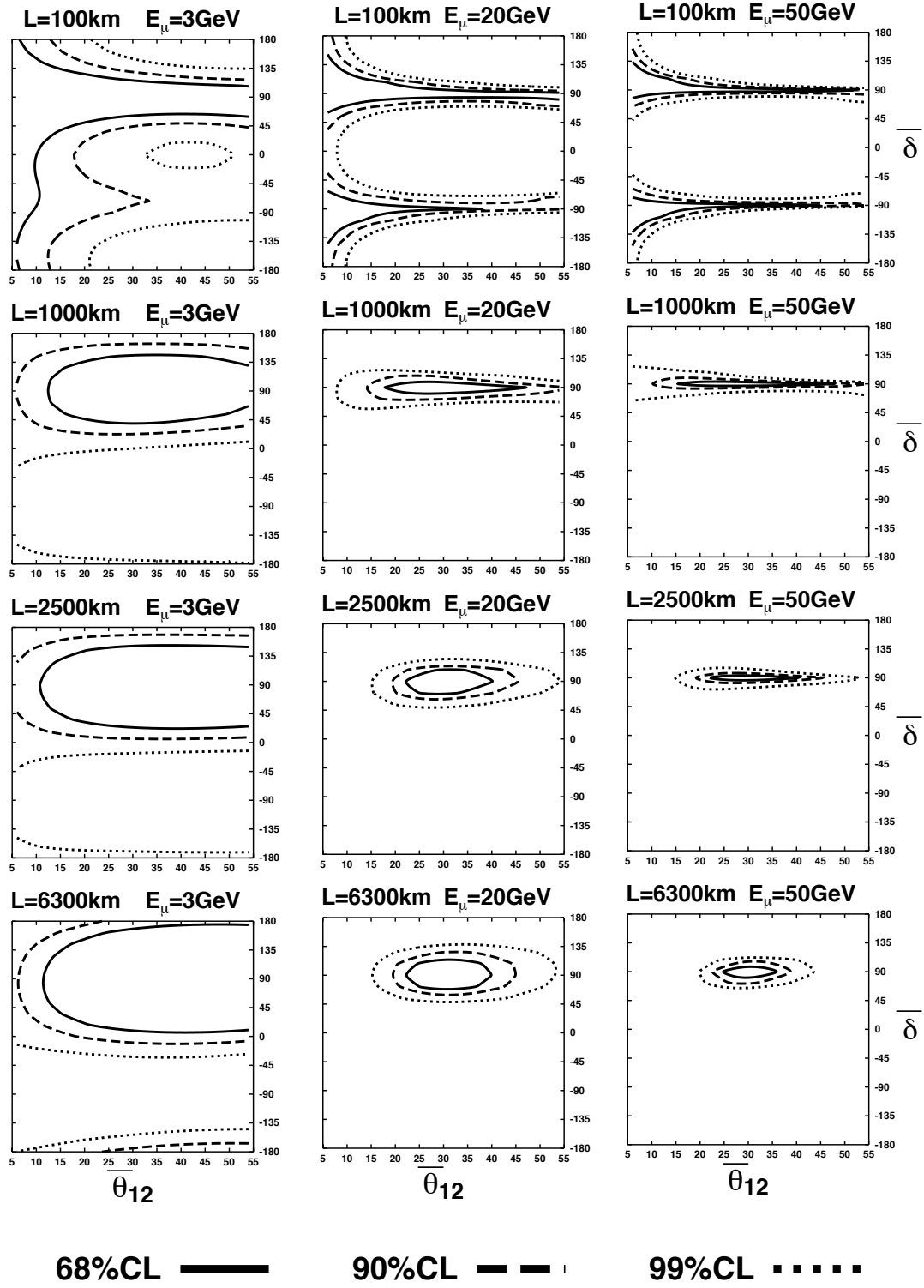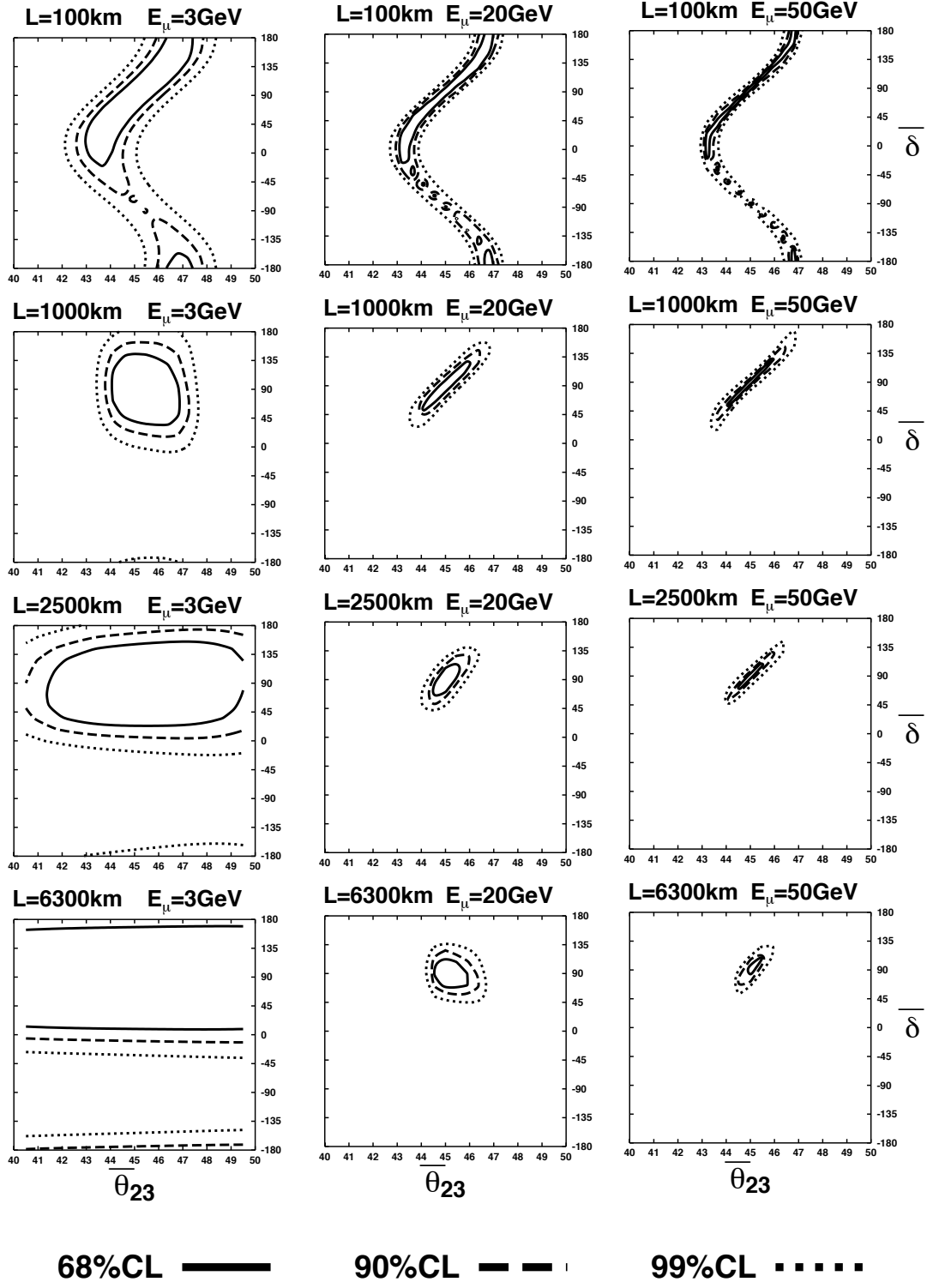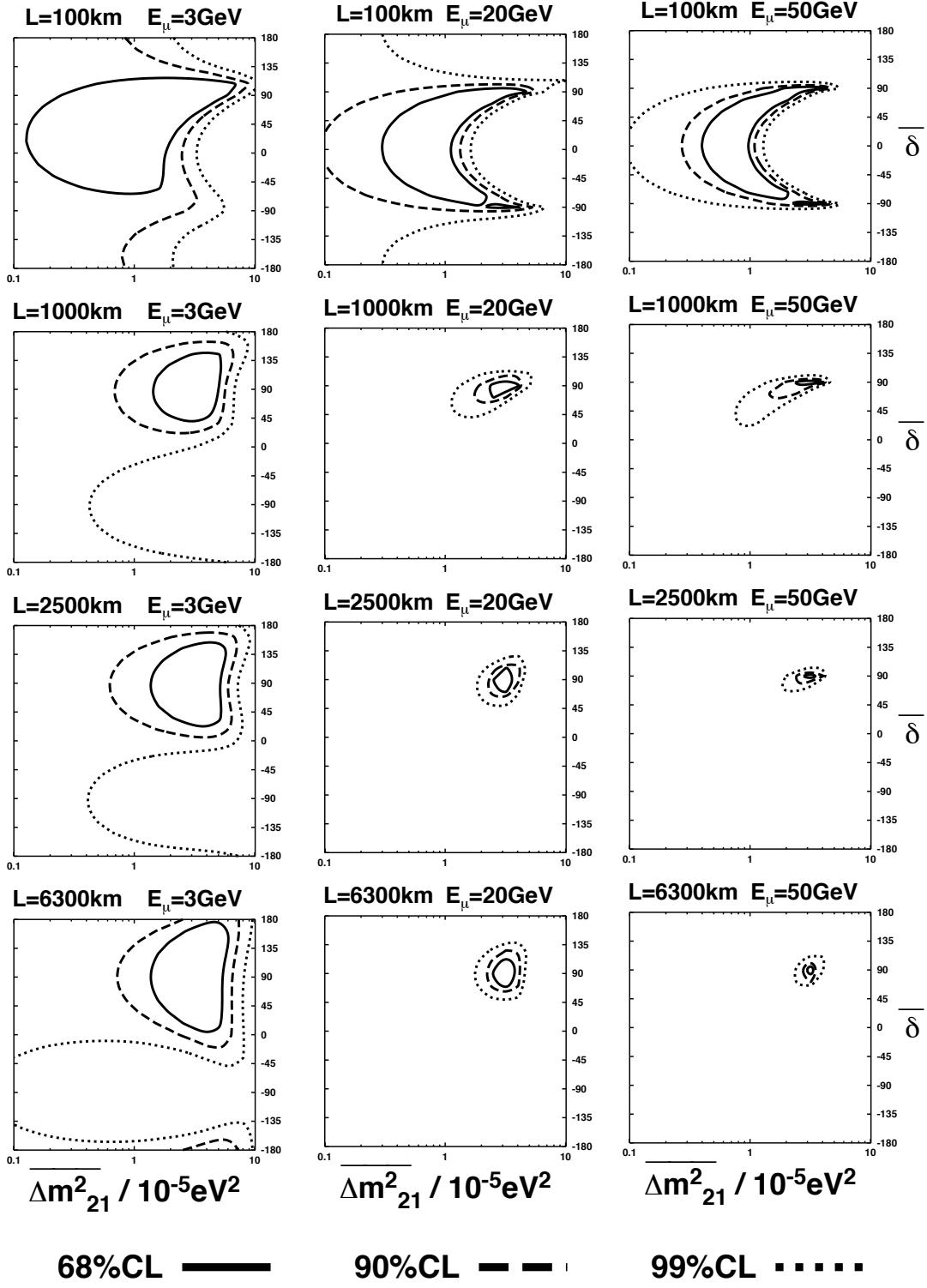
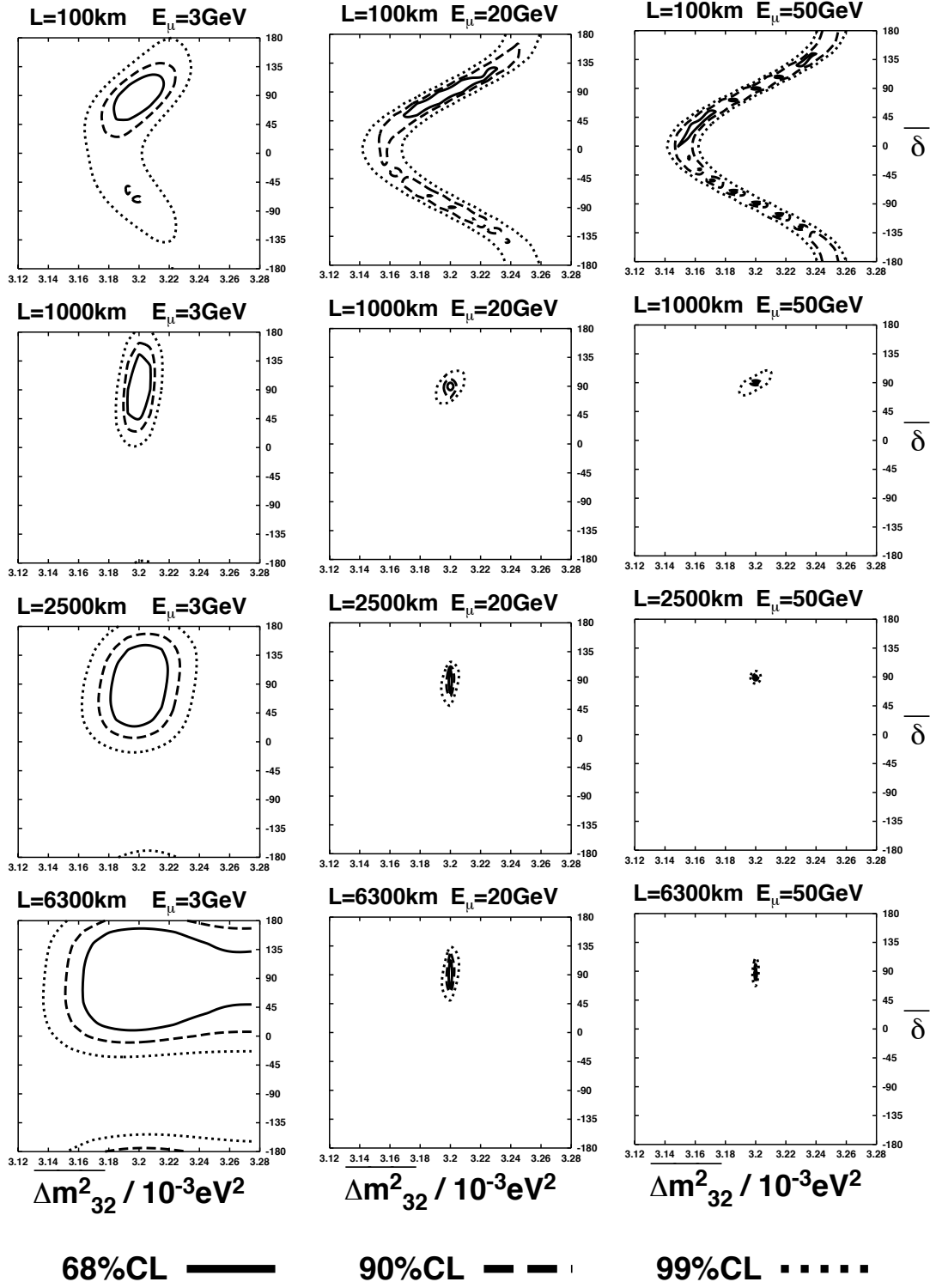78

$$
+ \sum_j \frac{\left[N_j^{\mathrm{wrong}}(\mu^+) - \bar{N}_j^{\mathrm{wrong}}(\mu^+)\right]^2}{\left[\sqrt{N_j^{\mathrm{wrong}}(\mu^+) + f_B N_j^{\mathrm{right}}(\mu^-) + 1 + \frac{11}{9}}\right]^2 + \left[\sigma_B f_B N_j^{\mathrm{right}}(\mu^-)\right]^2}
$$

$$
+ \sum_j \frac{\left[N_j^{\mathrm{right}}(\mu^-) - \bar{N}_j^{\mathrm{right}}(\mu^-)\right]^2}{N_j^{\mathrm{right}}(\mu^-)} + \sum_j \frac{\left[N_j^{\mathrm{right}}(\mu^+) - \bar{N}_j^{\mathrm{right}}(\mu^+)\right]^2}{N_j^{\mathrm{right}}(\mu^+)} \tag{C.2}
$$

where $\bar{N}_j^{\mathrm{wrong}}(\mu^\pm)$, $\bar{N}_j^{\mathrm{right}}(\mu^\pm)$ stand for $N_j^{\mathrm{wrong}}(\mu^\pm)$, $N_j^{\mathrm{right}}(\mu^\pm)$ with arguments $\bar{\theta}_{k\ell}, \overline{\Delta m_{k\ell}^2}, \bar{\delta}, \bar{C}$, respectively, and the corrections in the statistical errors are due to the Poisson statistical [70]. Then we minimize $\Delta\chi^2$ with respect $\bar{\theta}_{k\ell}, \overline{\Delta m_{k\ell}^2}$ and $\bar{C}$:

$$
\Delta\chi^2_{\mathrm{min}}\Big|_{f_B} \equiv \min_{\bar{\theta}_{k\ell}, \overline{\Delta m_{k\ell}^2}, \bar{C}} \Delta\chi^2(\theta_{k\ell}, \Delta m_{k\ell}^2, \delta, C; \bar{\theta}_{k\ell}, \overline{\Delta m_{k\ell}^2}, \bar{\delta} = 0, \bar{C})\Big|_{f_B} , \tag{C.3}
$$

where the values of oscillation parameters we use in (C.3) are the best fit values in the analyses of the solar and atmospheric neutrinos [41] as in Figs. C.1 – C.7, and we take $\theta_{13} = 1°$, $5°$, $8°$ and $\delta = \pi/2$ as a reference value. In varying the overall normalization C we assume $0.95 \leq C \leq 1.05$. We will mention the results for $|\Delta C| \leq 0.1$ and for $|\Delta C| \leq 0.2$ later. For other oscillation parameters, we vary $(\theta_{12}, \Delta m_{21}^2)$ and $(\theta_{23}, \Delta m_{32}^2)$ within the allowed region at 90%CL of the solar and the atmospheric neutrino data, i.e., $25° \leq \theta_{12} \leq 41°$, $35° \leq \theta_{23} \leq 55°$, $1.5 \times 10^{-5}\mathrm{eV}^2 \leq \Delta m_{21}^2 \leq 2.2 \times 10^{-4}\mathrm{eV}^2$, $1.6 \times 10^{-3}\mathrm{eV}^2 \leq \Delta m_{32}^2 \leq 4 \times 10^{-3}\mathrm{eV}^2$. It should be emphasized that in minimizing $\Delta\chi^2$ in (C.3) all the six parameters are varied at the same time, unlike in Figs. C.1 – C.7 which are obtained by varying only one of $\bar{\theta}_{k\ell}$, $\overline{\Delta m_{k\ell}^2}$, $\bar{C}$.

The result is given in Fig.C.8 for a neutrino factory with $0.5\mathrm{GeV} \leq E_\mu \leq 50\,\mathrm{GeV}$, $10\,\mathrm{km} \leq L \leq 10000\,\mathrm{km}$ and for three values of $\theta_{13} = 1°$, $5°$, $8°$ and two different values of the background fraction $f_B = 10^{-5}$, 10^{-3}. The behavior of the figures change a little depending on the value of θ_{13}. For $f_B = 10^{-3}$, the sensitivity to CP violation, i.e., the ability to reject a hypothesis with $\bar{\delta} = 0$ is *not* optimized by the set of parameters $(E_\mu, L) \simeq (50\text{ GeV}, 3000\text{ km})$, which has been advocated as the best choice, but rather by $(E_\mu, L) \simeq (20\text{ GeV}, 2000\text{ km})$. This is because with a nonnegligible fraction f_B the contribution of the systematic uncertainty $\sigma_B f_B N_j^{\mathrm{right}}$ to the total error becomes so large for high energy such as $E_\mu \sim 50$ GeV and sensitivity to CP violation is lost. For $f_B = 10^{-5}$ and $\theta_{13} = 1°$, on the other hand, the contribution of $\sigma_B f_B N_j^{\mathrm{right}}$ is not so large and the sensitivity is optimized by $(E_\mu, L) \simeq (50\text{ GeV}, 3000\text{ km})$. We note in passing that we have also optimized the sensitivity with respect to the number of energy bins but the conclusion does not depend very much on the number of energy bins. This result disagrees with the claim in [56].

We have also evaluated the data size assuming a larger uncertainty of the matter effect, i.e., $|\Delta C| \leq 0.1$ and $|\Delta C| \leq 0.2$. The results for $\theta_{13} = 8°$ are shown in Fig.C.9. If we have to assume an uncertainty of the matter effect which is as large as 20%, then the optimum baseline and muon energy become even smaller than the results with $|\Delta C| \leq 0.05$. The situation is less serious for smaller value of θ_{13}, i.e., $\theta_{13} \lesssim 3°$, for which the correlation $(\bar{\delta}, \bar{C})$ is not so strong. It should be noted that we have assumed in our analysis that the detection efficiency does not decrease down to the neutrino energy $E_\nu \sim$ a few GeV, so if this assumption is not satisfied then the optimum muon energy may not be as low as Fig.C.9 indicates.

In Figs. C.8 and C.9 we have taken $\delta = \pi/2$ as a reference value. It is possible to do the same analysis for a value of δ other than $\pi/2$. The results for $\theta_{13} = 8°$, 5° and 1° are given in Fig.C.10 for three sets of the parameters $(E_\mu = 50$ GeV, $L = 3000$ km$)$, $(E_\mu = 20$ GeV, $L = 1000$ km$)$ and $(E_\mu = 20$ GeV, $L = 2000$ km$)$. We observe that $(E_\mu = 50$ GeV, $L = 3000$ km$)$ is better than $(E_\mu = 20$ GeV, $L = 1000$ km$)$ for smaller values of θ_{13}, but for larger values of θ_{13} $(E_\mu = 20$ GeV, $L = 1000$ km$)$ can be more advantageous than the other. It should be emphasized that in all cases in Fig.C.10 we can distinguish the case of $\delta = \pi$ from that of $\delta = 0$, since the necessary data size to reject $\bar{\delta} = 0$ is finite even for $\delta = \pi$. This is because there are both contributions from $\sin \delta$ and $\cos \delta$ for the muon energy $E_\mu \lesssim 50$ GeV. As we will see in section 4, for extremely high energy $E_\mu \gg 50$ GeV we can show analytically that our $\Delta\chi^2(\text{CPV})$ becomes proportional to $\sin^2 \delta$ and distinction between $\delta = \pi$ and $\delta = 0$ is no longer possible.

C.4 Low and high energy behaviors of $\Delta\chi^2$

In this section we will show analytically that the sensitivity to CP and T violation decreases as $E_\mu \to$ small ($E_\mu \ll 10$ GeV) or $E_\mu \to$ large ($E_\mu \gg 50$ GeV). Throughout this section we assume $\sin^2 2\theta_{13} \gtrsim 10^{-3}$ ($\theta_{13} \gtrsim 1°$) so that we are always in the atmospheric regime in the language of [59], i.e., $\sin^2 2\theta_{13}/\sin^2 2\theta_{12} \gg (\Delta m_{21}^2/\Delta m_{31}^2)^2$. In this section we will ignore the effects of backgrounds and systematic errors for simplicity.

To examine significance of CP/T violation analytically, we introduce the following simplified quantities:

$$\Delta\chi^2(\text{CPV}) \equiv \min_{\bar{\theta}_{k\ell}, \overline{\Delta m_{k\ell}^2}, \bar{C}} \Delta\chi^2(\theta_{k\ell}, \Delta m_{k\ell}^2, \delta, C; \bar{\theta}_{k\ell}, \overline{\Delta m_{k\ell}^2}, \bar{\delta} = 0, \bar{C}),$$

$$\Delta\chi^2(\text{TV}) \equiv \frac{[\langle P(\nu_e \to \nu_\mu; \delta)\rangle - \langle P(\nu_\mu \to \nu_e; \delta)\rangle]^2}{\langle P(\nu_e \to \nu_\mu; \delta)\rangle},$$

where

$$\Delta\chi^2(\theta_{k\ell}, \Delta m_{k\ell}^2, \delta, C; \bar{\theta}_{k\ell}, \overline{\Delta m_{k\ell}^2}, \bar{\delta}, \bar{C})$$
$$= \frac{\left[\langle P(\nu_e \to \nu_\mu; \theta_{k\ell}, \Delta m_{k\ell}^2, \delta, C)\rangle - \langle P(\nu_e \to \nu_\mu; \bar{\theta}_{k\ell}, \overline{\Delta m_{k\ell}^2}, \bar{\delta}, \bar{C})\rangle\right]^2}{\langle P(\nu_e \to \nu_\mu; \delta)\rangle}$$

is defined as in (C.1),

$$\langle P(\nu_\alpha \to \nu_\beta; \delta)\rangle$$
$$\equiv \frac{12N_0 E_\mu^2}{\pi L^2 m_\mu^2} \int d\left(\frac{E_\nu}{E_\mu}\right) \left(\frac{E_\nu}{E_\mu}\right)^2 \left(1 - \frac{E_\nu}{E_\mu}\right) \sigma_{\nu N}(E_\nu) P(\nu_\alpha \to \nu_\beta; \delta) \quad (\text{C.4})$$

are the number of events ($(\alpha, \beta) = (e, \mu)$ or (μ, e); in the case of $(\alpha, \beta) = (\mu, e)$ we assume perfect polarization as in the previous section so that the number of events is given by the same definition (C.4)) and we have ignored effects of the backgrounds and systematic errors and correlations of errors for simplicity in this section. Also we will assume that the cross section is proportional to the neutrino energy E_ν for any E_ν, i.e., $\sigma = \sigma_0 E_\nu$. Strictly speaking this assumption is not accurate, but it is known [66] that $0 < \sigma < \sigma_0 E_\nu$ is satisfied for low energy $E_\nu \ll 1$GeV, so our approximation is sufficient to give an upper bound on the value of $\Delta\chi^2$ for low energy.

Let us first look at the low energy limit ($E_\nu \ll 10$ GeV). In this case matter effects are negligible and the probability can be replaced by that in vacuum. Thus we have

$$P(\nu_e \to \nu_\mu; \delta) \simeq s_{23}^2 \sin^2 2\theta_{13} \sin\left(\frac{\Delta E_{31} L}{2}\right) + c_{23}^2 \sin^2 2\theta_{12} \sin\left(\frac{\Delta E_{21} L}{2}\right)$$
$$+ 8\tilde{J} \sin\left(\frac{\Delta E_{21} L}{2}\right) \sin\left(\frac{\Delta E_{31} L}{2}\right) \cos\left(\delta + \frac{\Delta E_{31} L}{2}\right)$$

to the second order in $\mathcal{O}(\theta_{13})$ and $\mathcal{O}(\Delta E_{21}/\Delta E_{31})$, where

$$\tilde{J} \equiv \frac{c_{13}}{8} \sin 2\theta_{12} \sin 2\theta_{13} \sin 2\theta_{23},$$

and $\Delta E_{jk} \equiv \Delta m_{jk}^2/2E \equiv (m_j^2 - m_k^2)/2E$. The number of events are given by

$$
\begin{aligned}
&\langle P(\nu_e \to \nu_\mu; \delta) \rangle - \langle P(\nu_e \to \nu_\mu; \delta = 0) \rangle \\
&= \frac{96 N_0 E_\mu^3 \sigma_0 \tilde{J}}{\pi L^2 m_\mu^2} \int dx \ x^3 (1-x) \sin\left(\frac{\Delta m_{21}^2 L}{4 x E_\mu}\right) \\
&\times \ \sin\left(\frac{\Delta m_{31}^2 L}{4 x E_\mu}\right) \left[\cos\left(\delta + \frac{\Delta m_{31}^2 L}{4 x E_\mu}\right) - \cos\left(\frac{\Delta m_{31}^2 L}{4 x E_\mu}\right)\right] \quad \text{(C.5)}
\end{aligned}
$$

$$
\begin{aligned}
&\langle P(\nu_e \to \nu_\mu; \delta) \rangle - \langle P(\nu_\mu \to \nu_e; \delta) \rangle \\
&= \frac{192 N_0 E_\mu^3 \sigma_0 \tilde{J} \sin \delta}{\pi L^2 m_\mu^2} \int dx \ x^3 (1-x) \\
&\times \ \sin\left(\frac{\Delta m_{21}^2 L}{4 x E_\mu}\right) \sin\left(\frac{\Delta m_{31}^2 L}{4 x E_\mu}\right) \sin\left(\frac{\Delta m_{32}^2 L}{4 x E_\mu}\right) \quad \text{(C.6)}
\end{aligned}
$$

$$
\begin{aligned}
&\langle P(\nu_e \to \nu_\mu; \delta) \rangle \\
&\simeq \frac{12 s_{23}^2 \sin^2 2\theta_{13} E_\mu^3 \sigma_0}{\pi L^2 m_\mu^2} \int dx \ x^3 (1-x) \sin^2\left(\frac{\Delta m_{31}^2 L}{4 x E_\mu}\right), \quad \text{(C.7)}
\end{aligned}
$$

where $x \equiv E_\nu/E_\mu$, we have assumed conditions for the atmospheric regime $\sin^2 2\theta_{13}/\sin^2 2\theta_{12} \gg (\Delta m_{21}^2/\Delta m_{21}^2)^2$, and we have put $\bar{\theta}_{k\ell} = \theta_{k\ell}$, $\overline{\Delta m_{k\ell}^2} = \Delta m_{k\ell}^2$, $\bar{C} = C$ in (C.5) instead of optimizing $\langle P(\nu_e \to \nu_\mu; \delta) \rangle - \langle P(\nu_e \to \nu_\mu; \delta = 0) \rangle$ with respect to these variables, as that is sufficient to demonstrate that $\Delta\chi^2(\text{CPV})$ decreases as $E_\mu \to 0$. If we keep L/E_μ fixed while $L, E_\mu \to$ small, then all the quantities (C.5), (C.6) and (C.7) behave as $\mathcal{O}(E_\mu)$, so $\Delta\chi^2(\text{CPV}) \propto E_\mu$ and $\Delta\chi^2(\text{TV}) \propto E_\mu$ as $E_\mu \to 0$ with L/E_μ fixed. Thus sensitivity to CP/T violation is asymptotically lost as $E_\mu \to 0$. This is consistent with our numerical results in previous sections.

Next let us discuss the behavior of $\Delta\chi^2$ in the high energy limit ($E_\mu \gg 50\,\text{GeV}$). In this case we have to take into account the matter effect and we use the probability which has been obtained in [7] to second order in $\mathcal{O}(\theta_{13})$, $\mathcal{O}(\Delta E_{21}/\Delta E_{31})$, $\mathcal{O}(\Delta E_{21}/A)$ and $\mathcal{O}(\Delta E_{21} L)$:

$$
\begin{aligned}
P(\nu_e \to \nu_\mu; \delta) \ \simeq \ & s_{23}^2 \sin^2 2\theta_{13} \left(\frac{\Delta E_{31}}{B}\right)^2 \sin^2\left(\frac{BL}{2}\right) \\
+ \ & c_{23}^2 \sin^2 2\theta_{12} \left(\frac{\Delta E_{21}}{A}\right)^2 \sin^2\left(\frac{AL}{2}\right) \\
+ \ & 8\tilde{J}\frac{\Delta E_{21}}{A}\frac{\Delta E_{31}}{B} \sin\left(\frac{AL}{2}\right) \sin\left(\frac{BL}{2}\right) \cos\left(\delta + \frac{\Delta E_{31} L}{2}\right).
\end{aligned}
$$
(C.8)

Since we assume $\sin^2 2\theta_{13}/\sin^2 2\theta_{12} \gg (\Delta m_{21}^2/\Delta m_{21}^2)^2 = (\Delta E_{21}/\Delta E_{31})^2$ here, we can ignore the second term in (C.8).

It is straightforward to get the following high energy limit of $\Delta\chi^2(\text{TV})$. Using (C.8) we have

$$P(\nu_e \to \nu_\mu; \delta) - P(\nu_\mu \to \nu_e; \delta) = P(\nu_e \to \nu_\mu; \delta) - P(\nu_e \to \nu_\mu; -\delta)$$

$$\simeq -2\tilde{J}\frac{\Delta m_{21}^2 \left(\Delta m_{31}^2\right)^2}{E_\nu^3}\frac{L}{A^2}\sin^2\left(\frac{AL}{2}\right),$$

where we have expanded $\sin(\Delta E_{21}L/2) \simeq \Delta E_{21}L/2$ and have used the fact $B = [(\Delta E_{31}\cos 2\theta_{13} - A)^2 + (\Delta E_{31}\sin 2\theta_{13})^2]^{1/2} \simeq A$ as $E_\nu \to$ large. Therefore the number of events is given by

$$\langle P(\nu_e \to \nu_\mu; \delta)\rangle - \langle P(\nu_\mu \to \nu_e; \delta)\rangle$$

$$\simeq \frac{24N_0\sigma_0\tilde{J}\sin\delta\,\Delta m_{21}^2 \left(\Delta m_{31}^2\right)^2}{\pi m_\mu^2}\frac{1}{A^2L}\sin^2\left(\frac{AL}{2}\right)\int dx\,(1-x)$$

$$= \frac{12N_0\sigma_0\tilde{J}\sin\delta\,\Delta m_{21}^2 \left(\Delta m_{31}^2\right)^2}{\pi m_\mu^2}\frac{1}{A^2L}\sin^2\left(\frac{AL}{2}\right),$$

$$\langle P(\nu_e \to \nu_\mu; \delta)\rangle$$

$$\simeq \frac{3N_0\sigma_0 s_{23}^2 \sin^2 2\theta_{13}}{\pi m_\mu^2}\frac{E_\mu}{A^2L^2}\sin^2\left(\frac{AL}{2}\right)\int dx\,x(1-x)$$

$$= \frac{N_0\sigma_0 s_{23}^2 \sin^2 2\theta_{13}}{2\pi m_\mu^2}\frac{E_\mu}{A^2L^2}\sin^2\left(\frac{AL}{2}\right).$$

Hence we have the behaviors

$$\Delta\chi^2(\text{TV}) \simeq \frac{N_0\sigma_0}{\pi m_\mu^2}\frac{288\sin^2\delta\,\tilde{J}^2 \left(\Delta m_{21}^2\right)^2 \left(\Delta m_{31}^2\right)^4}{s_{23}^2 \sin^2 2\theta_{13}}\frac{1}{E_\mu A^2}\sin^2\left(\frac{AL}{2}\right) \quad \text{(C.9)}$$

$$\text{as } E_\mu \to \text{large}.$$

(C.9) indicates that the sensitivity to T violation decreases as E_μ becomes very large. Also for a fixed large E_μ, $\Delta\chi^2(\text{TV})$ is optimized for $L \sim \pi/A \sim 3 \times 2000\text{km}/(\rho/2.7\text{g·cm}^{-3}) \sim 5000$ km. From numerical calculations we see that $\Delta\chi^2(\text{TV})$ is optimized for $(L, E_\mu) \sim (3000\text{ km}, 50\text{ GeV})$ (see Fig.C.1), so our analytic treatment is consistent with numerical calculations qualitatively.

The behavior of $\Delta\chi^2(\text{CPV})$ is a little more complicated, as we have to optimize $\Delta\chi^2$ with respect to $\bar{\theta}_{k\ell}$, $\overline{\Delta m_{k\ell}^2}$, $\bar{C}$. If we put $\bar{\theta}_{k\ell} = \theta_{k\ell}$, $\overline{\Delta m_{k\ell}^2} = \Delta m_{k\ell}^2$, $\bar{C} = C$ as we did in (C.5), we have

$$P(\nu_e \to \nu_\mu; \delta) - P(\nu_e \to \nu_\mu; \delta = 0)$$

$$\simeq 2\tilde{J}(\cos\delta - 1)\frac{\Delta m_{21}^2 \Delta m_{31}^2}{E_\nu^2}\frac{1}{A^2}\sin^2\left(\frac{AL}{2}\right),$$

$$\langle P(\nu_e \to \nu_\mu; \delta)\rangle - \langle P(\nu_e \to \nu_\mu; \delta = 0)\rangle$$

$$= \frac{4N_0\sigma_0\tilde{J}(\cos\delta - 1)\Delta m_{21}^2 \Delta m_{31}^2}{\pi m_\mu^2}\frac{E_\mu}{A^2L^2}\sin^2\left(\frac{AL}{2}\right),$$

83

so that we naively have the following behavior

$$\Delta\chi^2(\text{naive CPV}) \simeq \frac{N_0\sigma_0}{\pi m_\mu^2} \frac{32(\cos\delta - 1)^2 \tilde{J}^2 \left(\Delta m_{21}^2\right)^2 \left(\Delta m_{31}^2\right)^2}{s_{23}^2 \sin^2 2\theta_{13}} \frac{E_\mu}{A^2 L^2} \sin^2\left(\frac{AL}{2}\right).$$

$$(\text{C.10})$$

It turns out that it is sufficient to consider the correlation of two variables $(\bar\delta, \bar X)$, where X is $\theta_{k\ell}$, $\Delta m_{k\ell}^2$ or C, to demonstrate $\Delta\chi^2(\text{CPV}) \propto 1/E_\mu$. Except for the correlations $(\bar\delta, \bar\theta_{12})$ and $(\bar\delta, \overline{\Delta m_{21}^2})$, we can ignore terms of order $\mathcal{O}((\Delta E_{21}/\Delta E_{31})^2)$. From the assumption $\sin^2 2\theta_{13}/\sin^2 2\theta_{12} \gg (\Delta m_{21}^2/\Delta m_{31}^2)^2$, (C.8) is approximately given by

$$P(\nu_e \to \nu_\mu; \delta) \simeq \left[s_{23} \sin 2\theta_{13} \frac{\Delta E_{31}}{A} \sin\left(\frac{AL}{2}\right) \right.$$

$$\left. + \frac{4\tilde{J}}{s_{23}\sin 2\theta_{13}} \frac{\Delta E_{21}}{A} \sin\left(\frac{AL}{2}\right) \cos\left(\delta + \frac{\Delta E_{31}L}{2}\right) \right]^2,$$

where we have used $A - \Delta E_{31} \simeq A$ for $E_\nu \to$ large, and we have ignored terms of order $\mathcal{O}((\Delta E_{21}/\Delta E_{31})^2)$. In the case of the two variable correlation $(\bar\delta, \bar\theta_{13})$, to minimize the square of

$$P(\nu_e \to \nu_\mu; \theta_{13}, \delta) - P(\nu_e \to \nu_\mu; \bar\theta_{13}, \bar\delta)$$

$$\simeq \left[s_{23} \sin 2\theta_{13} \frac{\Delta E_{31}}{A} \sin\left(\frac{AL}{2}\right) + \frac{4\tilde{J}}{s_{23}\sin 2\theta_{13}} \frac{\Delta E_{21}}{A} \sin\left(\frac{AL}{2}\right) \cos\left(\delta + \frac{\Delta E_{31}L}{2}\right) \right]^2$$

$$- \left[s_{23} \sin 2\bar\theta_{13} \frac{\Delta E_{31}}{A} \sin\left(\frac{AL}{2}\right) + \frac{4\tilde{J}}{s_{23}\sin 2\theta_{13}} \frac{\Delta E_{21}}{A} \sin\left(\frac{AL}{2}\right) \cos\left(\bar\delta + \frac{\Delta E_{31}L}{2}\right) \right]^2,$$

$$(\text{C.11})$$

it is sufficient to take[2]

$$\sin 2\bar\theta_{13} = \sin 2\theta_{13} - \frac{4\tilde{J}}{s_{23}^2 \sin 2\theta_{13}} \frac{\Delta m_{21}^2}{\Delta m_{31}^2} \left(\cos\bar\delta - \cos\delta\right), \qquad (\text{C.12})$$

where we have used in (C.11) and (C.12) the fact $\tilde{J}/\sin 2\theta_{13} = \cos\theta_{13}\times$ (independent of θ_{13}) $\simeq \cos\bar\theta_{13} \times$ (independent of θ_{13}) which holds because $\sin^2\theta_{13} \ll 1$. Notice that the phase $\Delta E_{31}L/2$ which appears together with δ in cosine in (C.11) disappears as $E_\nu \to$ large. Plugging (C.12) in (C.11), we find

$$P(\nu_e \to \nu_\mu; \theta_{13}, \delta) - P(\nu_e \to \nu_\mu; \bar\theta_{13}, \bar\delta)$$

$$\simeq s_{23}^2 \left(\frac{\Delta E_{31}}{A}\right)^2 \sin^2\left(\frac{AL}{2}\right) \left(\sin^2 2\theta_{13} - \sin^2 2\bar\theta_{13}\right)$$

---

[2]Here we do not discuss the other solution of the quadratic equation which was discussed by [59], since we are mainly interested in rejecting $\bar\delta = 0$ rather than determining the precise value of δ.

$$+ \quad 8\tilde{J}\frac{\Delta E_{21}\Delta E_{31}}{A^2}\sin^2\left(\frac{AL}{2}\right)\left[\cos\left(\delta+\frac{\Delta E_{31}L}{2}\right) - \cos\left(\bar{\delta}+\frac{\Delta E_{31}L}{2}\right)\right]$$

$$\simeq \quad 8\tilde{J}\frac{\Delta E_{21}\Delta E_{31}}{A^2}\sin^2\left(\frac{AL}{2}\right)$$

$$\times \quad \left[\cos\left(\delta+\frac{\Delta E_{31}L}{2}\right) - \cos\left(\bar{\delta}+\frac{\Delta E_{31}L}{2}\right) - \cos\delta + \cos\bar{\delta}\right],$$

$$\simeq \quad 8\tilde{J}\frac{\Delta E_{21}\Delta E_{31}}{A^2}\sin^2\left(\frac{AL}{2}\right)\left(\sin\bar{\delta} - \sin\delta\right)\frac{\Delta E_{31}L}{2}, \tag{C.13}$$

where we have expanded $\sin(\Delta E_{31}L/2) \simeq \Delta E_{31}L/2$, $\cos(\Delta E_{31}L/2) - 1 \simeq -(\Delta E_{31}L)^2/2 \simeq 0$ in the last step in (C.13). Hence we get

$$\left\langle P(\nu_e \to \nu_\mu; \theta_{13}, \delta) - P(\nu_e \to \nu_\mu; \bar{\theta}_{13}, \bar{\delta}=0)\right\rangle$$

$$\simeq \quad -\frac{6N_0\sigma_0}{\pi m_\mu^2}\tilde{J}\sin\delta\frac{\Delta m_{21}^2\left(\Delta m_{31}^2\right)^2}{A^2L^2}\sin^2\left(\frac{AL}{2}\right)\int dx(1-x)$$

$$= \quad \frac{3N_0\sigma_0}{\pi m_\mu^2}\tilde{J}\sin\delta\Delta m_{21}^2\left(\Delta m_{31}^2\right)^2\frac{\sin^2\left(AL/2\right)}{A^2L^2}. \tag{C.14}$$

We see from (C.14) that if we optimize $\Delta\chi^2(\text{CPV})$ with respect only to $\bar{\theta}_{13}$ then $\Delta\chi^2(\text{CPV})$ behaves as

$$\Delta\chi^2(\text{CPV}; (\delta, \theta_{13})) \simeq \frac{18N_0\sigma_0}{\pi m_\mu^2}\frac{\tilde{J}^2\sin^2\delta\left(\Delta m_{21}^2\right)^2\left(\Delta m_{31}^2\right)^2}{s_{23}^2\sin^2 2\theta_{13}}\frac{\sin^2\left(AL/2\right)}{E_\mu A^2}. \tag{C.15}$$

Note that the behavior of $\Delta\chi^2(\text{CPV}; (\delta, \theta_{13}))$ which is optimized with respect to $\bar{\theta}_{13}$ is quite different from that of $\Delta\chi^2(\text{naive CPV})$ in (C.10). We observe that the dependence of $\Delta\chi^2(\text{CPV}; (\delta, \theta_{13}))$ on E_μ is the same as that of $\Delta\chi^2(\text{TV})$. It should be also emphasized that $\Delta\chi^2(\text{CPV}; (\delta, \theta_{13}))$ is proportional to $\sin^2\delta$ and does not depend on $\cos\delta$ unlike $\Delta\chi^2(\text{naive CPV})$ in (C.10).

We can play the same game for θ_{23}, Δm_{32}^2 and C. In the case of the two variable correlation $(\bar{\delta}, \bar{\theta}_{23})$,

$$\sin\bar{\theta}_{23} = \sin\theta_{23} - \frac{4\tilde{J}}{s_{23}\sin^2 2\theta_{13}}\frac{\Delta m_{21}^2}{\Delta m_{31}^2}\left(\cos\bar{\delta} - \cos\delta\right) \tag{C.16}$$

minimizes $\Delta\chi^2(\text{CPV}; (\delta, \theta_{23}))$ and we have

$$\Delta\chi^2(\text{CPV}; (\delta, \theta_{23})) \simeq \frac{18N_0\sigma_0}{\pi m_\mu^2}\frac{\tilde{J}^2\sin^2\delta\left(\Delta m_{21}^2\right)^2\left(\Delta m_{31}^2\right)^2}{s_{23}^2\sin^2 2\theta_{13}}\frac{\sin^2\left(AL/2\right)}{E_\mu A^2},$$

which is the same as $\Delta\chi^2(\text{CPV}; (\delta, \theta_{13}))$. In the case of the two variable correlation $(\bar{\delta}, \overline{\Delta m_{32}^2})$, using

$$P(\nu_e \to \nu_\mu; \delta)$$

$$\simeq \quad \left[s_{23}\sin 2\theta_{13}\frac{\Delta E_{31}}{A}\sin\left(\frac{AL}{2}\right) + \frac{4\tilde{J}}{s_{23}\sin 2\theta_{13}}\frac{\Delta E_{21}}{A}\sin\left(\frac{AL}{2}\right)\cos\delta\right]^2,$$

we find

$$\overline{\Delta m_{31}^2} = \Delta m_{31}^2 - \frac{4\tilde{J}}{s_{23}^2 \sin^2 2\theta_{13}} \Delta m_{21}^2 \left(\cos\bar{\delta} - \cos\delta\right) \tag{C.17}$$

minimizes $\Delta\chi^2(\text{CPV}; (\delta, \Delta m_{31}^2))$. We obtain

$$\Delta\chi^2(\text{CPV}; (\delta, \Delta m_{31}^2)) \simeq \frac{18 N_0 \sigma_0}{\pi m_\mu^2} \frac{\tilde{J}^2 \sin^2\delta \left(\Delta m_{21}^2\right)^2 \left(\Delta m_{31}^2\right)^2}{s_{23}^2 \sin^2 2\theta_{13}} \frac{\sin^2\left(AL/2\right)}{E_\mu A^2},$$

which again is the same as $\Delta\chi^2(\text{CPV}; (\delta, \theta_{13}))$. In the case of the two variable correlation $(\bar{\delta}, \bar{C})$,

$$\frac{\sin\left(\bar{A}L/2\right)}{\bar{A}} = \frac{\sin\left(AL/2\right)}{A} \left[1 - \frac{4\tilde{J}}{s_{23}^2 \sin^2 2\theta_{13}} \frac{\Delta m_{21}^2}{\Delta m_{31}^2} \left(\cos\bar{\delta} - \cos\delta\right)\right] \tag{C.18}$$

minimizes $\Delta\chi^2(\text{CPV}; (\delta, C))$ and we get

$$\Delta\chi^2(\text{CPV}; (\delta, C)) \simeq \frac{18 N_0 \sigma_0}{\pi m_\mu^2} \frac{\tilde{J}^2 \sin^2\delta \left(\Delta m_{21}^2\right)^2 \left(\Delta m_{31}^2\right)^2}{s_{23}^2 \sin^2 2\theta_{13}} \frac{\sin^2\left(AL/2\right)}{E_\mu A^2},$$

which once again is the same as $\Delta\chi^2(\text{CPV}; (\delta, \theta_{13}))$. The expressions (C.12), (C.16), (C.17) and (C.18) for the optimal values for $\bar{\theta}_{13}$, $\bar{\theta}_{23}$, $\overline{\Delta m_{31}^2}$ and $\bar{C}$ explain why the correlation has a cosine curve for large E_μ and small L in Figs. 1, 2, 4 and 6.

In the case of the correlations $(\bar{\delta}, \bar{\theta}_{12})$, and $(\bar{\delta}, \overline{\Delta m_{21}^2})$, we have to take into account of terms of order $\mathcal{O}((\Delta E_{21}/\Delta E_{31})^2)$. For $(\bar{\delta}, \bar{\theta}_{12})$, we have

$$\begin{aligned}
\sin 2\bar{\theta}_{12} &= -\frac{4\tilde{J}}{c_{23}^2} \frac{\Delta m_{31}^2}{\Delta m_{21}^2} \cos\bar{\delta} + \left[\left(\frac{4\tilde{J}}{c_{23}^2} \frac{\Delta m_{31}^2}{\Delta m_{21}^2}\right)^2 \cos^2\bar{\delta}\right.\\
&\quad + \left. \frac{8\tilde{J}}{c_{23}^2} \frac{\Delta m_{31}^2}{\Delta m_{21}^2} \cos\delta \sin 2\theta_{12} + \sin^2 2\theta_{12}\right]^{\frac{1}{2}}, \tag{C.19}
\end{aligned}$$

and this optimizes $\Delta\chi^2(\text{CPV})$. We find

$$\begin{aligned}
&P(\nu_e \to \nu_\mu; \theta_{12}, \delta) - P(\nu_e \to \nu_\mu; \bar{\theta}_{12}, \bar{\delta})\\
\simeq\quad &\frac{8\tilde{J}}{\sin 2\theta_{12}} \frac{\Delta E_{21}\Delta E_{31}}{A^2} \sin^2\left(\frac{AL}{2}\right) \left[\sin 2\theta_{12} \cos\left(\delta + \frac{\Delta E_{31}L}{2}\right)\right.\\
&- \left.\sin 2\bar{\theta}_{12} \cos\left(\bar{\delta} + \frac{\Delta E_{31}L}{2}\right) - \sin 2\theta_{12} \cos\delta + \sin 2\bar{\theta}_{12} \cos\bar{\delta}\right]\\
\simeq\quad &\frac{8\tilde{J}}{\sin 2\theta_{12}} \frac{\Delta E_{21}\Delta E_{31}}{A^2} \sin^2\left(\frac{AL}{2}\right) \left(\sin\bar{\delta} \sin 2\bar{\theta}_{12} - \sin\delta \sin 2\theta_{12}\right) \frac{\Delta E_{31}L}{2},
\end{aligned}$$

where we have expanded $\sin(\Delta E_{31}L/2) \simeq \Delta E_{31}L/2$. By putting $\bar{\delta} = 0$, we obtain

$$\Delta\chi^2(\text{CPV}; (\delta, \theta_{12})) \simeq \frac{18 N_0 \sigma_0}{\pi m_\mu^2} \frac{\tilde{J}^2 \sin^2\delta \left(\Delta m_{21}^2\right)^2 \left(\Delta m_{31}^2\right)^2}{s_{23}^2 \sin^2 2\theta_{13}} \frac{\sin^2\left(AL/2\right)}{E_\mu A^2},$$

86

which once again is the same as $\Delta\chi^2(\text{CPV}; (\delta, \theta_{13}))$. For $(\bar{\delta}, \overline{\Delta m_{21}^2})$, we have

$$
\overline{\Delta m_{21}^2} = -\frac{4\tilde{J}}{c_{23}^2 \sin^2 2\theta_{12}} \Delta m_{31}^2 \cos\bar{\delta} + \left[\left(\frac{4\tilde{J}}{c_{23}^2 \sin^2 2\theta_{12}}\right)^2 \cos^2\bar{\delta} \left(\Delta m_{31}^2\right)^2 \right.
$$

$$
+ \left. \frac{8\tilde{J}}{c_{23}^2 \sin^2 2\theta_{12}} \Delta m_{21}^2 \Delta m_{31}^2 \cos\delta + \left(\Delta m_{21}^2\right)^2 \right]^{\frac{1}{2}} \tag{C.20}
$$

which leads to

$$
P(\nu_e \to \nu_\mu; \Delta m_{21}^2, \delta) - P(\nu_e \to \nu_\mu; \overline{\Delta m_{21}^2}, \bar{\delta})
$$
$$
\simeq 8\tilde{J}\frac{\Delta E_{21}\Delta E_{31}}{A^2} \sin^2\left(\frac{AL}{2}\right)\left(\sin\bar{\delta} - \sin\delta\right)\frac{\Delta E_{31}L}{2}.
$$

Thus we get

$$
\Delta\chi^2(\text{CPV}; (\delta, \Delta m_{21}^2)) \simeq \frac{18N_0\sigma_0}{\pi m_\mu^2} \frac{\tilde{J}^2 \sin^2\delta \left(\Delta m_{21}^2\right)^2 \left(\Delta m_{31}^2\right)^2}{s_{23}^2 \sin^2 2\theta_{13}} \frac{\sin^2\left(AL/2\right)}{E_\mu A^2},
$$

which once again is the same as $\Delta\chi^2(\text{CPV}; (\delta, \theta_{13}))$. Unlike the cases for $(\bar{\delta}, \bar{\theta}_{13})$, $(\bar{\delta}, \bar{\theta}_{23})$, $(\bar{\delta}, \overline{\Delta m_{31}^2})$ and $(\bar{\delta}, \bar{C})$, the optimal values (C.19) and (C.20) have nontrivial behaviors even for large E_μ and small L, as we can see from Figs. 3 and 5.

We have seen analytically that two variable correlations give us the behavior $\Delta\chi^2(\text{CPV}) \propto \sin^2\delta/E_\mu$ and this behavior is the same as $\Delta\chi^2(\text{TV})$. Although it is difficult to discuss correlations of more than two variables analytically, the discussions above are sufficient to demonstrate that sensitivity to CP violation decreases as E_μ becomes larger. In fact we have verified numerically that $\Delta\chi^2(\text{CPV})$ decreases as the muon energy increases ($E_\mu \gtrsim$ 100 GeV). The conclusion in this section is qualitatively consistent with the work by Lipari who claims that sensitivity to CP violation decreases as E_μ becomes large. However it may not be quantitatively consistent with in which it was suggests that sensitivity starts getting lost for $E_\nu \gtrsim$ a few GeV. In our discussion here it was necessary to have $|\Delta E_{31}L| \ll 1$ which may not be attained for $L \sim 3000$ km and $E_\mu \lesssim 50$ GeV. Our numerical calculations in the previous section indicate that the sensitivity is optimized for 20 GeV $\lesssim E_\mu \lesssim 50$ GeV which is quantitatively consistent with the results in [5, 7, 47, 48, 49, 50, 51, 52, 53, 54, 56, 57]. This interval for E_μ is the intermediate energy region which cannot be treated analytically using our arguments in this section. In fact it seems difficult to explain analytically the strong correlation of $(\bar{\delta}, \bar{C})$ for $E_\mu \simeq 50$ GeV and $L \simeq 3000$ km. (cf. Fig.C.1)

C.5   The JHF-NU superbeam experiment

The JHF project [71] has been proposed to perform precise measurements of the oscillation parameters. The possible extension of this project includes the upgrade of the power to 4MW and the construction of a mega–ton detector [67]. The possibility to measure CP violation at the JHF project has been discussed by [72, 70, 73]. Here we briefly discuss the possibility of measurements of CP violation at the JHF experiment with power 4MW and a 1 Mton detector as a comparison with neutrino factories. As in previous sections, we will take into consideration the correlations of all the oscillation parameters. In the case of the JHF experiment, which has the baseline $L \simeq 300$ km, the matter effect is almost negligible and it is possible to compare the numbers of events for $\nu_\mu \to \nu_e$ and $\bar{\nu}_\mu \to \bar{\nu}_e$ directly by taking into account the difference of the cross sections between $\sigma_{\nu N}$ and $\sigma_{\bar{\nu} N}$. However, we use the same $\Delta\chi^2$, as discussions with the same criterion gives more transparent comparisons between neutrino factories and the superbeam at JHF.

The correlations of two variables (δ, X), where X is $\theta_{k\ell}$, $\Delta m^2_{k\ell}$ or C, are shown in Fig.C.11, where the central values for these parameters are those of the best fit point, i.e., $\sin^2 2\theta_{12} = 0.75$, $\Delta m^2_{21} = 3.2 \times 10^{-5} \text{eV}^2$; $\sin^2 2\theta_{23} = 1.0$, $\Delta m^2_{32} = 3.2 \times 10^{-3} \text{eV}^2$, C=1.0 and we have used a reference value $\theta_{13} = 8°$. In this calculation the narrow band beam (NBB) (the flux referred to as LE2π in [71]) is used, and it is assumed for simplicity that there are no backgrounds and the detection efficiency is 70% in Fig.C.11. Note that for the purpose of measurements of CP violation NBB is more advantageous than the wide band beam, as the former has better energy resolution.

As in the previous sections, we have evaluated numerically the data size required to reject a hypothesis with $\bar{\delta} = 0$. Of course the data size depends on the true value δ and the results obtained by varying the six variables $(\theta_{k\ell}, \Delta m^2_{k\ell}, C)$ are plotted in Fig.C.12, where we have taken the best fit values for $(\theta_{12}, \Delta m^2_{21})$, $(\theta_{23}, \Delta m^2_{32})$, $\theta_{13} = 8°, 5°, 1°(2°)$, and the NBB is used. The vertical axis of Fig.C.12 stands for the data size required per kt$\times(\nu_\mu$ 1 year $+ \bar{\nu}_\mu$ 2 years). We have used two ways of ν_e selections, one is 1-ring e-like selection which has the background fraction $f_B = 1.8 \times 10^{-2}$, the detection efficiency 70.4%, and the other one is π^0 cut selection which has the background fraction $f_B = 2 \times 10^{-3}$, the detection efficiency 50.4% [72]. In the case of the 1-ring e-like selection, for $\theta_{13} = 1°$ the systematic error becomes so large that the data size required to reject $\bar{\delta} = 0$ becomes infinite. Also in this case the number of events for $\delta = \pi$ becomes almost the same as that for $\delta = 0$ up to the systematic errors and there is no way to distinguish the case of $\delta = \pi$ and that of $\delta = 0$. However, as long as the value of δ is not close to 0 or π and $\theta_{13} \gtrsim 3°$, the JHF with 4MW power and a 1 mega ton detector will be able to demonstrate $\bar{\delta} \neq 0$ at 3σCL.

C.6 Discussions

The bottom line of the present section is that either the high ($E_\mu \sim$ 50 GeV) or medium ($E_\mu \sim$ 20 GeV) energy option is certainly better than the low energy ($E_\nu \ll 10$ GeV) option which has been advocated by some people [56, 62, 63]. We have arrived at this conclusion on the assumption that the energy threshold is as low as 0.1 GeV, and the detection efficiency is independent of the neutrino energy. In practice, it may be very difficult to have such a low threshold and to keep such a good detection efficiency down to 0.1 GeV, so it is expected that the low energy option becomes less and less advantageous.

If $\theta_{13} \gtrsim 3°$ and if the value of δ is not close to 0 or π, then the JHF experiment with 4MW power and a 1 mega ton detector will be able to demonstrate $\bar{\delta} \neq 0$ at 3σCL. On the other hand, if $\theta_{13} \lesssim 3°$, then neutrino factories seem to be the only experiment which can demonstrate $\bar{\delta} \neq 0$. In that case, depending on the situation such as the fraction of backgrounds, the uncertainty of the matter effect and the magnitude of θ_{13}, the option with ($E_\mu \simeq$50 GeV, $L \simeq$3000 km) may be advantageous (or disadvantageous) over ($E_\mu \simeq$20 GeV, $L \simeq$1000 km). In both a neutrino factory with (20 GeV $\lesssim E_\mu \lesssim$ 50 GeV, 1000 km $\lesssim L \lesssim$ 3000 km) and the JHF experiment, our $\Delta\chi^2$(CPV) depends not only on $\sin\delta$ but also $\cos\delta$, [3] so that we can in principle distinguish $\delta = \pi$ from $\delta = 0$ as long as the statistical significance overcomes the systematic errors. This is not the case for a neutrino factory with large systematic errors for small θ_{13}, i.e., for E_μ=50 GeV and $\theta_{13} = 1°$ (cf. Fig.C.10), and for the JHF experiment with less S/N ratio i.e., when the 1-ring e-like selection is adopted, or when $\theta_{13} = 8°$ and the π^0 cut selection is adopted (cf. Fig.C.12). From Fig.C.10 we find that the high energy option $E_\mu \sim 50$ GeV, which has been advocated as the best choice, is not always the best, when the background effect is taken into account. In fact, if UNO type detectors with the detector mass ~ 1 mega ton and the background fraction $f_B \sim 10^{-3}$ can be built, then $E_\mu \sim 20$ GeV, $L \sim 1000$ km is probably the best parameter set for measurements of CP violation for generic values of θ_{13} and ΔC.

In order to be more concrete, we need the knowledge on the uncertainty of the matter effect A. The error of $A = \sqrt{2}G_F Y_e \rho$ comes from those of Y_e and ρ. The error of Y_e has been discussed by [74] and it is about 2% and geophysicists [75, 76] agree with it. Without any uncertainty of the matter effect, it has been claimed that a medium baseline experiment ($L \sim$ 3000km, $E_\mu \sim 50$ GeV) is best for measurements of CP violation. In that case the depth of the neutrino path is at most 200 km and most of the neutrino path is in the upper mantle. It is known in geophysics [77] that the crust has relatively large latitude-longitude dependent fluctuations around constant density. On the other hand, in the case of the upper mantle, some geophysicists claim that fluctuations around constant density are a few %

---

[3]If we evaluate $\Delta\chi^2$(CPV; (δ,θ_{13})) in (C.15) to the next leading order in $\Delta m^2_{31} L/E_\mu$ then $\tilde{J}^2 \sin^2\delta$ in (C.15) is replaced by $\tilde{J}^2(\sin\delta+\text{const.}(\Delta m^2_{31}L/E_\mu)\cos\delta)^2$, and $\Delta m^2_{31}L/E_\mu$ is not necessarily negligible in either case.

[78, 75, 76] while another [79] says that they may be as large as 5 %. However, such discussions are based on normal mode studies in seismology which are confined to long wavelength features, and it was pointed out [76, 79] that the fluctuations in the density in the analysis of neutrino factories may be larger than 5 %, since the width of the neutrino beam is much smaller than typical wavelengths in seismological studies. If that is the case, then it follows from Fig. C.9 that the case $L \simeq 1000$ km is better than the case $L \simeq 3000$ km, since the former is insensitive to the uncertainty of the matter effect. In this section we adopted simplified assumptions such as that the detection efficiency is independent of the neutrino energy, that the threshold energy can be taken as low as 0.1GeV, and that the uncertainty of the matter effect is at most 5 %. We need much more detailed experimental information as well as seismological discussions to obtain the optimal baseline and the muon energy in neutrino factories.
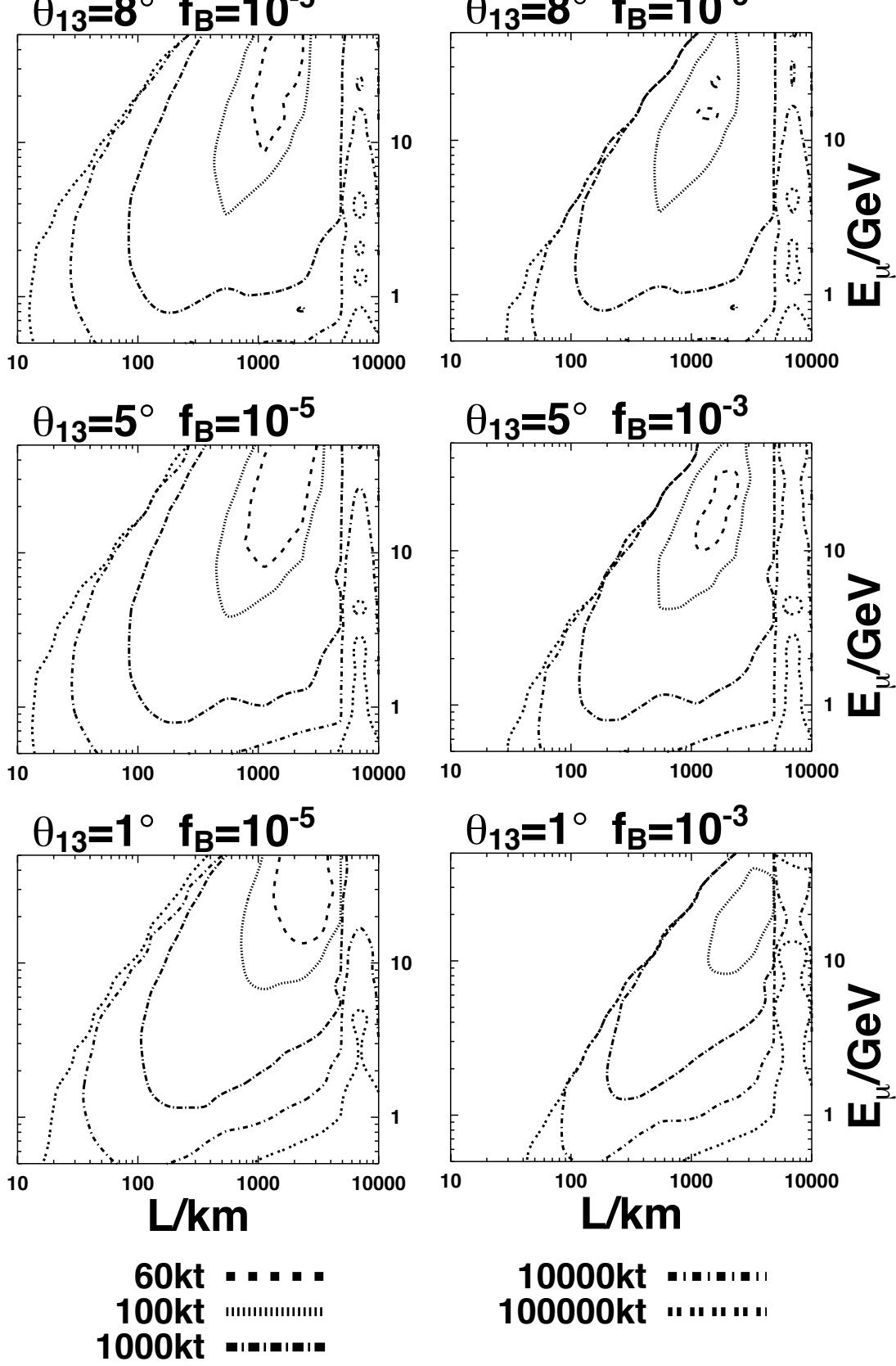
Figure C.8: The contour plot of equi-number of data size required (in the unit of kt) to reject a hypothesis $\bar{\delta} = 0$ at 3σ using $\Delta\chi^2(\text{CPV})$ (C.3) in the case of a neutrino factory with 10^{21} useful muon decays, the background fraction $f_B = 10^{-5}$ or 10^{-3}, $\theta_{13} = 8°$, $5°$, $1°$. The other oscillation parameters are the same as in Fig.C.1.
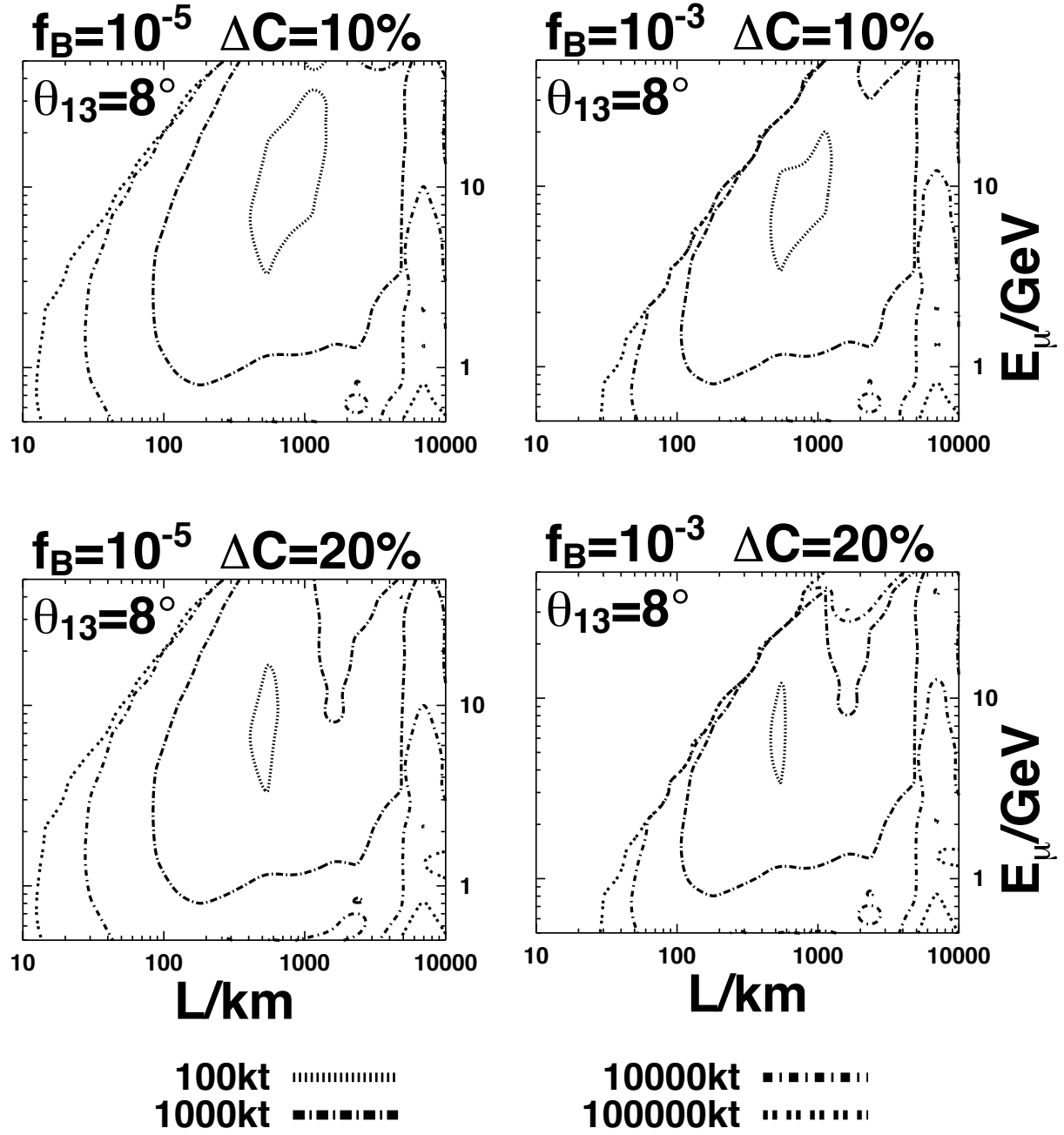
91

Figure C.9: The same as Fig.C.8 with $\theta_{13} = 8°$, except that the uncertainty of the matter effect is assumed to be larger $|\Delta C| \leq 0.1$ or $|\Delta C| \leq 0.2$.
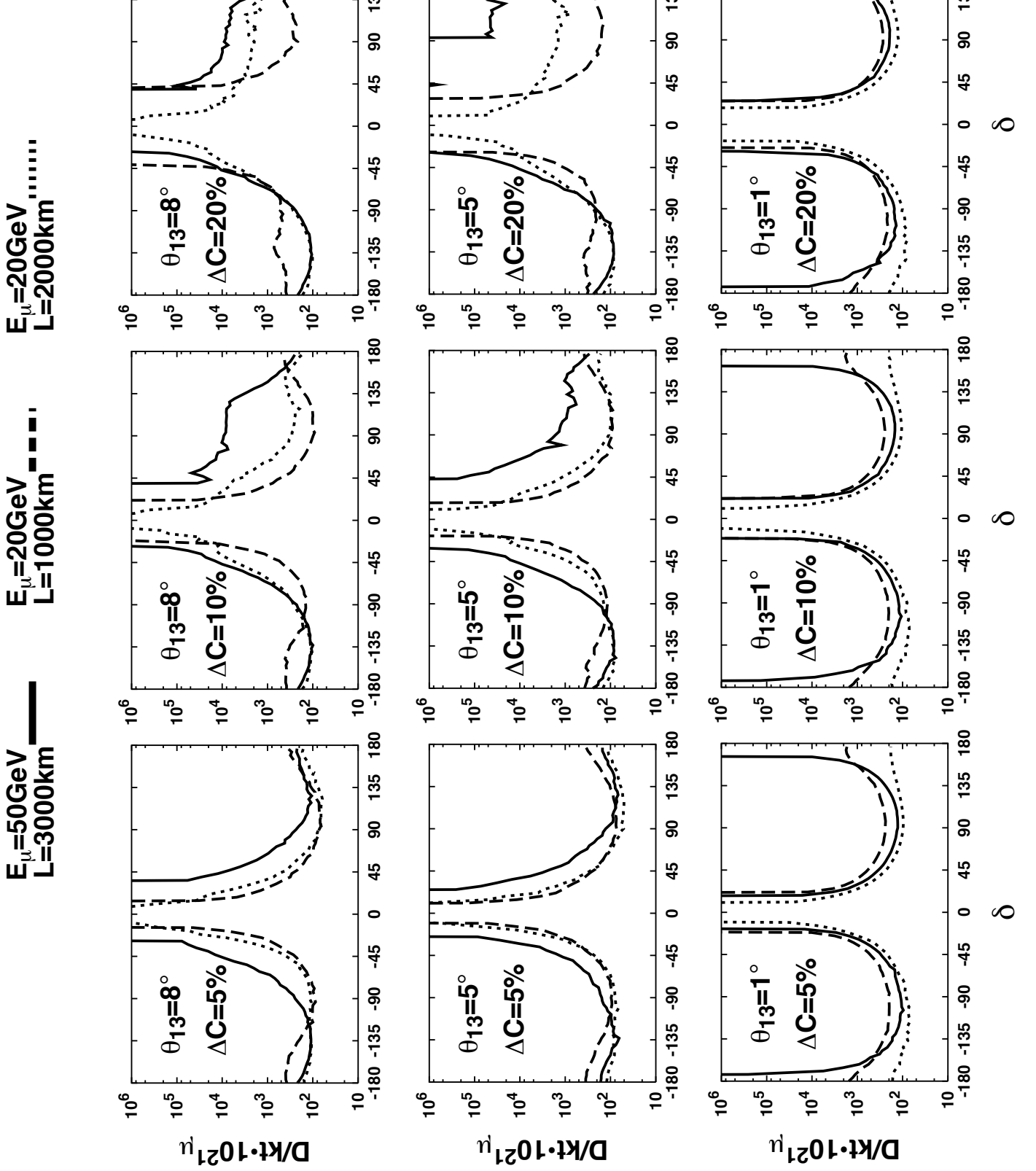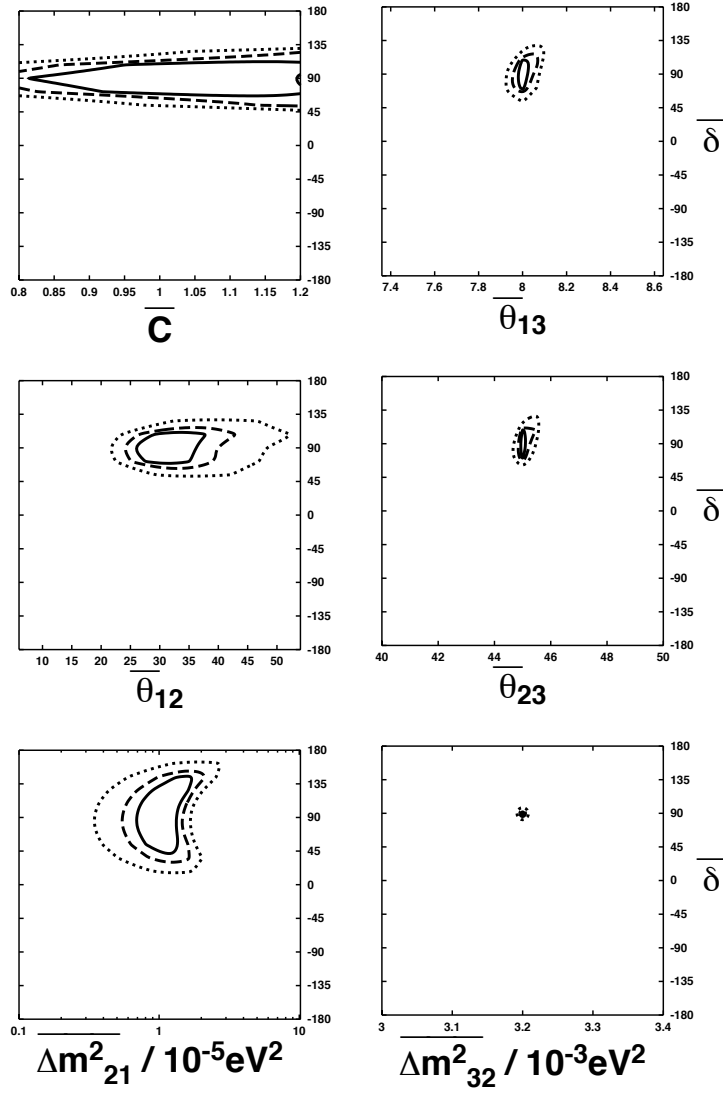
Figure C.10: The number of data size required to reject a hypothesis $\bar{\delta} = 0$ at 3σ for a neutrino factory using $\Delta\chi^2(\text{CPV})$ (C.3) as a function of the true value of δ for $f_B = 10^{-3}$. All the assumptions except for δ are the same as in Fig.C.8. The situation is improved for smaller θ_{13}.

Figure C.11: The correlations of errors of $(\bar{\delta}, \bar{C})$, $(\delta, \bar{\theta}_{13})$, $(\delta, \bar{\theta}_{12})$, $(\delta, \bar{\theta}_{23})$, $(\delta, \overline{\Delta m^2_{21}})$, $(\delta, \overline{\Delta m^2_{32}})$ in the case of the JHF experiment with 4MW power, a 1 mega ton detector and NBB. No backgrounds are taken into consideration in these figures. The oscillation parameters used are the same as in Fig.C.1.
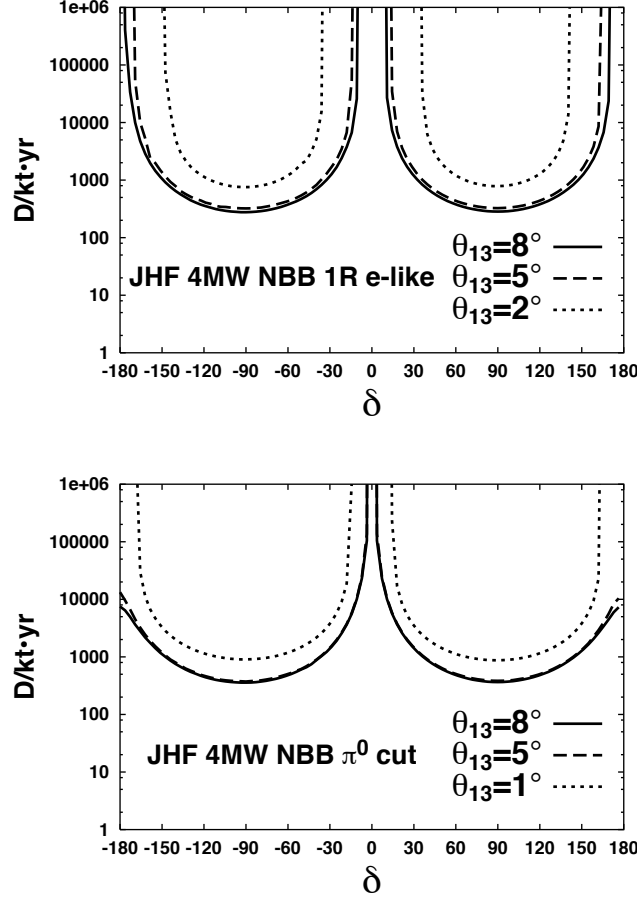
Figure C.12: The number of data size required (in the unit of kt) to reject a hypothesis $\bar{\delta} = 0$ at 3σ for the JHF experiment with 4MW power, a 1 mega ton detector and NBB using $\Delta\chi^2(\text{CPV})$ (C.3) as a function of the true value of δ. Unlike in the case of Fig.C.11, the effects of backgrounds are taken into account in this figure. The oscillation parameters used are the same as in Fig.C.1, and two ways of cuts (1-ring e-like and π^0 cut) [72] are used. In the case of the 1-ring e-like selection, $\theta_{13} = 1°$ does not have a solution because the systematic errors become so large.

Appendix D

Statistical Evaluation on Sensitivities

In the following, a different approach of statistics needed is shown.[1]

D.1 Determination of U_{e3}

In this section, it is estimated how large data sample is needed to see that $\sin\theta_{13} \neq 0$. Since the solar neutrino mixing is attributed to the LMA solution, then even if $\sin\theta_{13} = 0$, we can observe the appearance event. Indeed at the high energy region the oscillation effect due to the solar mixing mimics that due to $\sin\theta_{13}$. Therefore we estimate the data size in the LMA case since we can expect that there is a difficulty to see that $\sin\theta_{13} \neq 0$.

Now the following test statistics is employed:

$$
T_{13}^2 = \sum_i^n \frac{[\bar{N}_i^{\text{th}}(0;\tilde{x}_j)N_i^{\text{ex}} + N_i^{\text{th}}(0;\tilde{x}_j)\bar{N}_i^{\text{ex}} - 2N_i^{\text{th}}(0;\tilde{x}_j)\bar{N}_i^{\text{th}}(0;\tilde{x}_j)]^2}{\{\bar{N}_i^{\text{th}}(0;\tilde{x}_j)\}^2 N_i^{\text{ex}} + \{N_i^{\text{th}}(0;\tilde{x}_j)\}^2 \bar{N}_i^{\text{ex}}} \tag{D.1}
$$

where $N_i^{\text{ex}}(\bar{N}_i^{\text{ex}})$ denotes the appearance event rate for $\nu_e \to \nu_\mu$ ($\bar{\nu}_e \to \bar{\nu}_\mu$) at the energy bin i. Here, we use the theoretically-calculated event rate $N_i^{\text{th}}(\theta_{13}; x_j)$ for the mixing parameters $\{x_i\} \equiv \{\theta_{12}, \theta_{23}, \delta m_{ij}^2, \delta, a\}$. By varying $\tilde{x}_j$'s with $\theta_{13} = 0$ we search for the minimum of T_{13}^2,

$$
\chi_{13}^2 \equiv \min_{\tilde{x}_j, n} T_{13}^2 \tag{D.2}
$$

and from χ_{13}^2 we estimate the necessary data size. See ref.[82] for details. We plot in Fig.D.1 the required data size in the unit 10^{21} for parent muon number and 100kt for the detector mass. Here $\{\theta_{12}, \theta_{23}, m_{31}^2, m_{21}^2, \delta\} = \{\pi/4, \pi/4, 3 \times 10^{-3}\text{eV}^2, 10^{-4}\text{eV}^2, 0\}$. As we expected, while for small $\sin\theta_{13}$ the sensitivity depends on $\sin\theta_{13}^2 E_\mu$, the sensitivity is drastically worse for small $\sin\theta_{13}$.

In conclusion we can observe the effect by $\sin\theta_{13}$ very precisely if it is larger than 0.03. If it is smaller than 0.03, we need a very precise information

---

[1]This study has been done by J. Sato et al.

about the mixing angle and the mass square difference for the solar neutrino mixing.

D.2 Determinetion of the Sign of Δm^2

It is estimated how large data sample is needed to see the sign of Δm_{31}^2. Since to determine the sign of Δm_{31}^2 is essentially the same as to see the fake CP asymmetry due to the matter effect, we employ the following test statistics.

$$T_m^2 = \sum_i^n \frac{[\bar{N}_i^{\text{th}}(-\Delta m_{31}^2; \tilde{x}_j) \times N_i^{\text{ex}} - N_i^{\text{th}}(-\Delta m_{31}^2; \tilde{x}_j) \times \bar{N}_i^{\text{ex}}]^2}{\{\bar{N}_i^{\text{th}}(-\Delta m_{31}^2; \tilde{x}_j)\}^2 N_i^{\text{ex}} + \{N_i^{\text{th}}(-\Delta m_{31}^2; \tilde{x}_j)\}^2 \bar{N}_i^{\text{ex}}}, \quad \text{(D.3)}$$

where $N_i^{\text{ex}}(\bar{N}_i^{\text{ex}})$ denotes the appearance event rate for $\nu_e \to \nu_\mu$ ($\bar{\nu}_e \to \bar{\nu}_\mu$) at the energy bin i. Here, we use the theoretically-calculated event rate $N_i^{\text{th}}(\Delta m_{31}^2; x_j)$ for the parameters $\{x_i\} \equiv \{\theta_{ij}, \delta, \Delta m_{21}^2, a\}$. By varying the bin number n and $\tilde{x}_j$'s with $-\Delta m_{31}^2$ search the minimum of T_m^2,

$$\chi_m^2 \equiv \min_{n, \tilde{x}_j, -\Delta m_{31}^2} \frac{T^2}{\chi_\alpha^2(n)} \quad \text{(D.4)}$$

and from χ_m^2 we estimate the necessary data size to the sign of Δm_{31}^2 at the level of significance of α. See ref.[82] for details. Hereafter we set $\alpha = 0.01$ which naively corresponds to 99% confidence level.

In Fig.D.2, we show the required data size to see the sign in the unit 10^{21} for parent muon number and 100kt for the detector mass. There we plot it for various $\sin\theta_{13}$ and $\{\sin\theta_{12}, \sin\theta_{23}, \Delta m_{31}^2, \Delta m_{21}^2\} = \{\pi/4, \pi/4, 3 \times 10^{-3}\text{eV}^2, 10^{-4}\text{eV}^2\}$.[2] From these graphs we find that it is difficult to observe the sign at a shorter baseline. Indeed the asymmetry due to the matter effect takes the form

$$\frac{2}{3} \sin^2\theta_{23} \sin^2 2\theta_{13} \cos 2\theta_{13} \frac{a(L)L}{4E_\nu} \left(\frac{\Delta m_{31}^2 L}{4E_\nu}\right)^3. \quad \text{(D.5)}$$

As a event rate it increased with L^2 and hence the sensitivity to the sign increases with L^4. Thus a longer baseline is much more suitable for the observation of the sign of Δm_{31}^2.

In Fig.D.3, it is shown how large data size is required to see the sign of Δm_{31}^2 for various values of $\sin\theta_{13}$ at $L = 2000$ km with $E_\mu = 20\text{GeV}$. The required data size depends on $\sin^2\theta_{13}$ in the case of rather large values of $\sin\theta_{13}$. It is easily understood; From Eq.D.5 the numerator of Eq.D.3 depends on $\sin^4\theta_{13}$ while the denominator depends on $\sin\theta_{13}$. On the other hand, in the case of smaller $\sin\theta_{13}$, the dependence is rather complicated. In the numerator of Eq.D.3 there is also a contribution from the true CP-violation effect and its ambiguity can mimic the fake asymmetry due to the

---

[2] Matter density is approximated to be constant and calculated by PREM. Thus the matter effect has a dependence on the baseline length, $a(L)$.
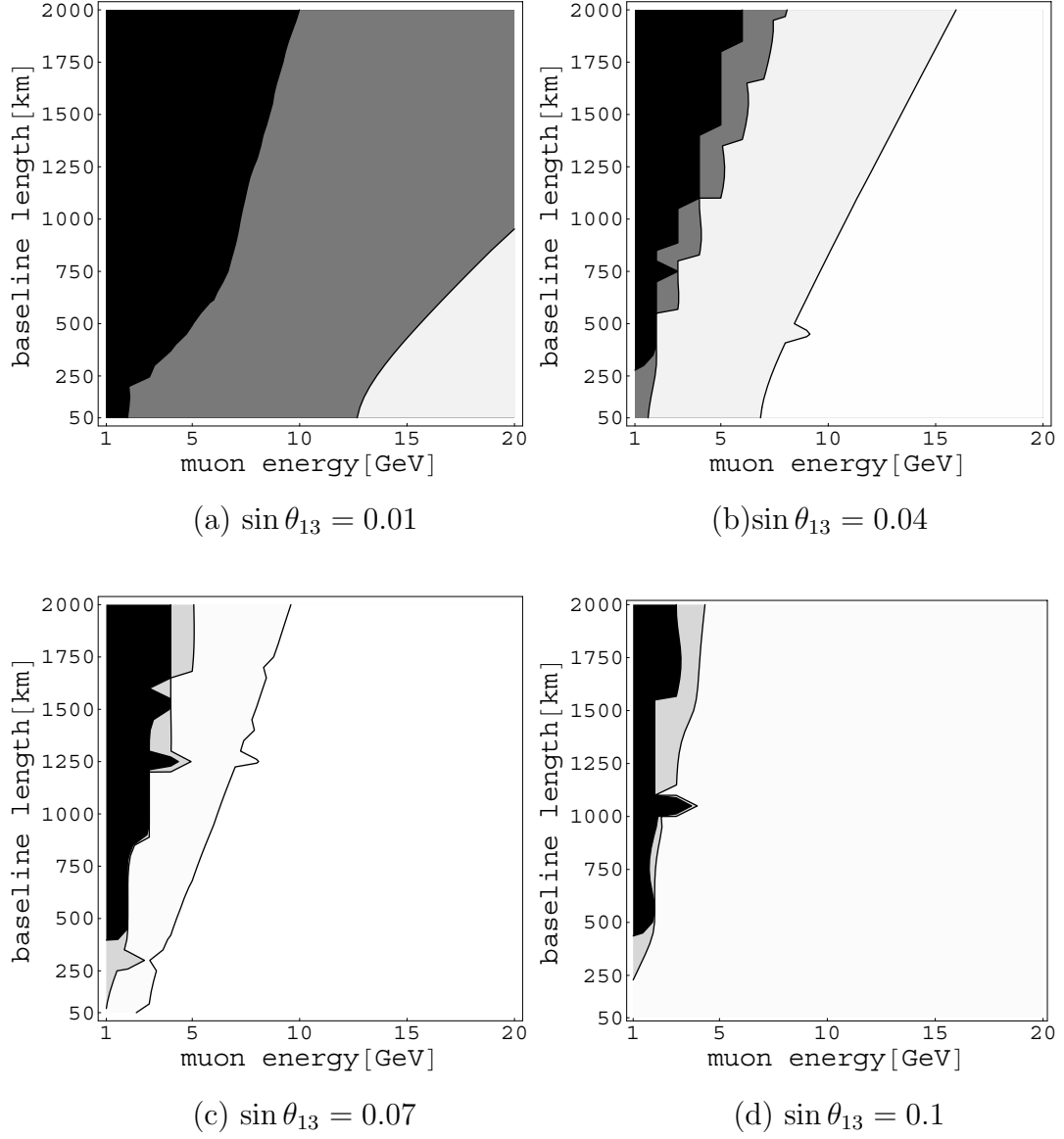
Figure D.1: Required data size in the unit $[10^{21} 100\text{kt}]$ to observe that $\sin\theta_{13} \neq 0$ as a function of muon energy E_μ and baseline length L. $\sin\theta_{13} =$(a) 0.01, (b) 0.04, (c) 0.07, (d) 0.1 .
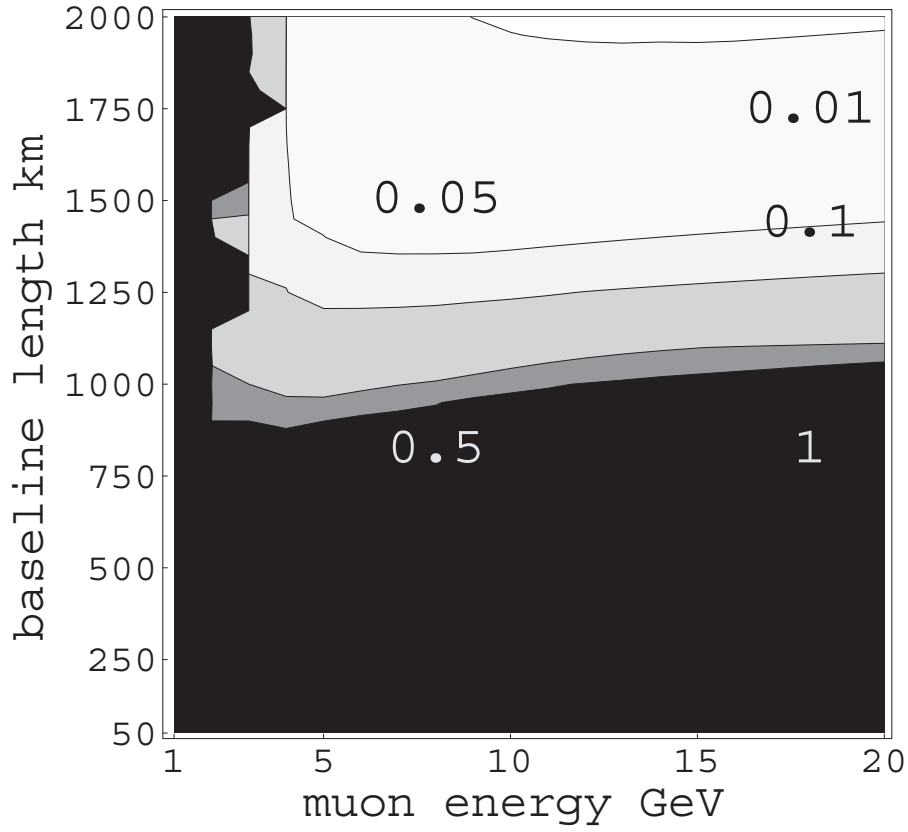
98

Figure D.2: Required data size to observe the sign of Δm^2_{31} as function of muon energy E_μ and baseline length L.

matter effect. Therefore the sensitivity to the sign becomes drastically worse. In the reference value of the theoretical parameters considered here, we find in Fig.D.3 that for $\sin\theta_{13} < 0.03$ the matter effect can hidden and hence the sensitivity becomes worse.

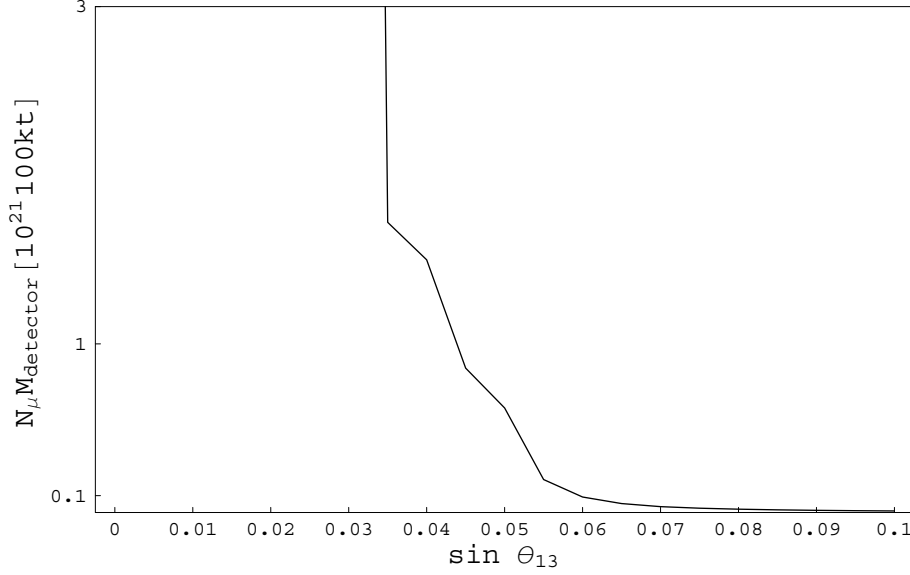To raise the sensitivity to the sign we should make an experiment with longer baseline.

Figure D.3: Required data size to observe the sign of Δm^2_{31} as a function of $\sin\theta_{13}$ at $L = 2000$km and $E_\mu = 20$ GeV.

D.3 Measurement of CP asymmetry

Here we estimate how large data size we need to see the CP-violation effect as the asymmetry between neutrinos and anti-neutrinos. We employ the following test statistics.

$$T^2 = \cdot \sum_i^n \frac{[\bar{N}_i^{\text{th}}(\delta_0; \tilde{x}_j) \times N_i^{\text{ex}} - N_i^{\text{th}}(\delta_0; \tilde{x}_j) \times \bar{N}_i^{\text{ex}}]^2}{\{\bar{N}_i^{\text{th}}(\delta_0; \tilde{x}_j)\}^2 N_i^{\text{ex}} + \{N_i^{\text{th}}(\delta_0; \tilde{x}_j)\}^2 \bar{N}_i^{\text{ex}}}. \tag{D.6}$$

Here $N_i^{\text{ex}}(\bar{N}_i^{\text{ex}})$ denotes the appearance event rate for $\nu_e \to \nu_\mu$ ($\bar{\nu}_e \to \bar{\nu}_\mu$) at energy bin i. Here, since we do not have any real data, we replace them with theoretically calculated event rate $N_i^{\text{th}}(\delta; x_j)$ using the theoretical parameters $\{x_i\} \equiv \{\theta_{ij}, \Delta m^2_{ij}, a\}$. By varying the bin number n and $\tilde{x}_j$'s with $\{\delta_0\} = \{0, \pi\}$ we search the minimum of T^2,

$$\chi^2 \equiv \min_{n, \tilde{x}_j, \delta_0} \frac{T^2}{\chi^2_\alpha(n)} \tag{D.7}$$

and from χ^2 we estimate the necessary data size to see the CP-violation effect at α level of significance. See the appendix of ref.[82] for details. Hereafter we set $\alpha = 0.01$ which naively corresponds to 99% confidence level.

In Fig.D.4 We show the required data size to see the CP-violation effect in the unit 10^{21} for parent muon number and 100kt for the detector mass. There we plot it for various δ and Δm^2_{21} and $\{\sin\theta_{13}, \sin\theta_{12}, \sin\theta_{23}, \Delta m^2_{31}\} =$

$\{0.1, \pi/4, \pi/4, 3 \times 10^{-3}\text{eV}^2\}$.[3] From these graphs we find that it is difficult to observe the CP asymmetry with longer baseline. Since the neutrino propagates in the earth, there is not only the pure asymmetry due to the CP-violation effect but also that due to the matter effect. We have to distinguish them. The CP asymmetry is almost proportional to

$$J_{/\delta} \equiv \frac{\Delta m_{21}^2}{\Delta m_{31}^2} \sin 2\theta_{12} \sin 2\theta_{23} \sin 2\theta_{13} \cos \theta_{13} \sin \delta \qquad (D.8)$$

and the matter asymmetry is proportional to

$$\frac{2}{3} \sin^2 \theta_{23} \sin^2 2\theta_{13} \cos 2\theta_{13} \frac{a(L)L}{4E_\nu}. \qquad (D.9)$$

From these Eqs.D.8 and D.9 we find that at a longer length it become difficult to see the CP-violation effect as the asymmetry. Moreover it is easy to understand for smaller Δm_{21}^2 and $\sin \delta$ the shorter baseline becomes better.

Next we study the sensitivity to the asymmetry at $L = 1000km$. In FigD.5 we plot the required data size for various $\sin \theta_{13}$ with (a) E_μ. From these graphs we find that the sensitivity depends very weakly on $\sin \theta_{13}$. It is easily understood from Eq.D.8. Since the asymmetry is proportional to $\sin \theta_{13}$, in the test statistics Eq.D.1 the dependence on $\sin \theta_{13}$ almost cancels. It is also easy to understand that the sensitivity is slightly worse in the larger $\sin \theta_{13}$ region. Since for larger $\sin \theta_{13}$ the matter effect is stronger as seen in Eq.D.9, the sensitivity is slightly worse.

In conclusion, if we want to see the CP-violation effect as the difference between neutrino and anti-neutrino we have to make an experiment at shorter distance as long as the theoretical parameters have ambiguities.

---

[3]Matter density is approximated to be constant and calculated by PREM. Thus the matter effect has a dependence on the baseline length, $a(L)$).
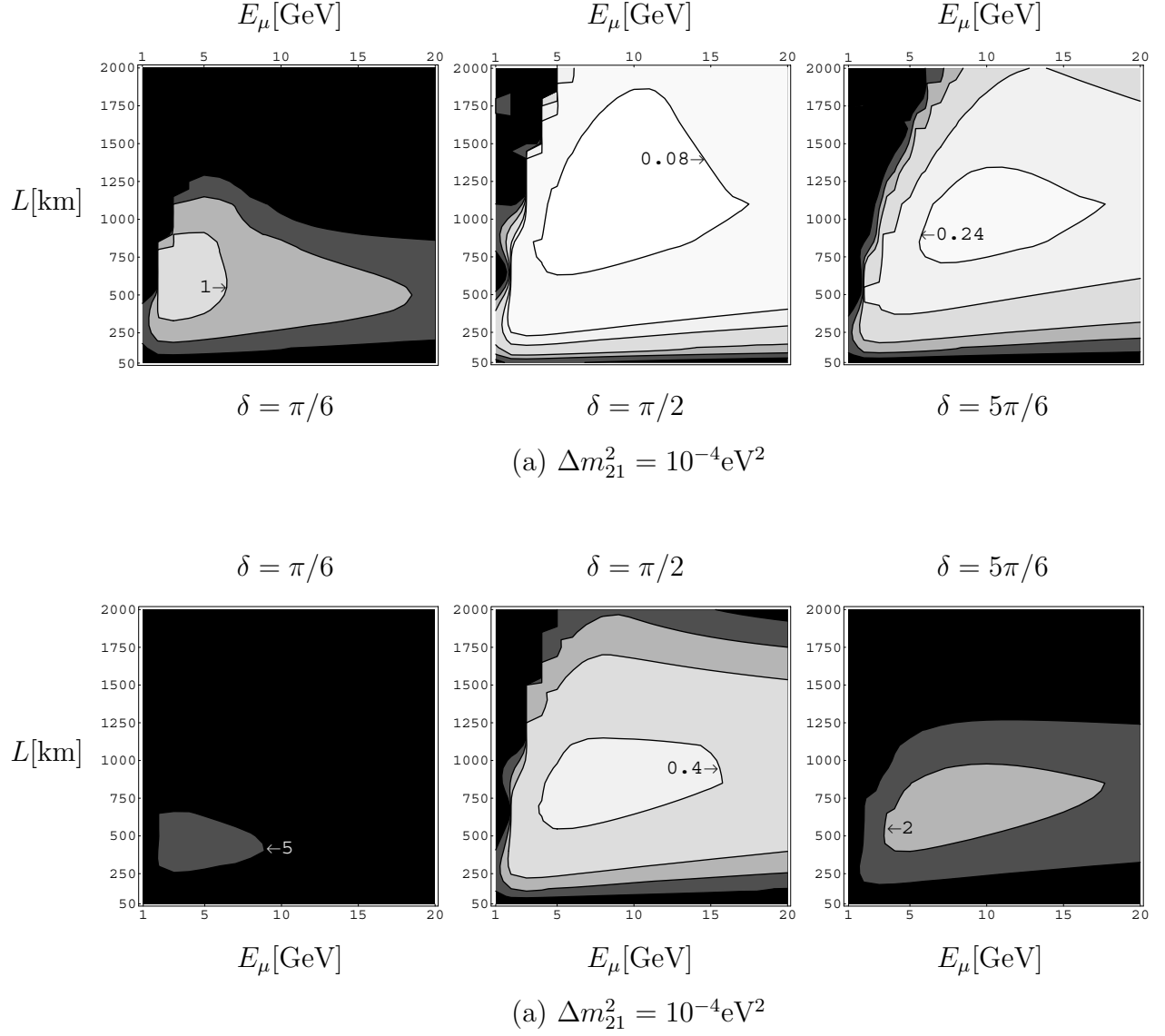
Figure D.4: Required data size in the unit $[10^{21}100\text{kt}]$ to observe the CP-violation effect as a function of muon energy E_μ and baseline length L for various δ and Δm_{21}^2. (a) $\Delta m_{21}^2 = 10^{-4}$ eV^2. (b) $\delta m_{21}^2 = 5 \times 10^{-5}$ eV^2.
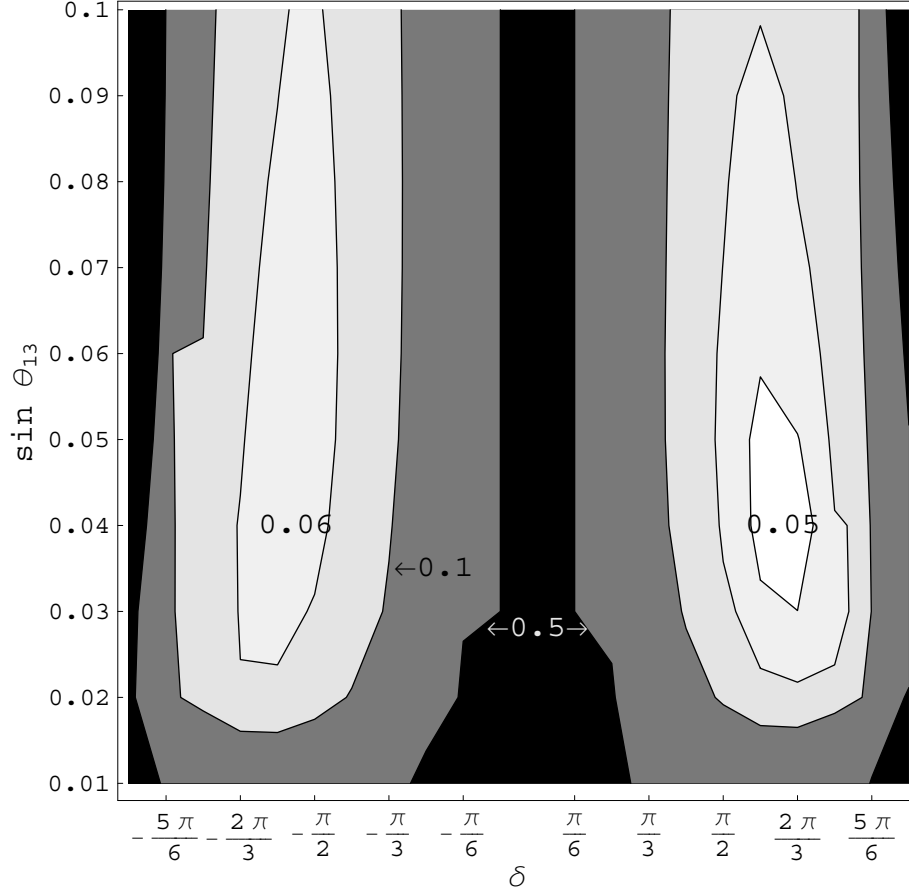
Figure D.5: Required data size at $L = 1000$km and $E_\mu = 10$ GeV in the unit $[10^{21}100\text{kt}]$ for various $\sin\theta_{13}$.